

UC Davis

UC Davis Electronic Theses and Dissertations

Title

Leveraging metabolomics for pathobiology: Advancements and applications of mass spectrometry-based approaches for chemical biology.

Permalink

<https://escholarship.org/uc/item/5qm5315h>

Author

Rabow, Zachary

Publication Date

2022

Peer reviewed|Thesis/dissertation

Leveraging metabolomics for pathobiology: Advancements and applications of mass spectrometry-based approaches for chemical biology.

By

ZACHARY T RABOW
DISSERTATION

Submitted in partial satisfaction of the requirements for the degree of

DOCTOR OF PHILOSOPHY

in

Integrative Pathobiology

in the

OFFICE OF GRADUATE STUDIES

of the

UNIVERSITY OF CALIFORNIA

DAVIS

Approved:

Oliver Fiehn, Chair

Denise Imai

Kevin Woolard

Committee in Charge

2022

Acknowledgements

I would like to extend my gratitude to the members of my dissertation committee, Prof. Denise Imai-Leonard and Prof. Kevin Woolard for their valuable feedback and guidance during my training, qualifying exam and dissertation.

I am thankful for the mentorship and guidance from Dr.'s Mirna Lechpammer, Megan Showalter, Tong Shen, Arpana Vaniya, and Uri Keshet. Each played an invaluable role in my training. I want to pay a special thanks to Kelly Paglia, Greg Byram, Luis Valdiviez, and Iris Beussen for their help and support during my tenure at the Fiehn Lab.

I would not have been able to successfully complete my PhD without the infinite support, advice, and encouragement from my friends. I am particularly grateful to Dr.'s Alex McInturf and Evan Batzer, to Alessandra Zuniga, Dr. Kyra Laubach, Jenn Cossaboon, and a wonderful collection of humans that make up my chosen family. Each of you have supported me and helped me tremendously- thank you. Graduate school during a pandemic brought special challenges, and you all helped me stay the course and thrive.

I want to thank my mother, Karen Rabow, for her endless care and love in supporting me and my goals. I cannot express the amount of gratitude, love, and respect I have for her.

Finally, completion of this dissertation would not be possible without the support of my PhD advisor and committee chair, Prof. Oliver Fiehn. Prof. Fiehn's love of science and extensive knowledge has been inspiring and has shaped my scientific outlook, I am forever grateful for his leadership and mentorship.

Abstract

Metabolism occurs in a spatial-temporal fashion and represent the product of cellular functions. Mass spectrometry-based metabolomics enables the analysis of hundreds to thousands of analytes that can be used to study biological processes in the context of disease. Here, we leverage novel mass spectrometry approaches- both high-resolution mass spectrometry coupled to liquid chromatography, as well as matrix assisted laser desorption ionization mass spectrometry imaging- to exam neurometabolic related questions.

Chapter one characterizes the biochemical, behavioral, and cytological in the brain in long-evans rats following neonatal, postnatal day six (P6), exposure to DMSO, the widely used vehicle (VEH) solvent. First, neurometabolic changes were profiled 24 hours after exposure in four distinct brain regions- the cortex, hippocampus, basal ganglia, and cerebellum- using hydrophilic interaction liquid chromatography. Second, behavioral tests were performed between P21-40 to investigate the chronic alterations to behavior following short term, early exposure. Lastly, immunofluorescence and immunohistochemistry were used to assess cytological changes in microglia, astrocytes, and neurons at P40. These findings show that short term exposure of DMSO, regardless of dose, at neonatal stages alters key regulatory metabolites and alters neurochemistry, results in chronic hypoactive behavior and decreased social habits, and in dose dependent increase in microglia and astrocytes.

Chapter two investigates the role of p73 α 1, a p73 C-terminal isoform, in regulating lipid metabolism. Characterization of this novel protein isoform was described by Dr. Kyra Laubach, and cell lines were generated using CRIPSR to remove *E12 in cancer cell lines*.






A multi-omic approach was integrated with molecular biology techniques to identify lipid classes and lipid metabolism-associated genes that were altered by the expression of p73 α 1. Furthermore, the tumor suppressive function of p73 α 1 was found to be mediated in part through lipid metabolism-associated genes. Through these findings, a previously unidentified p73 target was established, in addition to determining a role for p73 α 1 in lipid metabolism.

Chapter three provides a framework and application for spatial metabolomics using matrix assisted laser desorption ionization- mass spectrometry imaging (MALDI-MSI). I demonstrate that spatial metabolomics enables data driven segmentation that provides unique clusters that resemble and map to anatomical structures. Next, I show that lipids in the brain are highly organized, and these lipids can be identified in tissue through MS/MS experiments. Additionally, I perform manual segmentation to extract ion intensities for regions of interest and show that MSI enables histopathological analysis of small molecules. Finally, I apply this workflow to a case study of litter-matched matched rats, one that expresses transgenes that induce an Alzheimer-like pathology, and its wild-type, healthy control litter-mate. I show that several phosphatidylcholine (PC) lipids are altered in the entire brain and specific regions of interest. Other PC lipids are changed only in clear ROIs when comparing WT and AD brains but are not changed in the whole brain. This workflow is a critical step necessary to enable histopathological analysis using metabolomics.

Table of Contents

Acknowledgements	ii
Abstract	iii-iv
Table of Contents	v
Chapter 1: Exposure to DMSO during infancy alters neurochemistry, social interactions, and brain morphology in long-evans rats	1-18
Chapter 2: p73 α 1, an isoform of the p73 tumor suppressor, modulates lipid metabolism and cancer cell growth via Stearoyl-CoA Desaturase-1	19-43
Chapter 3: Application of MALDI Mass Spectrometry Imaging for Spatially Resolved Metabolomics	44-59
Appendix: Other projects	60-62

Exposure to DMSO during infancy alters neurochemistry, social interactions, and brain morphology in long-evans rats

Zachary Rabow^{1,2}  | Taryn Morningstar¹ | Megan Showalter²  | Hailey Heil² |
 Krista Thongphanh¹ | Sili Fan² | Joanne Chan¹ | Verónica Martínez-Cerdeño^{1,3,4}  |
 Robert Berman^{3,5} | David Zagzag⁶ | Evgeny Nudler^{7,8} | Oliver Fiehn²  |
 Mirna Lechpammer^{1,3,8,9} 

¹Department of Pathology and Laboratory Medicine, School of Medicine, University of California Davis, Sacramento, CA, USA

²NIH West Coast Metabolomics Center, University of California Davis, Davis, CA, USA

³MIND Institute, University of California Davis, Sacramento, CA, USA

⁴Institute for Pediatric Regenerative Medicine and Shriners Hospital for Children of Northern California, Sacramento, CA, USA

⁵Department of Neurological Surgery, University of California Davis, Sacramento, CA, USA

⁶Departments of Pathology and Neurosurgery, Division of Neuropathology, NYU Langone Medical Center, New York, NY, USA

⁷Howard Hughes Medical Institute, New York University School of Medicine, New York, NY, USA

⁸Department of Biochemistry & Molecular Pharmacology, New York University School of Medicine, New York, NY, USA

⁹Pathology, Foundation Medicine, Inc., Cambridge, MA, USA

Correspondence

Mirna Lechpammer, Langone Medical Center, New York University, New York, NY, USA.
 Email: mirna.lechpammer@nyulangone.org

Funding information

Rat brain morphology and behavioral studies were supported by research grants awarded to ML and EN by the Zimin Foundation. Metabolomics work was funded by NIH grant (5U19AG023122-12) to OF.

Abstract

Introduction: Dimethyl sulfoxide (DMSO) is a widely used solvent to dissolve hydrophobic substances for clinical uses and experimental in vivo purposes. While usually regarded safe, our prior studies suggest changes to behavior following DMSO exposure. We therefore evaluated the effects of a five-day, short-term exposure to DMSO on postnatal infant rats (P6-10).

Methods: DMSO was intraperitoneally injected for five days at 0.2, 2.0, and 4.0 ml/kg body mass. One cohort of animals was sacrificed 24 hr after DMSO exposure to analyze the neurometabolic changes in four brain regions (cortex, hippocampus, basal ganglia, and cerebellum) by hydrophilic interaction liquid chromatography. A second cohort of animals was used to analyze chronic alterations to behavior and pathological changes to glia and neuronal cells later in life (P21-P40).

Results: 164 metabolites, including key regulatory molecules (retinoic acid, orotic acid, adrenergic acid, and hypotaurine), were found significantly altered by DMSO exposure in at least one of the brain regions at P11 ($p < .05$). Behavioral tests showed significant hypoactive behavior and decreased social habits to the 2.0 and 4.0 ml DMSO/kg groups ($p < .01$). Significant increases in number of microglia and astrocytes at P40 were observed in the 4.0 ml DMSO/kg group (at $p < .015$).

Conclusions: Despite short-term exposure at low, putatively nontoxic concentrations, DMSO led to changes in behavior and social preferences, chronic alterations in glial cells, and changes in essential regulatory brain metabolites. The chronic neurological effects of DMSO exposure reported here raise concerns about its neurotoxicity and consequent safety in human medical applications and clinical trials.

KEYWORDS

glial cells, metabolomics, neurochemistry, neuropharmacology

This is an open access article under the terms of the Creative Commons Attribution License, which permits use, distribution and reproduction in any medium, provided the original work is properly cited.

© 2021 The Authors. *Brain and Behavior* published by Wiley Periodicals LLC

1 | INTRODUCTION

Dimethyl sulfoxide (DMSO) is regarded as a safe solvent, commonly used in *in vivo* experiments. It is also widely available as an over-the-counter, topical pain-relieving agent, and can be purchased in large quantities with no regulation. Additionally, DMSO is a cryopreservative that is re-infused along with stem cells during autologous bone marrow transplantations (Hanslick et al., 2009). DMSO rapidly penetrates the skin and can transport drugs and other molecules that would otherwise not cross the skin. When applied to the skin, DMSO has local anesthetic properties and reduces swelling (Maryland, 1967). Experimentally, DMSO has been used to treat intestinal, renal, and cerebral ischemia, and has been shown to suppress central nervous system (CNS) injury by scavenging inflammation-triggering free radicals (De la Torre et al., 1975; Kedar et al., 1983; Kharasch & Thyagarajan, Little et al., 1983; Ravid et al., 1983). DMSO is fully miscible with other aqueous substances and can form chemical associations with many different molecules and matrices, including metal ions, drugs, and components of tissue, blood, plasma, and spinal fluid (Wong & Reinertson, 1984).

Dimethyl sulfoxide crosses the blood-brain barrier and has been effective in the treatment of traumatic brain edema by reducing the increase in intracranial pressure and by elevating cerebral blood flow without altering blood pressure (Brown et al., 1980; Camp et al., 1981; De la Torre et al., 1975; Ikeda & Long, 1990; Karaca et al., 1991). Dimethyl sulfoxide is metabolized to dimethyl sulfide (DMS) and dimethyl sulfone (DMSO₂). Unmetabolized DMSO is the most abundant form found in the body after exposure. DMSO is found in tissue, blood, feces, and urine regardless of application route (Wong & Reinertson, 1984).

The United States Federal Drug Administration (FDA) approved the use of DMSO for the treatment of interstitial cystitis under the trade name "Rimso-50" (Wilhite & Katz, 1984). The toxicology studies, which demonstrated the perceived safety of DMSO, did not look at long-term effects from brief exposure to the compound. The high doses of DMSO that are tolerated by various application routes have led to DMSO being deemed relatively nontoxic and safe (Table 1) (Leake, 1966). More advanced technology has been developed to examine cellular, epigenetic, and metabolic changes since the 1970s when DMSO was approved by the FDA, so the safety of DMSO in

both the clinical setting and its use in research should be revisited (Crawley, 2004; Yuan et al., 2016).

Autologous stem cell transplants require the use of cryopreservatives to protect cells from freezing damage. DMSO is the standard and most commonly used cryoprotective agent (Al-Anazi, 2012). Hanslik et al. (2009) found that the average dose of DMSO was 0.63 ml/kg when used as a cryoprotectant for medical purposes. When DMSO is transfused into patients, it has several well-identified side effects, including nausea, vomiting, abdominal cramps, and headaches. Acute neurological abnormalities immediately following the infusion of stem cells suspended in the cryopreservative DMSO have been reported in some patients (Chen-Plotkin et al., 2007; Davis et al., 1990; Hanslick et al., 2009; Martin-Henao et al., 2010; Santos et al., 2003).

DMSO is used in the process of *in vitro* fertilization for embryo cryopreservation, as well as the treatment of palmar-plantar erythrodysesthesia syndrome (hand-foot syndrome), which is a common side effect in cancer treatments (Lechpammer et al., 2016). To our knowledge, no papers have been published to examine the behavioral and cognitive effects of neonatal DMSO exposure in rodents. Two published studies have reported behavioral effects in rodents following DMSO exposure; however, these studies were performed in adult rats, and it remained unclear whether DMSO has caused permanent changes in animals (Authier et al., 2002; Fossum et al., 1985). Since fetuses and neonates are exposed to DMSO in the practice of pediatric medicine or during treatment of the mother and through her use of topical products that contain DMSO, we see this practice as a potential area of unrecognized neurotoxicological exposure that might add to psychiatric complications in childhood such as decreased social behavior that could present similar to Asperger's disorder (Verheijen et al., 2019).

The purpose of this study was to assess the effects of DMSO on neonatal male rats following exposures to clinically relevant doses. DMSO exposure was performed during the period of brain development vulnerability in LE neonatal rats, which corresponds to the critical myelination time periods in humans lasting from the last trimester through early childhood (Downes & Mullins, 2014; Semple et al., 2013). To that end, we evaluated the effects of DMSO on metabolome of the brains after short-term neonatal exposure from postnatal days 6–10 (P6–10). Additionally, we assessed chronic changes to behavior, social preferences, and brain morphology in adult rats after neonatal exposure. The limitations of this study are only male rats were used, and longitudinal sampling was not able to be performed to investigate metabolic changes over time. Here, we present the first investigation of DMSO during developmental time periods in rats with follow-up studies later in life.

2 | RESULTS AND DISCUSSION

2.1 | Chronic changes to social behavior later in life after neonatal exposure to DMSO

We evaluated the effects of a five-day, short-term exposure of DMSO during the critical phase of myelination in neonatal Long-Evans (LE)

TABLE 1 LD50 values in g/kg body weight for DMSO (Amended from Leake, 1966)

Species	Dermal	per os	i.v.	s.c.
Application route				
Mouse	50	21–28	4–9	15–25
Rat	40	15–28	5–8	13
Monkey	>11	>10	2–3	—

Note: LD50 values for various species with different application or exposure routes. per os—oral administration; i.v.—intravenous injection; s.c.—subcutaneous injection.

rats (P6–10). DMSO was intraperitoneally (IP) injected twice per day for five days at 0.2, 2.0, and 4.0 ml/kg body mass (Downes & Mullins, 2014). Behavior was assessed at P21 using the open-field locomotion test. Social preferences were assessed at P32 using the three-chambered social approach test. No changes were observed in locomotion behavior as assessed by the open-field test (Figure S1); however, social preferences were altered in the 2.0 and 4.0 ml DMSO/kg groups ($p < .0001$) (Figure 1a). Both groups showed a significant decrease in sociability as indicated by less time spent with a social stimulus (novel rat) than a nonsocial object (empty wire cage). Additionally, in the preference for social novelty, the preference for interacting with a novel rat over a familiar rat was significantly reduced in both the 2.0 ml DMSO/kg group ($p = .004$) and the 4.0 ml DMSO/kg group ($p = .009$) compared with the sham-treated controls (Figure 1b).

These results suggest prolonged effects on behavior and social cognition following brief exposure to DMSO early in life.

2.2 | Astrocytes and microglia increase in a dose-dependent manner following exposure to DMSO

Brain morphology was assessed at P40, 30 days after DMSO exposure was stopped. No gross morphological brain changes were observed. Microglia, astrocytes, and cortical neurons were assessed ($n = 24$, 6 per group). Immunohistochemical analysis of microglia showed a DMSO dose-dependent increase in the number of microglia. Significant increases in Iba-1-expressing microglia were observed in the 4.0 ml DMSO/kg group ($p = .019$) (Figure 2a). Astrocytes (assessed by GFAP stain) had a similar response, and significant increases were observed in the 4.0 ml DMSO/kg group ($p = .0065$) (Figure 2b). No changes were seen in number of cortical neurons (Figure 2c).

Increase in the number of microglia and astrocytes is common following neurological injury. Microglia play a fundamental role in phagocytosis and debris clearance in the CNS via phagocytic clearance by facilitating the reorganization of neuronal circuits and initiating repair mechanisms (Neumann et al., 2009). Chronic assaults to the CNS lead to microglia developing a hypertrophic morphology instead of a retracted or amoeboid morphology. Various mental and behavioral issues are linked to the elevation of hypertrophic microglia (Calcia et al., 2016). The increase in microglia observed after DMSO exposure provides a possible explanation for the alterations in normal behavior and social preferences. Following CNS injury, astrocytes produce cytokines, chemokines, and anti-inflammatory mediators to respond to injured or dying cells (Burda et al., 2016; Llauw et al., 2008). In parallel, large areas of active neural tissue undergo astrogliosis due to the destruction of nearby neurons. The activation of astrocytes following injury leads to increased survival of neurons by extending hypertrophic processes to the traumatized neurons (Bylicky et al., 2018). This cell-cell interaction leads to an increase in glycoproteins and transcriptional activators that lead to axonal sprouting (Campbell et al., 1985; Carmichael et al., 2017). Damaged and destroyed neurons may explain the hypoactive and irregular social preferences and behavior observed in our study.

2.3 | DMSO accumulates in various brain regions

Animals ($n =$ five rats per treatment group, 20 total) were sacrificed for brain metabolome analysis at postnatal day 11 (P11), 24 hr after the administration of DMSO stopped. The presence and abundance of metabolites were assessed by hydrophilic interaction chromatography combined with high-resolution mass spectrometry (HILIC-Q Exactive HF MS/MS, see Method Section). We

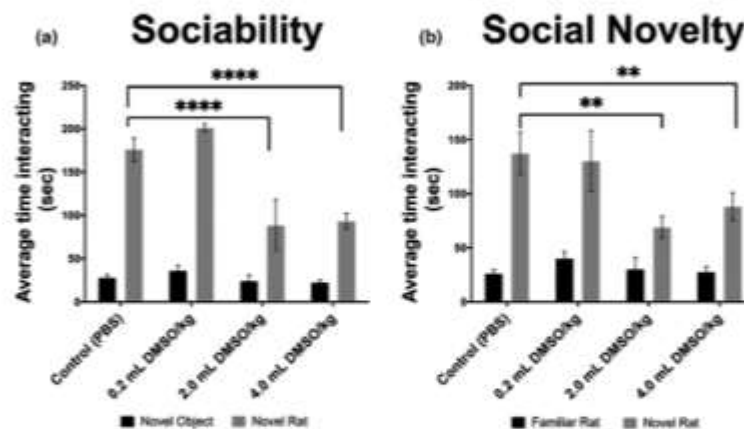


FIGURE 1 Behavior assessment for adult rats following neonatal exposure to DMSO ($n = 30$). Experimental groups were prepared and submitted to behavioral assessments as described in the methods. Depicted are behavioral patterns for sociability and social novelty assessed at P32. Significant decreases in interaction time were observed following DMSO exposure in both the sociability and social novelty test. Values are represented as means \pm SEM; sociability tests for both the 2.0 and 4.0 ml DMSO/kg groups, $p < .0001$. Social novelty tests for the 2.0 ml DMSO/kg group, $p = .0041$, and the 4.0 ml DMSO/kg group, $p = .0085$. ** $p < .01$ versus sham-treated control (PBS); **** $p < .0001$ versus sham-treated control (PBS)

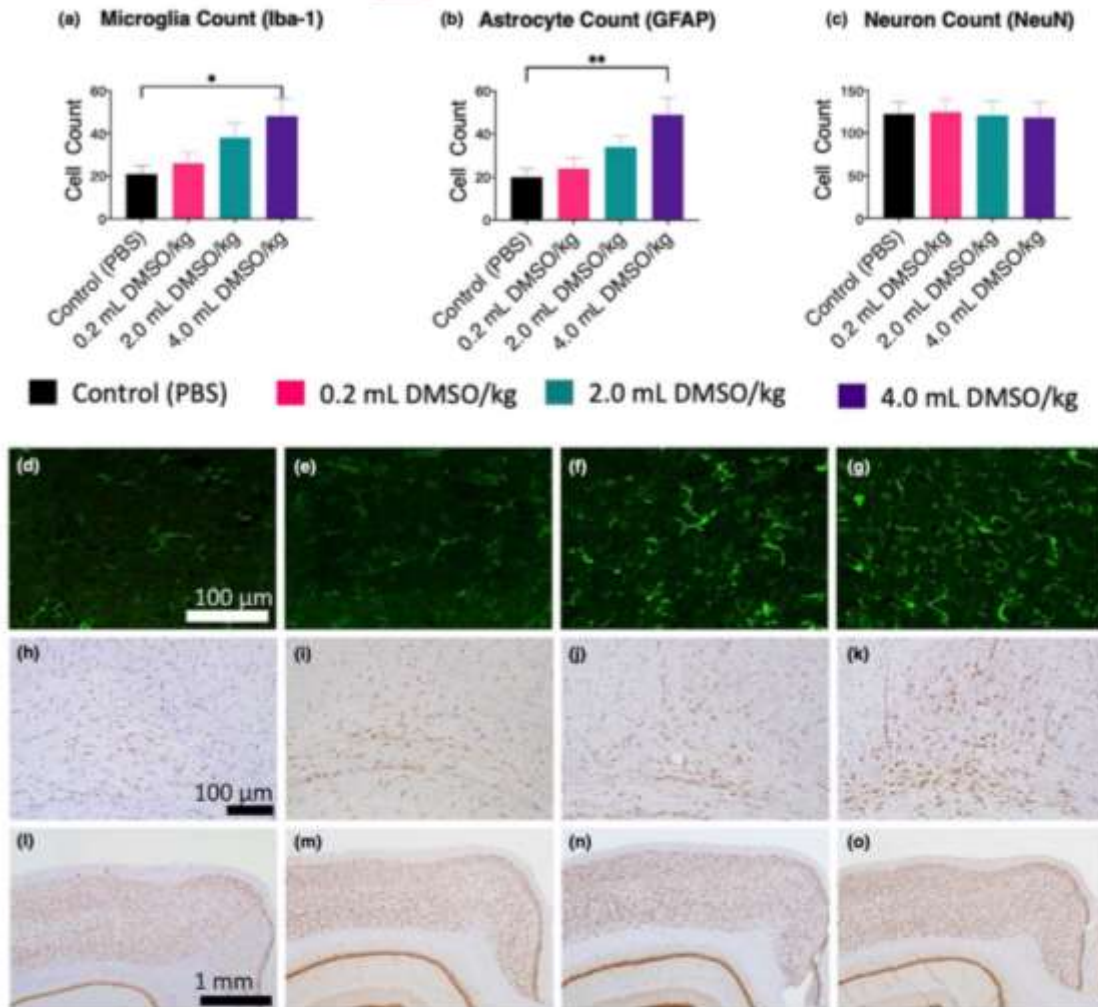
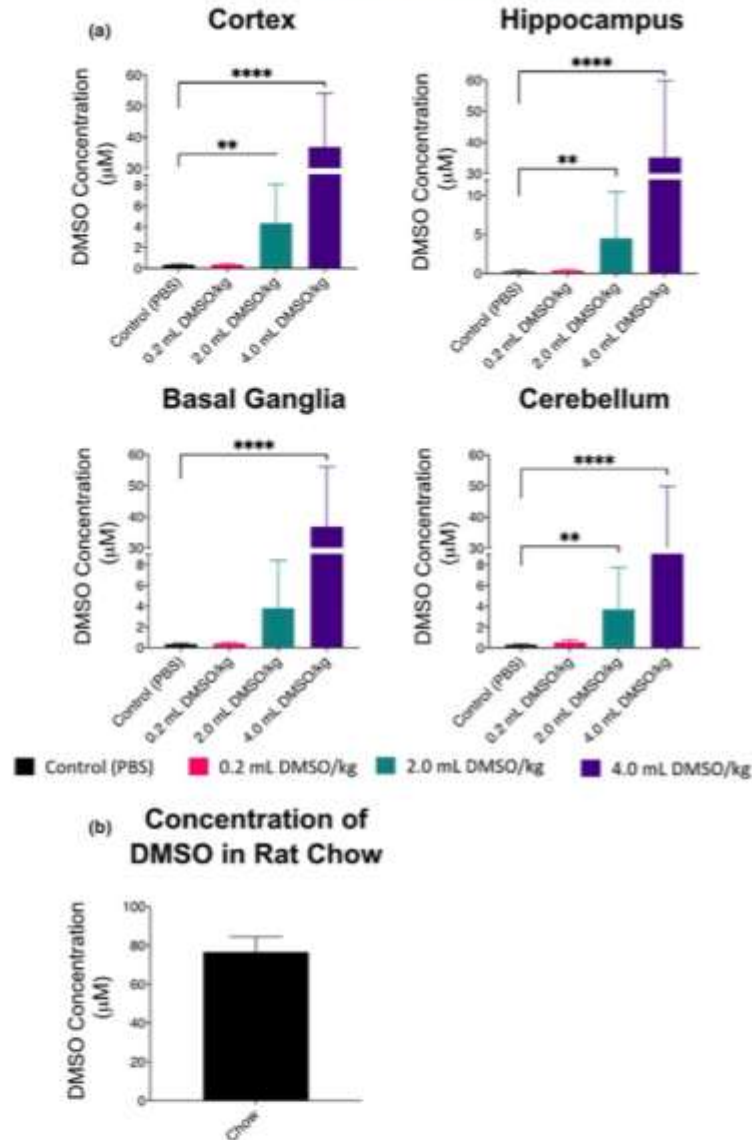


FIGURE 2 Immunohistochemical analysis of microglia, astrocytes, and cortical neurons in adult rats (P40) following neonatal exposure to DMSO at P6-10 ($n = 24$, 6/group). Tissue was collected and prepared as described in the methods. Data were collected in a randomized, blinded manner by two neuroscientists. (a-c) Quantitative analysis of microglia, astrocytes, and neurons. (d-g) Representative immunohistochemical stains showing an increase in microglia (Iba-1 stain) with increasing DMSO doses; (d) control; (e) 0.2 ml DMSO/kg; (f) 2.0 ml DMSO/kg; (g) 4.0 ml DMSO/kg (size bar = 100 μ m). (h-k) Representative immunohistochemical stains showing an increase in astrocytes (GFAP stain) with increasing DMSO doses; (h) control; (i) 0.2 ml DMSO/kg; (j) 2.0 ml DMSO/kg; (k) 4.0 ml DMSO/kg (size bar = 100 μ m). (l-o) Representative immunohistochemical stains showing no change in cortical neurons (NeuN stain) with exposure to DMSO; (l) control; (m) 0.2 ml DMSO/kg; (n) 2.0 ml DMSO/kg; (o) 4.0 ml DMSO/kg (size bar = 1 mm). Values are represented as means \pm SEM; * $p < .05$ versus sham-treated control (PBS); ** $p < .01$ versus sham-treated control (PBS)

first investigated the data set for the detection of the target molecule DMSO. DMSO was detected in tissue from all four analyzed brain regions: cortex, hippocampus, basal ganglia, and cerebellum. We found increasing, dose-dependent mean levels of DMSO in the different brain regions ranging from 0.3 to 0.5 μ M DMSO in the 0.2 ml DMSO/kg group to 3-4 μ M DMSO in the 2.0 ml DMSO/kg group and finally 27-37 μ M DMSO in the 4.0 ml DMSO/kg group. DMSO was significantly higher in the 4.0 ml/kg groups of

all four analyzed brain regions ($p < .0001$) and significantly higher in the 2.0 ml/kg group in the cortex, hippocampus, and cerebellum ($p < .001$) compared with the controls. Interestingly, even the sham-treated control group showed low levels of DMSO present as well, with a mean concentration of 0.3 μ M DMSO for all regions (Figure 3a). We investigated the origin of DMSO in untreated rats and found that the rat chow itself contained 76 μ M DMSO (Figure 3b). Interestingly, as these were neonatal animals and still

FIGURE 3 Quantification of DMSO by HILIC-Q Exactive HF MS/MS in the brain 24 hr after exposure ($n = 20$, 5 per group). (a) Concentration of DMSO by region and dose. (b) Concentration of DMSO in standard chow; values are represented as means \pm SEM; ** $p < .01$ versus control (PBS); **** $p < .0001$ versus control (PBS)



nursing, only the dam was ingesting the chow, and thus, the DMSO was transmitted via dam's milk.

Through IP administration, DMSO is absorbed into the mesenteric blood supply and then carried to the liver and subjected to hepatic metabolism. The amount of DMSO that was passed from the dam to the pups via milk is unknown. DMSO levels detected in the brains of the control rats were likely transported through small intestinal absorption from chow in the dam, and then metabolized in the liver before passing to the bloodstream, and, ultimately, the dam's milk. The DMSO detected in the control pups likely derived from gastrointestinal absorption of the dam's milk, which was introduced due to maternal consumption of the chow (Turner et al., 2011).

Our results reported here expand on the prior work that investigated DMSO levels in plasma after exposure. Yellowlees et al. (1980) found that an oral dose of 1 g DMSO/kg body weight (0.91 ml DMSO/kg) resulted in peak plasma concentrations in 4 to 6 hr, with detectable levels present for 400 hr (Yellowlees et al., 1980). Our findings support reports by Hanslick et al. (2009) who observed differences in relative degeneration severity of different brain regions, suggesting that cell-specific transporters may play a crucial role in responding to the damage induced by DMSO (Hanslick et al., 2009).

We found that the 0.2 ml DMSO/kg group had nearly the same levels of DMSO incorporated as the sham-treated animals. As our

Instruments were sensitive enough to detect even minute quantities of DMSO (Figure S2), we hypothesize that there might be an inflection point of the glymphatic and circulatory system that clears low amounts of DMSO from the brain as the relationship between administered DMSO and DMSO found in regions of the brain seems characteristic of a saturation curve, where uptake and clearance are not proportional.

2.4 | The brain metabolome is drastically altered by low doses of DMSO

Four regions of the rats' brain (cortex, hippocampus, basal ganglia, and cerebellum) were macrodissected and analyzed at P11 ($n = 20$, 5 per group) for metabolic alterations following five days of DMSO exposure. These regions were chosen for their well-defined

functions related to behavior, social interactions, and motor functions. Metabolic alterations were assessed by using hydrophilic interaction liquid chromatography coupled to orbital ion trap MS/MS (HILIC-Q Exactive HF MS/MS). 483 structurally identified metabolites were detected by matching retention times, accurate mass, and MS/MS spectra to authentic compounds and entries in the MoNA and NIST17 databases. Data have been uploaded to the NIH MetabolomicsWorkbench.org database.

Principle component analysis (PCA) shows that DMSO had significant global effects on the metabolic network of the brain following any exposure to DMSO (Figure 4a). PCA shows dose-dependent effects on the brain metabolome in each specific region (Figure 4c), and large effects were seen when analyzing only significant metabolites compared with sham-treated control for each region and dose (Figure 53). In the 0.2 ml/kg group, the most affected brain region

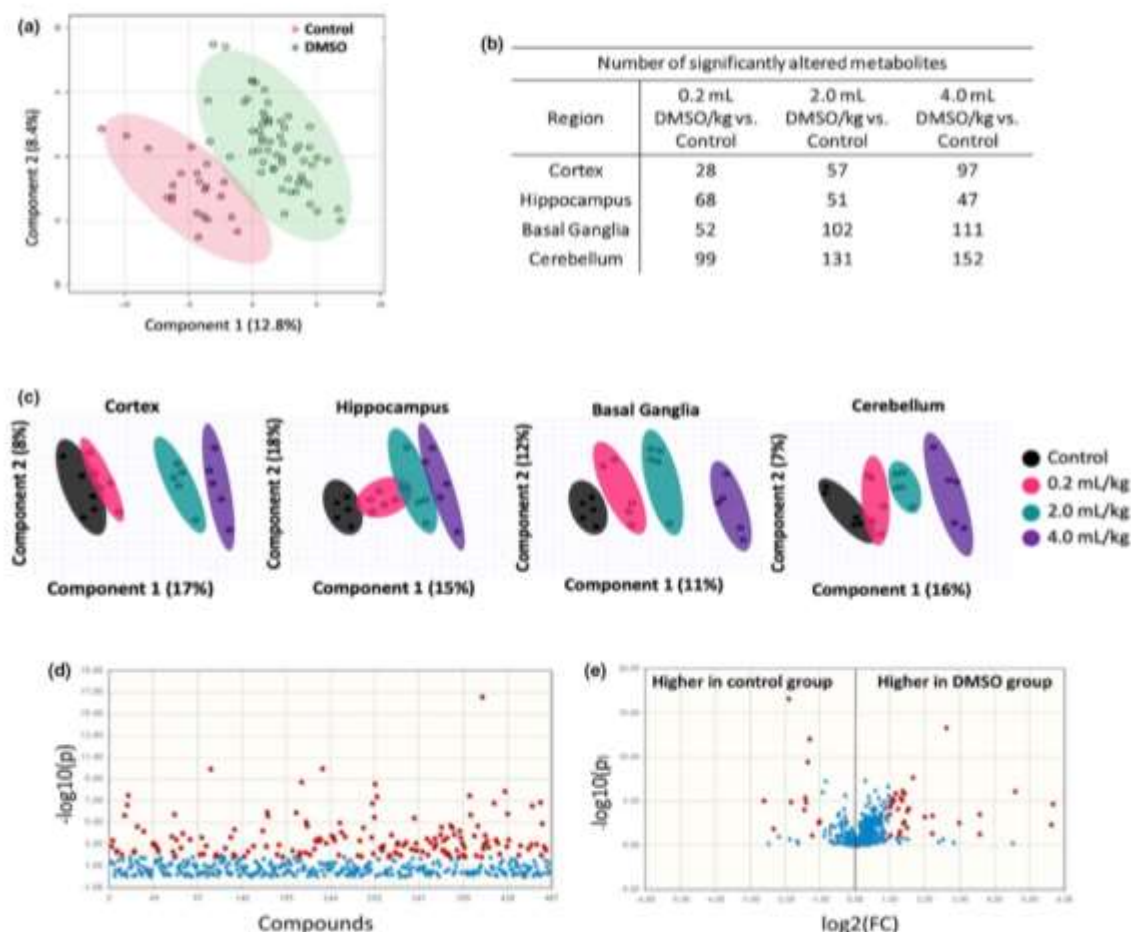


FIGURE 4 Summary of metabolites in the brain 24 hr after DMSO exposure using HILIC analysis ($n = 20$, 5 per group). (a) Principal component analysis of DMSO-treated animals and controls. (b) Number of significantly altered metabolites by dose and region. (c) Principal component analysis of brain region and treatment. (d) Manhattan plot of metabolites of all DMSO doses and regions compared with control. Compounds in red represent metabolites with $p < .05$. (e) Volcano plot of metabolites of all DMSO doses and regions compared with control. Compounds in red represent metabolites with FDR-adjusted $p < .05$.

was the cerebellum with 99 altered compounds, followed by the hippocampus, basal ganglia, and cortex (Figure 4b). To investigate metabolites that were changed with any exposure to DMSO, regardless of region, a Wilcoxon rank-sum test was performed (Figure 4d). 164 of the 483 metabolites were altered under DMSO treatment in at least one brain region at $p < .05$. Treatment with DMSO at any dose presented multiple significantly altered metabolites following false discovery rate (FDR) adjustment, including many compounds with more than twofold changes when compared to the sham-treated controls (Figure 4e). Metabolic alterations varied based on dose and brain region, suggesting dose-dependent and microenvironment effects.

Metabolites were grouped into different clusters based on their structure in order to perform chemical enrichment analysis. This clustering showed consistent changes in metabolites involved in

DNA damage pathways, oxidative stress, and noncanonical metabolites. Metabolites in these clusters were further investigated to provide possible mechanistic explanations of the behavioral and cellular changes we observed.

Nucleosides, amino acids, and oxidized metabolites showed clear dose responses and directions of regulation across the four brain regions (Figure 5). Interestingly, metabolites did not have the same response following DMSO exposure in the brain's different regions, exemplifying the spatial differences in the brain metabolome and microenvironment effects. Threonine and alanine are two examples of metabolites showing differential response by region. While both metabolites increase in a dose-dependent fashion with DMSO, threonine is only statistically different in the cerebellum for all groups compared with the control, and alanine is only statistically altered in the highest dose of DMSO in the basal ganglia in

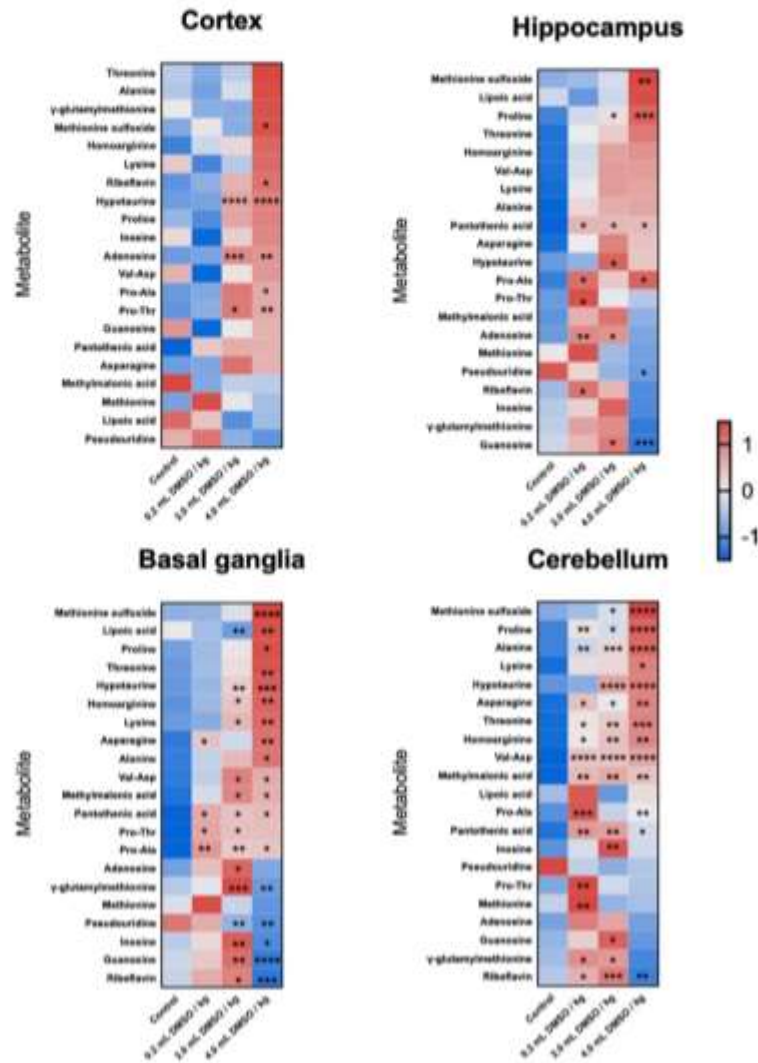


FIGURE 5 Heat map visualization of metabolites involved in nucleic acid and protein metabolism in the brain 24 hr after DMSO exposure ($n = 20$, 5 per group) measured using HILIC-Q Exactive HF MS/MS following Z-score transformation. p -values for each metabolite are indicated by asterisks. Averages for each compound are shown to indicate fold change magnitude and direction. * $p < .05$ versus control (PBS); ** $p < .01$ versus control (PBS); *** $p < .001$ versus control (PBS); **** $p < .0001$ versus control (PBS)

addition to all treatment groups compared with the control group for the cerebellum. Epimetabolites such as pseudouridine are physiologically active molecules generated from adjacent canonical metabolites (Showalter et al., 2017; Zhao & He, 2015). Pseudouridine levels decreased in a dose-dependent manner with DMSO exposure in the hippocampus, basal ganglia, and cerebellum, while levels in the cortex remained fairly constant. Guanosine had a similar trend of decreased levels in all regions of the brain following DMSO exposure. Guanosine is a neuroprotective metabolite that activates intra- and extracellular signaling pathways that regulate CNS functions, behavioral responses, and neuronal plasticity (Di Liberto et al., 2016). Hence, decreases in guanosine levels may have contributed to the behavioral dysfunction observed. Conversely, levels of other nucleoside and nucleotide moieties were increased in the brain following DMSO exposure (Figure 5). Protein and amino acid levels in cells are in a state of dynamic equilibrium. Increases in amino acids and dipeptides may be the result of enhanced proteasomal degradation caused by the misfolding or loss of protein structure (proteopathy) and cellular stress (Chen et al., 2017). Similarly, differences in nucleoside levels may point to dysregulation of RNA and DNA homeostasis. It was found previously that DMSO can decrease the stability of RNA and proteins by decreasing conformational structure (Tunçer et al., 2018). Verheijen et al. (2019) showed that over 2,000 microRNAs were altered when cells were exposed to as little as 1% DMSO in culture, which supports our hypothesis that DMSO induces degradation of protein and nucleic acid structures. The increase in oxidized metabolites (methionine sulfoxide and hypoxanthine) suggests that the increase in amino acids and dipeptides is due to the degradation of proteins due to loss of structure (Figure 5).

Microglia act as the resident macrophages in the central nervous system, and an increase in protein and nucleic acid catabolism would lead to cell stress, resulting in the need to clear cellular debris. An increase in catabolic debris and oxidative stress has been shown to correlate with an increase in microglia (Rojo et al., 2014). Our data showing the activation of microglia (Figure 2) support the possibility of DMSO causing oxidative stress in the brain.

Our metabolomic data showed large changes in retinoic acid (RA), the biologically active form of vitamin A, which plays a key role in gene expression, cell growth, and overall brain development. Retinoid signaling synchronizes cortical neuronal activity between separate locations in the brain, a critical phenomenon responsible for influencing sleep, memory, and learning (Dräger, 2006). RA is critical for neuronal survival and promotes antiapoptotic and pro-proliferative activity through various pathways (Wagner et al., 2002). We have found that total RA levels have significantly decreased in a dose-dependent manner in all DMSO treatment groups ($p < .0001$) (Figure 6a). RA levels were significantly decreased in all DMSO treatment groups in the hippocampus ($p < .01$), and basal ganglia ($p < .001$), and in the 2.0 and 4.0 ml/kg DMSO groups in the cerebellum ($p < .03$) (Figure 53a). While mechanisms have not yet been fully elucidated on how RA modulates neuronal pathways, it is hypothesized that the RA receptors or retinoid X receptors form a ligand complex and dimerize, allowing for the activation and modulation of neuronal differentiation (Jang et al., 2004). It is unclear whether the decreased levels of RA observed following DMSO exposure are due to RA acting as a ligand and being modified to retinyl esters to assist neuronal and glial cells in combating oxidative stress from DMSO, or whether RA was degraded by cytochrome p enzymes as previously described (Duester, 2008). Normal levels of RA activate the peroxisome proliferator response element of certain genes to increase protein levels of two

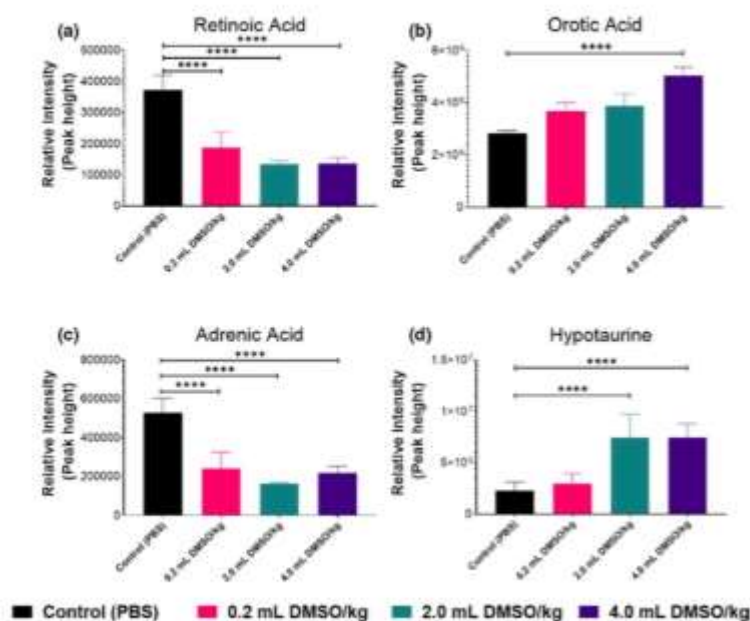


FIGURE 6 Effects of DMSO on (a) retinoic acid, (b) orotic acid, (c) adrenic acid, and (d) hypotaurine levels in whole brain following using HILIC-Q Exactive HF MS/MS. Data are means \pm SEM of metabolite abundance ($n = 20$, 5 per group). **** $p < .0001$ versus control (PBS)

superoxide dismutase isoforms and to preserve glial and neuronal cells from oxidative damage (Ahlemeyer et al., 2001). The marked decreased RA following exposure to DMSO in all assessed brain regions suggests DMSO causes oxidative damage, resulting in cellular stress and apoptosis, leading to the activation of microglia and astrocytes.

The nucleoside pathway precursor orotic acid (OA) was elevated in a dose-dependent manner in all brain regions following the administration of DMSO and significantly increased in the 4.0 ml/kg treatment group ($p < .0001$) (Figure 6b). OA was significantly altered in the 4.0 ml DMSO/kg group in the cortex ($p = .041$), cerebellum ($p = .0053$), and basal ganglia ($p = .0287$) (Figure S3b). OA is produced in the mitochondria by dihydroorotate dehydrogenase, or in the cytoplasm by the pyrimidine synthesis pathway (Rawls et al., 2000). OA enables astrocytes to carry out normal aerobic metabolism even when cells were cultured under hypoxic conditions, indicating the importance of this metabolite in promoting neuronal survival during central nervous system insults or injuries (Sonnewald et al., 1998). Increased OA levels may be linked to the increase in astrocytes we observed. Furthermore, it provides an explanation on why no changes were seen in the number of neurons following brief CNS injury.

Adrenic acid (AdA) is a naturally occurring polyunsaturated fatty acid and one of the most abundant fatty acids in the developing human brain. AdA was significantly decreased in all regions following the administration of DMSO at all exposure levels (Figure 6c). AdA was significantly altered in the 4.0 ml DMSO/kg groups in the cortex ($p = .041$), cerebellum ($p = .0053$), and basal ganglia ($p = .0287$) (Figure S3c). In the brain, AdA is mainly found in myelin tissue (Martinez, 1992). AdA is formed by a 2-carbon elongation of arachidonic acid and is further metabolized to bioactive compounds such as dihomoprostaglandins and dihomio-EETs (Campbell et al., 1985; Yi et al., 2007). The marked decrease in AdA following brief DMSO exposure provides mechanistic insights and supports our observations in both behavioral changes and activation of microglia and astrocytes. Since DMSO exposure was carried out during the critical period of myelination in the neonatal LE rats and no changes in the number of neurons were observed, the decrease in this critical component of myelin warrants further investigation of neuronal developmental process (Duester, 2008).

Hypotaurine was consistently elevated in all regions following the administration of DMSO at 2.0 and 4.0 ml/kg doses ($p < .0001$) (Figure 6d). Hypotaurine was significantly altered in the 2.0 and 4.0 ml DMSO/kg groups in the cortex and cerebellum ($p < .0001$), in the 2.0 ml DMSO/kg group in the hippocampus ($p = .0055$), and in the 4.0 ml DMSO/kg group in the basal ganglia ($p = .0047$) (Figure S3d). Hypotaurine is an antioxidant that has been shown to increase the proliferation of cells and increase mitochondrial activity (Ha et al., 2016). Interestingly, DMSO leads to the collapse of the mitochondrial membrane potential, decreasing electron transport chain efficacy. The increased levels of hypotaurine may counteract the oxidative effects of DMSO in order to attempt to maintain normal cellular functions (Liu et al., 2001).

The alterations of metabolites discussed above suggest dysregulation of protein and nucleic acid metabolism in the brain following DMSO exposure in infancy. Alterations to RA and OA further

support the notion of oxidative damage following brief DMSO exposure, which may be linked to glial cell signaling and activation. Alterations of AdA provide some insight into possible mechanism of damage to myelin, leading to the changes in behavior observed later in life after brief DMSO exposure in infancy.

3 | CONCLUSION

DMSO is a by-product of algal metabolism and has been documented to be present in very low levels of fruit, but is mainly an additive in topical lotions and a cryopreservative for various medical applications (Pearson et al., 1981). Here, we unequivocally show that the administration of DMSO at previously regarded safe concentrations causes significant changes to brain biochemistry and cellular and behavioral patterns in LE rats. We observed that exposure to DMSO by IP injection at any of the low doses used resulted in global changes to the brain metabolome and an increase in both oxidative stress markers (taurine, hypotaurine, methionine sulfoxide) and proteolysis markers (dipeptides). The nonlinear relationship between DMSO administered and DMSO concentration present in the brain suggests that the glymphatic system is able to clear low levels of DMSO, but reaches a saturation point and is then unable to clear the compound. Additionally, behavioral tests in the 2.0 and 4.0 ml DMSO/kg groups have revealed hypoactive exploratory behavior and decreased social habits. Finally, we have observed a significant increase in microglia and astrocytes in brains of young adult rats following brief exposure as neonates, suggestive of chronic CNS damage (Figure 7).

We therefore propose that DMSO might be of concern in clinical practice and studies. For example, a noninterventional study carried out in 64 European centers for transplants of myeloma and leukemia showed that 95% of transplanted cells did not have DMSO removed prior to transfusion. Patients received an average of 22.6 ml over the course of two days, which equated to 0.3 ml DMSO/kg of body weight (Morris et al., 2014). Moreover, DMSO is the most common vehicle for drug delivery in high-throughput screening models (Kenny et al., 2015). Future studies should focus on what effects sex might have on DMSO exposure and how much DMSO is absorbed from the diet in research animals. Investigation of resting and active microglia could be expanded to understand the role of glial cells following exposure; all points beyond the scope of this manuscript. Our novel findings reported here challenge the broadly perceived relative safety of low concentrations of DMSO, while observed neurotoxicity should be considered in future human medical applications and clinical trials to prevent possible chronic morphological and neurocognitive sequelae of its use.

4 | MATERIALS AND METHODS

4.1 | Animal experiments

Adult female Long-Evans rats and their male pups (P4) were obtained from Charles River Laboratories. Male rats were used in order

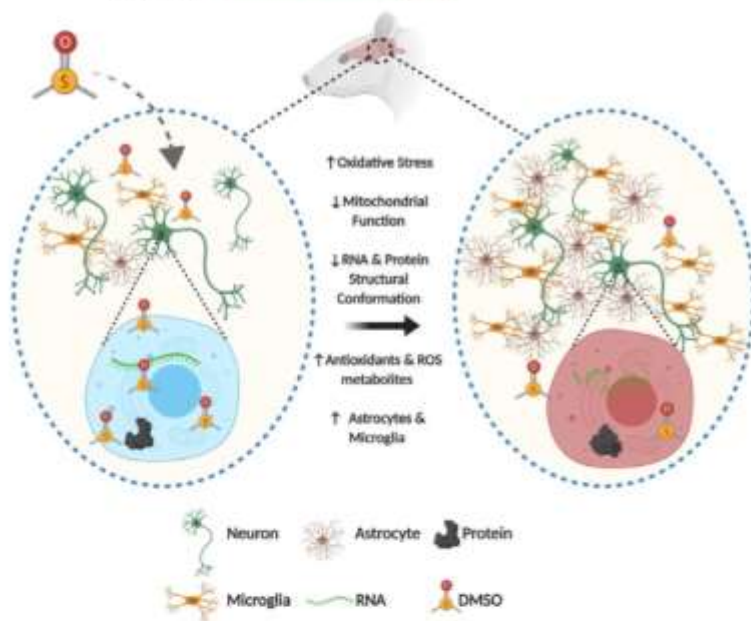


FIGURE 7 Summary of cellular and metabolic brain changes following brief exposure to DMSO

to compare our results with previously published studies that did look at the effect of DMSO exposure in female animals (Fontoura-Andrade et al., 2017). Litters were acclimatized for 48 hr before experiments began. Treatments were distributed between preweaned litters to control for potential litter variables. Litters (i.e., dam with up to 10 pups) were individually caged under controlled temperature ($22 \pm 2^\circ\text{C}$) with 12-hr light cycles (light 6 a.m.–6 p.m.; dark 6 p.m.–6 a.m.). Rat pups received IP injection with either PBS (Sigma-Aldrich, St. Louis, MO) or DMSO (0.2, 2.0, or 4.0 ml/kg; $\geq 99.7\%$ Hybri-Max DMSO, Sigma-Aldrich, St. Louis, MO). DMSO doses were chosen following an extensive literature search for common doses, and while not much was reported for animal experiments or in vivo studies, a 2014 report from the European Group for Blood and Marrow Transplantation documented the average dose humans received was 0.303 ml/kg body weight (± 0.277 ml/kg) (Morris et al., 2014), and Long-Evans rat pups received IP injection twice a day from P6 to P10. One cohort ($n = 5$ per group, a total of 20 animals) was sacrificed at P11. Brains were macrodissected into regions—cortex, basal ganglia, hippocampus, and cerebellum—and then snap-frozen in liquid nitrogen and stored at -80°C until extracted for metabolomic analysis. All animals were sacrificed on the same day, and tissue was collected for each animal after cervical decapitation. The entire process took one hour, between 11 a.m. and noon, in order to minimize any diurnal fluctuation of metabolites in the brain. Animals were randomly selected, blocked by treatment group, for the order they were sacrificed. A second cohort was weaned off their dams at P20. Locomotion and behavioral assays were performed in a blinded fashion as previously described at P21 and P32 (Lechpammer et al., 2017). Animals were sacrificed at P40, and brains were preserved for morphological and histochemical

analysis. All animal procedures were performed in accordance with the standards approved by the UC Davis Institutional Animal Care and Use Committee (IACUC #17420).

4.2 | Open-field locomotion test

The locomotor behavioral test measures animal exploration in an open-field enclosure to assess the animal's level of anxiety or changes to their behavior (Schmitt & Hiemke, 1998). Prior to the test, each animal was introduced in the center of a 100×100 cm square enclosed by Plexiglas and allowed to habituate in the environment for 30 min. A day after habituation, each animal was individually placed into the same apparatus and monitored for 30 min using an overhead camera and the ANY-maze Video Tracking System (ANY-maze; Stoelting, Wood Dale, IL) (Crawley, 2004). The software recorded the number of times the animal entered the center zone, the animal's mean speed, the time the animal spent in the center, and the time the animal spent in the perimeter. In between trials, the chamber was cleaned with 70% ethanol.

4.3 | Three-chamber social choice test

Rat social behaviors were observed using "Social Approach" and "Social Novelty" tests adapted from Moy et al. (2004) as described previously by Lechpammer et al. (2017) (Lechpammer et al., 2017; Moy et al., 2004). The test apparatus was composed of two circular cages placed at the ends of a three-chambered, Plexiglas enclosure (100×100 cm, with chambers 100×33 cm). The cages, 13.3 cm in

diameter and 21 cm in height, had metal rods spaced 0.5 cm apart to allow interaction between the animal and a caged "stranger" animal. Rectangular openings between the chambers allowed the animal to move freely around the enclosure during tests.

For the social approach test, each animal was first habituated in the empty three-chambered enclosure for five minutes. After habituation, the animal was removed, and cages were placed in the end chambers, one containing a same-sex stranger rat, and the other left empty. The test animal was reintroduced in the center chamber and allowed to explore the enclosure for 10 min. An overhead camera and ANY-maze software tracked time spent in each chamber. Time spent interacting with the stranger rat and the empty cage was also recorded. The expected behavior of a control rat would be to spend more time in the chamber with the stranger.

For the recognition of social novelty test, the test animal was removed from the apparatus and a novel same-sex stranger was placed in the previously empty cage. The test animal was reintroduced to the center chamber and allowed to explore the enclosure for an additional 10 min. The same data were recorded for the test through the ANY-maze software. The expected behavior of a control rat would be to spend more time in the chamber with the novel stranger. In between trials, the chamber and caged cylinders were cleaned with 70% ethanol.

4.4 | Brain morphology

Serial 20- μ m coronal sections were cut by cryostat from the anterior extent of the lateral ventricles through the posterior extent of the dorsal hippocampus. Coronal sections at the level of the mid-dorsal hippocampus were examined. Representative sections of the parietal cortex and white matter were stained by hematoxylin and eosin (H&E) or immunohistochemical and immunofluorescent labeling, as previously published (Kim et al., 2015; Lechpammer et al., 2008, 2016). Microphotographs were taken at 200x magnification, and two blinded neuroscientists counted number of immunolabeled cells.

4.5 | Metabolomic sample preparation

Metabolites were extracted from macrodissected fresh brain tissue ($n = 5$ for each group) as described previously (Barupal et al., 2019). Briefly, 6 mg of tissue was homogenized using 3.2-mm-diameter stainless steel beads ground using a GenoGrinder for 50 s at 1,500 rpm. Ground tissues were then extracted using 225 μ l cold methanol containing a mixture of deuterated internal standard water and methyl tert-butyl ether, as adapted from Matyash (Matyash et al., 2008). Ten method blanks were extracted and analyzed at the same time as the samples. The polar fraction of methanol and water was dried under vacuum and reconstituted in 110 μ l of 80:20 (v/v) acetonitrile: water containing 34 deuterated internal standards. Samples were then vortexed, sonicated, and centrifuged prior to analysis.

4.6 | LC-MS data acquisition

Hydrophilic interaction liquid chromatography (HILIC) was used as previously described (Showalter et al., 2018). Briefly, HILIC analysis was performed using a Vanquish UHPLC coupled to a Q-Exactive HF orbital ion trap mass spectrometer (Thermo Fisher Scientific, San Jose, CA). Chromatographic separation was achieved using a Waters BEH Amide column under the following chromatographic conditions: Mobile phase A consisted of 100% water with 10 mM ammonium formate and 0.1% formic acid. Mobile phase B was 80:20 acetonitrile: water with 10 mM ammonium formate and 0.1% formic acid. Gradients were run from 0 to 2 min at 100%B; 2-7.70 min to 70%B; 7.70-9.5 to 40%B; 9.5-10.25 min to 30%B; and 10.25-12.75 min of increase back to 100%B with column equilibration from 12.75 to 16.75 min at 100%B. The flow rate was 0.400 ml/min. The column was heated to 40°C. 5 μ l of the sample was injected onto the column for analysis in both polarity modes. Data were collected from 120 to 1,200 m/z in a data-dependent manner with the top four ions from each MS1 scan being selected for MS/MS fragmentation. Samples were randomized prior to injection with method blanks, and QC samples were analyzed between every ten study samples.

4.7 | Data processing and statistics

Data processing was performed using MS-DIAL v3.90 (Tsugawa et al., 2015). Raw data are available on the Metabolomics Workbench. Compounds were identified by matching retention times and experimental spectra downloaded from the HILIC-MS/MS database in MassBank of North America in addition to NIST17 MS/MS spectra. For statistical analysis, samples were normalized to the sum of all identified metabolites. Heat maps were generated using GraphPad Prism v8.4.0. Heat map values are Z-scores of each metabolite. Z-scores were calculated by subtracting the mean of the group values and then dividing by the standard deviation in order to scale the data for relative expression for each region. Line graphs and violin plots were generated using GraphPad Prism v8.4.0. All p -values listed for metabolites are normalized raw p -values. PCA, Wilcoxon rank-sum test, and volcano plots were generated using MetaboAnalyst v4.0. False discovery rate (FDR) adjustment was used to correct for multiple comparisons in the volcano plot. For animal experiments and immunohistochemistry data, statistical analysis was carried out using GraphPad Prism v8.4.0. All values are expressed as mean \pm SEM. Groups were compared using the one-way ANOVA test with the multiple comparison post hoc tests. $p \leq .05$ were considered statistically significant.

ACKNOWLEDGMENTS

Data were previously presented in part at the American Association of Neuropathologists 95th Annual Meeting, Atlanta, GA, 6-9 June 2019.

CONFLICT OF INTEREST

The authors declare no conflict of interests.

AUTHOR CONTRIBUTIONS

Zach Rabow conceptualized the data, involved in formal analysis, investigated the data, curated the data, wrote original draft, and visualized the data; **Taryn Morningstar** involved in formal analysis, investigated the data, involved in behavioral studies, curated the data, and visualized the data; **Megan Showalter** involved in formal analysis and curated the data; **Hailey Heil** curated the data; **Krista Thongphanh** involved in formal analysis, investigated the data, and involved in behavioral studies; **Joanne Chan** investigated the data; **Sili Fan** involved in formal analysis and visualized the data; **Verónica Martínez-Cerdeño** provided software, involved in behavioral studies, and provided resources; **David Zagzag** conceptualized the data, designed methodology, and wrote and edited the manuscript. **Robert Berman** involved in behavioral studies and provided resources; **Evgeny Nudler** conceptualized the data, designed methodology, provided resources, and acquired funding; **Oliver Fiehn** conceptualized the data, designed methodology, provided software, provided resources, wrote, reviewed, and edited the manuscript, supervised the data, administered the project, and acquired funding; **Mirna Lechpammer** conceptualized the data, designed methodology, provided software, involved in behavioral studies, provided resources, wrote, reviewed, and edited the manuscript, supervised the data, administered the project, acquired funding.

ETHICAL APPROVAL

The vertebrate animal protocol used in this study was approved by an Institutional Animal Care and Use Committee (IACUC) at the University of California, Davis (Protocol Number: 17420).

DATA AVAILABILITY STATEMENT

The data that support the findings of this study are available from the corresponding author upon reasonable request.

ORCID

Zachary Rabow  <https://orcid.org/0000-0001-6213-4950>

Megan Showalter  <https://orcid.org/0000-0002-3506-5483>

Verónica Martínez-Cerdeño  <https://orcid.org/0000-0002-9613-3603>

Oliver Fiehn  <https://orcid.org/0000-0002-6261-8928>

Mirna Lechpammer  <https://orcid.org/0000-0002-6235-6227>

REFERENCES

- Ahlemeyer, B., Bauerbach, E., Plath, M., Steuber, M., Heers, C., Tegtmeier, F., & Kriegstein, J. (2001). Retinoic acid reduces apoptosis and oxidative stress by preservation of SOD protein level. *Free Radical Biology and Medicine*, 30(10), 1067-1077. [https://doi.org/10.1016/S0891-5849\(01\)00495-6](https://doi.org/10.1016/S0891-5849(01)00495-6)
- Al-Anazi, K. A. (2012). Autologous hematopoietic stem cell transplantation for multiple myeloma without cryopreservation. *Bone Marrow Research*, 2012, 1-7. <https://doi.org/10.1155/2012/917361>

- Authier, N., Dupuis, E., Kwasiborski, A., Eschalier, A., & Coudoré, F. (2002). Behavioural assessment of dimethylsulfoxide neurotoxicity in rats. *Toxicology Letters*, 132(2), 117-121. [https://doi.org/10.1016/S0378-4274\(02\)00052-8](https://doi.org/10.1016/S0378-4274(02)00052-8)
- Barupal, D. K., Zhang, Y., Shen, T., Fan, S., Roberts, B. S., Fitzgerald, P., Wancewicz, B., Valdiviez, L., Wohlgemuth, G., Byram, G., Choy, Y. Y., Haffner, B., Showalter, M. R., Vaniya, A., Blossiez, C. S., Folz, J. S., Kind, T., Flenniken, A. M., Mckerlie, C., ... Fiehn, O. (2019). A comprehensive plasma metabolomics dataset for a cohort of mouse knockouts within the international mouse phenotyping consortium. *Metabolites*, 9(5), 101. <https://doi.org/10.3390/metabo9050101>
- Brown, F. D., Johns, L. M., & Mullan, S. (1980). Dimethyl sulfoxide in experimental brain injury, with comparison to mannitol. *Journal of Neurosurgery*, 53(1), 58-62. <https://doi.org/10.3171/jns.1980.53.1.0058>
- Burda, J. E., Bernstein, A. M., & Sofroniew, M. V. (2016). Astrocyte roles in traumatic brain injury. *Experimental Neurology*, 275, 305-315. <https://doi.org/10.1016/j.expneurol.2015.03.020>
- Bylicky, M. A., Mueller, G. P., & Day, R. M. (2018). Mechanisms of endogenous neuroprotective effects of astrocytes in brain injury. *Oxidative Medicine and Cellular Longevity*, 2018, 1-16. <https://doi.org/10.1155/2018/6501031>
- Calcia, M. A., Bonsall, D. R., Bloomfield, P. S., Selvaraj, S., Barichello, T., & Howes, O. D. (2016). Stress and neuroinflammation: A systematic review of the effects of stress on microglia and the implications for mental illness. *Psychopharmacology (Berl)*, 233(9), 1637-1650. <https://doi.org/10.1007/s00213-016-4218-9>
- Camp, P., James, H., & Werner, R. (1981). Acute dimethyl sulfoxide therapy in experimental brain edema: Part 1: Effects on intracranial pressure, blood pressure, central venous pressure, and brain water and electrolyte content. *Neurosurgery*, 9(1), 28-33. <https://doi.org/10.1227/00006123-198107000-00005>
- Campbell, W. B., Falck, J. R., Okita, J. R., Johnson, A. R., & Callahan, K. S. (1985). Synthesis of dihomoprostaglandins from adrenic acid (7,10,13,16-docosatetraenoic acid) by human endothelial cells. *Biochimica et Biophysica Acta (BBA) - Lipids and Lipid Metabolism*, 837(1), 67-76. [https://doi.org/10.1016/0005-2760\(85\)90086-4](https://doi.org/10.1016/0005-2760(85)90086-4)
- Carmichael, S. T., Kathirvelu, B., Schweppe, C. A., & Nie, E. H. (2017). Molecular, cellular and functional events in axonal sprouting after stroke. *Experimental Neurology*, 287, 384-394. <https://doi.org/10.1016/j.expneurol.2016.02.007>
- Chen, L., Brewer, M. D., Guo, L., Wang, R., Jiang, P., & Yang, X. (2017). Enhanced degradation of misfolded proteins promotes tumorigenesis. *Cell Reports*, 18(13), 3143-3154. <https://doi.org/10.1016/j.celrep.2017.03.010>
- Chen-Plotkin, A. S., Vessel, K. A., Samuels, M. A., & Chen, M. H. (2007). Encephalopathy, stroke, and myocardial infarction with DMSO use in stem cell transplantation. *Neurology*, 68(11), 859-861. <https://doi.org/10.1212/01.wnl.0000256716.04218.5b>
- Crawley, J. N. (2004). Designing mouse behavioral tasks relevant to autistic-like behaviors. *Mental Retardation and Developmental Disabilities Research Reviews*, 10(4), 248-258. <https://doi.org/10.1002/mrdd.20039>
- Davis, J. M., Rowley, S. D., Braine, H. G., Plantadosi, S., & Santos, G. W. (1990). Clinical toxicity of cryopreserved bone marrow graft infusion. *Blood*, 75(3), 781-786.
- De la Torre, J., Kawanaga, H., Rowed, D., Johnson, C., Goode, D., Kajihara, K., & Mullan, S. (1975). Dimethyl sulfoxide in central nervous system trauma. *Annals of the New York Academy of Sciences*, 243(1), 362-389. <https://doi.org/10.1111/j.1749-6632.1975.tb25377.x>
- Dí Liberto, V., Mudó, G., Garozzo, R., Frinchi, M., Fernandez-Dueñas, V., Di Iorio, P., Ciccirelli, R., Caciagli, F., Condorelli, D. F., Ciruela, F., & Belluardo, N. (2016). The guanine-based purinergic system: The tale of an orphan neuromodulation. *Frontiers in Pharmacology*, 7, 158. <https://doi.org/10.3389/fphar.2016.00158>

- Downes, N., & Mullins, P. (2014). The development of myelin in the brain of the juvenile rat. *Toxicologic Pathology*, 42(5), 913–922. <https://doi.org/10.1177/0192623313503518>
- Dräger, U. C. (2006). Retinoic acid signaling in the functioning brain. *Science Signaling*, 2006(324), pe10. <https://doi.org/10.1126/stke.3242006pe10>
- Duester, G. (2008). Retinoic acid synthesis and signaling during early organogenesis. *Cell*, 134(6), 921–931. <https://doi.org/10.1016/j.cell.2008.09.002>
- Fontoura-Andrade, J. L., Amorim, R. F. B., & Sousa, J. B. (2017). Improving reproducibility and external validity. The role of standardization and data reporting of laboratory rat husbandry and housing. *Acta Cirurgica Brasileira*, 32(3), 251–262. <https://doi.org/10.1590/s0102-865020170030000010>
- Fossom, L., Messing, R., & Sparber, S. (1985). Long lasting behavioral effects of dimethyl sulfoxide and the "peripheral" toxicant p-bromophenylacetylurea. *Neurotoxicology*, 6(1), 17–28.
- Ha, S.-J., Kim, B.-G., Lee, Y.-A., Kim, Y.-H., Kim, B.-J., Jung, S.-E., Pang, M.-G., & Ryu, B.-Y. (2016). Effect of antioxidants and apoptosis inhibitors on cryopreservation of murine germ cells enriched for spermatogonial stem cells. *PLoS One*, 11(8), e0161372. <https://doi.org/10.1371/journal.pone.0161372>
- Hanslick, J. L., Lau, K., Noguchi, K. K., Olney, J. W., Zorumski, C. F., Mennerick, S., & Farber, N. B. (2009). Dimethyl sulfoxide (DMSO) produces widespread apoptosis in the developing central nervous system. *Neurobiology of Disease*, 34(1), 1–10. <https://doi.org/10.1016/j.nbd.2008.11.006>
- Ikedo, Y., & Long, D. M. (1990). Comparative effects of direct and indirect hydroxyl radical scavengers on traumatic brain oedema. *Acta neurochirurgica. Supplementum*, 51, 74–76. https://doi.org/10.1007/978-3-7091-9115-6_25
- Jang, Y., Park, J. J., Lee, M., Yoon, B., Yang, Y., Yang, S., & Kim, S. (2004). Retinoic acid-mediated induction of neurons and glial cells from human umbilical cord-derived hematopoietic stem cells. *Journal of Neuroscience Research*, 75(4), 573–584. <https://doi.org/10.1002/jnr.10789>
- Karaca, M., Bilgin, U., Akar, M., & de la Torre, J. (1991). Dimethyl sulphoxide lowers ICP after closed head trauma. *European Journal of Clinical Pharmacology*, 40(1), 113–114.
- Kedar, I., Jacob, E. T., Bar-Natan, N., & Ravid, M. (1983). Dimethyl sulfoxide in acute ischemia of the kidney. *Annals of the New York Academy of Sciences*, 411, 131–134. <https://doi.org/10.1111/j.1749-6632.1983.tb47294.x>
- Kenny, H. A., Lal-Nag, M., White, E. A., Shen, M., Chiang, C.-Y., Mitra, A. K., Zhang, Y., Curtis, M., Schryver, E. M., Bettis, S., Jadhav, A., Boxer, M. B., Li, Z., Ferrer, M., & Lengyel, E. (2015). Quantitative high throughput screening using a primary human three-dimensional organotypic culture predicts in vivo efficacy. *Nature Communications*, 6(1), 1–11. <https://doi.org/10.1038/ncomms7220>
- Kharasch, N., & Thyagarajan, B. (1983). Structural basis for biological activities of dimethyl sulfoxide. *Annals of the New York Academy of Sciences*, 411(1 Biological Ac), 391–402.
- Kim, E., Camacho, J., Combs, Z., Ariza, J., Lechpammer, M., Noctor, S. C., & Martínez-Cerdeño, V. (2015). Preliminary findings suggest the number and volume of supragranular and infragranular pyramidal neurons are similar in the anterior superior temporal area of control subjects and subjects with autism. *Neuroscience Letters*, 589, 98–103. <https://doi.org/10.1016/j.neulet.2015.01.021>
- Leake, C. D. (1966). Dimethyl sulfoxide. *Science*, 152, 1646–1649. <https://doi.org/10.1126/science.152.3729.1646>
- Lechpammer, M., Manning, S., Samonte, F., Nelligan, J., Sabo, E., Talos, D., Volpe, J. J., & Jensen, F. E. (2008). Minocycline treatment following hypoxic/ischaemic injury attenuates white matter injury in a rodent model of periventricular leucomalacia. *Neuropathology and Applied Neurobiology*, 34(4), 379–393. <https://doi.org/10.1111/j.1365-2990.2007.00925.x>
- Lechpammer, M., Tran, Y. P., Wintermark, P., Martínez-Cerdeño, V., Krishnan, V. V., Ahmed, W., Berman, R. F., Jensen, F. E., Nudler, E., & Zagzag, D. (2017). Upregulation of cystathionine β -synthase and p70S6K/S6 in neonatal hypoxic ischemic brain injury. *Brain Pathology*, 27(4), 449–458. <https://doi.org/10.1111/bpa.12421>
- Lechpammer, M., Wintermark, P., Merry, K. M., Jackson, M. C., Jantzie, L. L., & Jensen, F. E. (2016). Dysregulation of FMRP/mTOR signaling cascade in hypoxic-ischemic injury of premature human brain. *Journal of Child Neurology*, 31(4), 426–432. <https://doi.org/10.1177/0883073815596617>
- Liau, J., Hoang, S., Choi, M., Eroglu, C., Choi, M., Sun, G.-H., Percy, M., Wildman-Tobriner, B., Bliss, T., Guzman, R. G., Barres, B. A., & Steinberg, G. K. (2008). Thrombospondins 1 and 2 are necessary for synaptic plasticity and functional recovery after stroke. *Journal of Cerebral Blood Flow & Metabolism*, 28(10), 1722–1732. <https://doi.org/10.1038/jcbfm.2008.65>
- Little, J. R., Spetzler, R. F., Roski, R. A., Selman, W. R., Zabramski, J., & Lesser, R. P. (1983). Ineffectiveness of DMSO in treating experimental brain ischemia. *Annals of the New York Academy of Sciences*, 411, 269. <https://doi.org/10.1111/j.1749-6632.1983.tb47308.x>
- Liu, J., Yoshikawa, H., Nakajima, Y., & Tasaka, K. (2001). Involvement of mitochondrial permeability transition and caspase-9 activation in dimethyl sulfoxide-induced apoptosis of EL-4 lymphoma cells. *International Immunopharmacology*, 11(1), 63–74. [https://doi.org/10.1016/S1567-5769\(00\)00016-3](https://doi.org/10.1016/S1567-5769(00)00016-3)
- Martinez, M. (1992). Tissue levels of polyunsaturated fatty acids during early human development. *The Journal of Pediatrics*, 120(4), S129–S138. [https://doi.org/10.1016/S0022-3476\(05\)81247-8](https://doi.org/10.1016/S0022-3476(05)81247-8)
- Martin-Henao, G., Resano, P., Villegas, J., Manero, P., Sanchez, J., Bosch, M., Codins, A. E., Bruguera, M. S., Infante, L. R., Oyarzabal, A. P., Soldevila, R. N., Caiz, D. C., Bosch, L. M., Barbata, E. C., & Ronda, J. R. G. (2010). Adverse reactions during transfusion of thawed haematopoietic progenitor cells from apheresis are closely related to the number of granulocyte cells in the leukapheresis product. *Vox Sanguinis*, 99(3), 267–273. <https://doi.org/10.1111/j.1423-0410.2010.01341.x>
- Maryland, R. (1967). The status of dimethyl sulfoxide from the perspective of the food and drug administration John G. Harter. *Anti-inflammatory drug products*. Swmommen, 141, 1.
- Matyash, V., Liebisch, G., Kurzchalia, T. V., Shevchenko, A., & Schwudke, D. (2008). Lipid extraction by methyl-tert-butyl ether for high-throughput lipidomics. *Journal of Lipid Research*, 49(5), 1137–1146. <https://doi.org/10.1194/jlr.D700041-JLR200>
- Morris, C., De Weede, L., Scholten, M., Brand, R., Van Biezen, A., Sureda, A., Dickmeiss, E., Trnny, M., Apperley, J., Chiusolo, P., van Imhoff, G. W., Lenhoff, S., Martinelli, G., Hentrich, M., Pabst, T., Onida, F., Quinn, M. J., Kroger, N., de Witte, T., & Ruutu, T. (2014). Should the standard dimethyl sulfoxide concentration be reduced? Results of a European Group for Blood and Marrow Transplantation prospective noninterventional study on usage and side effects of dimethyl sulfoxide. *Transfusion*, 54(10), 2514–2522. <https://doi.org/10.1111/trf.12759>
- Moy, S., Nadler, J., Perez, A., Barbaro, R., Johns, J., Magnuson, T., Piven, J., & Crawley, J. N. (2004). Sociability and preference for social novelty in five inbred strains: An approach to assess autistic-like behavior in mice. *Genes, Brain and Behavior*, 3(5), 287–302. <https://doi.org/10.1111/j.1601-1848.2004.00076.x>
- Neumann, H., Kotter, M., & Franklin, R. (2009). Debris clearance by microglia: An essential link between degeneration and regeneration. *Brain*, 132(2), 288–295. <https://doi.org/10.1093/brain/awn109>
- Pearson, T. W., Dawson, H. J., & Lackey, H. B. (1981). Naturally occurring levels of dimethyl sulfoxide in selected fruits, vegetables, grains, and beverages. *Journal of Agricultural and Food Chemistry*, 29(5), 1089–1091. <https://doi.org/10.1021/jf00107a049>
- Ravid, M., Van-Dyk, D., Bernheim, J., & Kedar, I. (1983). The protective effect of dimethyl sulfoxide in experimental ischemia of the intestine.

- Annals of the New York Academy of Sciences*, 411, 100. <https://doi.org/10.1111/j.1749-6632.1983.tb47290.x>
- Rawls, J., Knecht, W., Diekert, K., Lill, R., & Löffler, M. (2000). Requirements for the mitochondrial import and localization of dihydroorotate dehydrogenase. *European Journal of Biochemistry*, 267(7), 2079–2087. <https://doi.org/10.1046/j.1432-1327.2000.01213.x>
- Rojo, A. I., McBean, G., Cindric, M., Egea, J., López, M. G., Rada, P., Zarkovic, N., & Cuadrado, A. (2014). Redox control of microglial function: Molecular mechanisms and functional significance. *Antioxidants & Redox Signaling*, 21(12), 1766–1801. <https://doi.org/10.1089/ars.2013.5745>
- Santos, N. C., Figueira-Coelho, J., Martins-Silva, J., & Saldanha, C. (2003). Multidisciplinary utilization of dimethyl sulfoxide: Pharmacological, cellular, and molecular aspects. *Biochemical Pharmacology*, 65(7), 1035–1041. [https://doi.org/10.1016/S0006-2952\(03\)00002-9](https://doi.org/10.1016/S0006-2952(03)00002-9)
- Schmitt, U., & Hiemke, C. (1998). Combination of open field and elevated plus-maze: A suitable test battery to assess strain as well as treatment differences in rat behavior. *Progress in Neuro-Psychopharmacology and Biological Psychiatry*, 22(7), 1197–1215. [https://doi.org/10.1016/S0278-5846\(98\)00051-7](https://doi.org/10.1016/S0278-5846(98)00051-7)
- Semple, B. D., Blomgren, K., Gimlin, K., Ferrero, D. M., & Noble-Haeusslein, L. J. (2013). Brain development in rodents and humans: Identifying benchmarks of maturation and vulnerability to injury across species. *Progress in Neurobiology*, 106, 1–16. <https://doi.org/10.1016/j.pneurobio.2013.04.001>
- Showalter, M. R., Cajka, T., & Fiehn, O. (2017). Epimetabolites: Discovering metabolism beyond building and burning. *Current Opinion in Chemical Biology*, 36, 70–76. <https://doi.org/10.1016/j.cbpa.2017.01.012>
- Showalter, M. R., Nonnecke, E. B., Linderholm, A., Cajka, T., Sa, M. R., Lönnerdal, B., Kenyon, N. J., & Fiehn, O. (2018). Obesogenic diets alter metabolism in mice. *PLoS One*, 13(1), e0190632. <https://doi.org/10.1371/journal.pone.0190632>
- Sonnenwald, U., Akiho, H., Koshiya, K., & Iwa, A. (1998). Effect of orotic acid on the metabolism of cerebral cortical astrocytes during hypoxia and reoxygenation: An NMR spectroscopy study. *Journal of Neuroscience Research*, 51(1), 103–108.
- Tsugawa, H., Cajka, T., Kind, T., Ma, Y., Higgins, B., Ikeda, K., Kanazawa, M., VanderGheynst, J., Fiehn, O., & Arita, M. (2015). MS-DIAL: Data-independent MS/MS deconvolution for comprehensive metabolome analysis. *Nature Methods*, 12(6), 523–526. <https://doi.org/10.1038/nmeth.3393>
- Tunçer, S., Gurbanov, R., Sheraj, I., Sofel, E., Esenturk, O., & Banerjee, S. (2018). Low dose dimethyl sulfoxide driven gross molecular changes have the potential to interfere with various cellular processes. *Scientific Reports*, 8(1), 1–15. <https://doi.org/10.1038/s41598-018-33234-z>
- Turner, P. V., Brabb, T., Pekow, C., & Vasbinder, M. A. (2011). Administration of substances to laboratory animals: Routes of administration and factors to consider. *Journal of the American Association for Laboratory Animal Science*, 50(5), 600–613.
- Verheijen, M., Lienhard, M., Schrooders, Y., Clayton, O., Nudischer, R., Boerno, S., Timmermann, B., Selevsek, N., Schlapbach, R., Gmuender, H., Gotta, S., Geraedts, J., Herwig, R., Kleinjans, J., & Caiment, F. (2019). DMSO induces drastic changes in human cellular processes and epigenetic landscape in vitro. *Scientific Reports*, 9(1), 1–12. <https://doi.org/10.1038/s41598-019-40660-0>
- Wagner, E., Luo, T., & Dräger, U. C. (2002). Retinoic acid synthesis in the postnatal mouse brain marks distinct developmental stages and functional systems. *Cerebral Cortex*, 12(12), 1244–1253. <https://doi.org/10.1093/cercor/12.12.1244>
- Willhite, C., & Katz, P. (1984). Dimethyl sulfoxide. *Journal of Applied Toxicology*, 4(3), 155–160. <https://doi.org/10.1002/jat.2550040308>
- Wong, L. K., & Reinertson, E. L. (1984). Clinical considerations of dimethyl sulfoxide. *Iowa State University Veterinarian*, 46(2), 2.
- Yellowlees, P., Greenfield, C., & McIntyre, N. (1980). Dimethylsulphoxide-induced toxicity. *The Lancet*, 316(8202), 1004–1006. [https://doi.org/10.1016/S0140-6736\(80\)92158-3](https://doi.org/10.1016/S0140-6736(80)92158-3)
- Yi, X.-Y., Gauthier, K. M., Cui, L., Nithipatikom, K., Falck, J. R., & Campbell, W. B. (2007). Metabolism of adrenic acid to vasodilatory 1 α , 3 β -dihomo-epoxyelcosatrienoic acids by bovine coronary arteries. *American Journal of Physiology-Heart and Circulatory Physiology*, 292(5), H2265–H2274. <https://doi.org/10.1152/ajpheart.00947.2006>
- Yuan, Y., Yang, Y., Tian, Y., Park, J., Dai, A., Roberts, R. M., Liu, Y., & Han, X. (2016). Efficient long-term cryopreservation of pluripotent stem cells at -80 C. *Sci Rep-Uk*, 6(1), 1–13.
- Zhao, B. S., & He, C. (2015). Pseudouridine in a new era of RNA modifications. *Cell Research*, 25(2), 153–154. <https://doi.org/10.1038/cr.2014.143>

SUPPORTING INFORMATION

Additional supporting information may be found online in the Supporting Information section.

How to cite this article: Rabow Z, Morningstar T, Showalter M, et al. Exposure to DMSO during infancy alters neurochemistry, social interactions, and brain morphology in long-evans rats. *Brain Behav*. 2021;11:e02146. <https://doi.org/10.1002/brb3.2146>

Exposure to DMSO in infancy alters neurochemistry, social interactions, and brain morphology in Long-Evans Rats

Supplemental figures

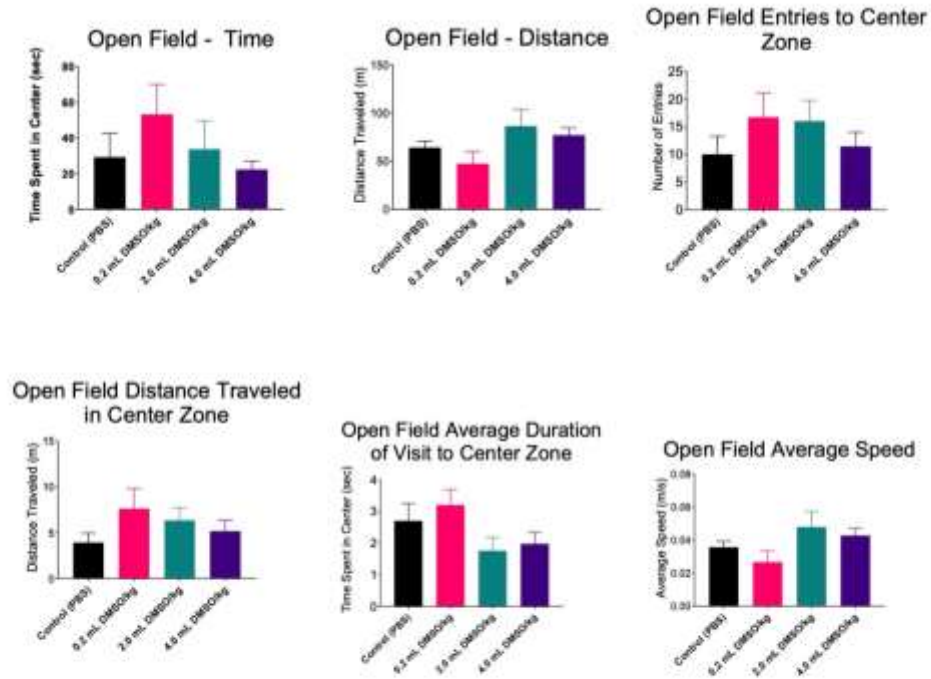
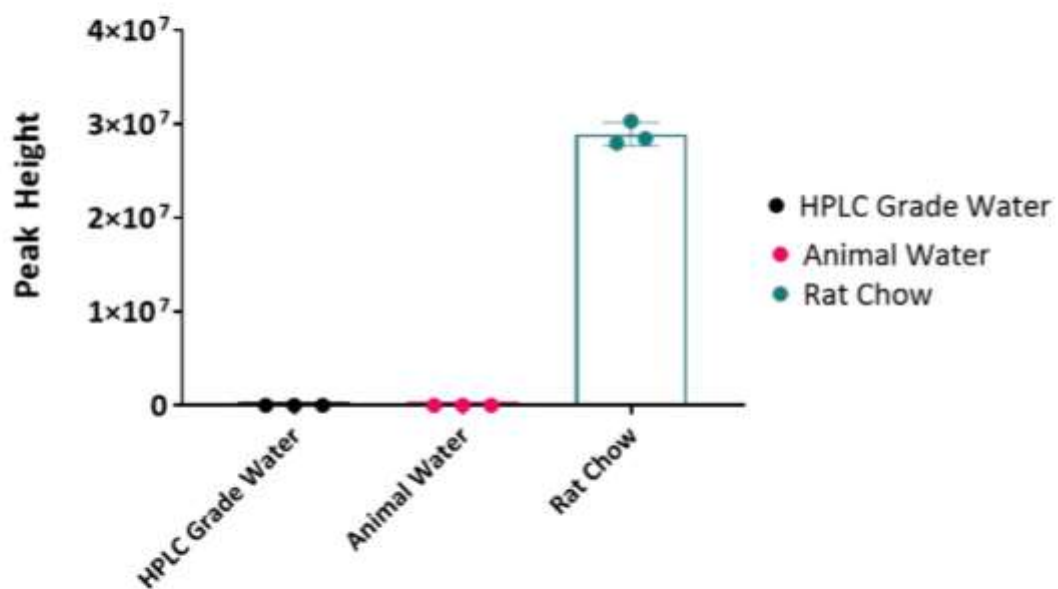


Figure S1 – Locomotion assessment of LE Rats at P21 (n= 28). Experimental groups were prepared and submitted to behavioral assessments as described in the methods. No changes were observed.

(A) Analysis of DMSO in Rat Chow and Water



(B) Calibration Curve

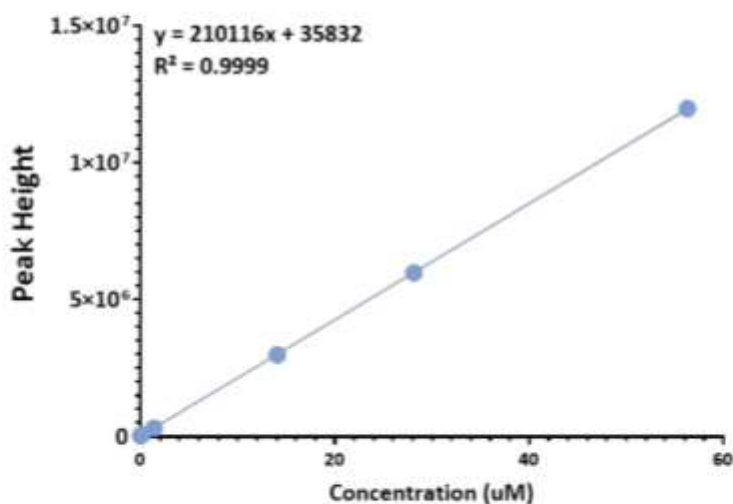


Figure S2- Analytical precision of DMSO Detection and quantification (A) Analysis an analytical blank (HPLC grade water), animal water and food ($n=3/\text{group}$). (B) DMSO Calibration Curve showing excellent linearity with limit of quantificaion above 0.01 μM .

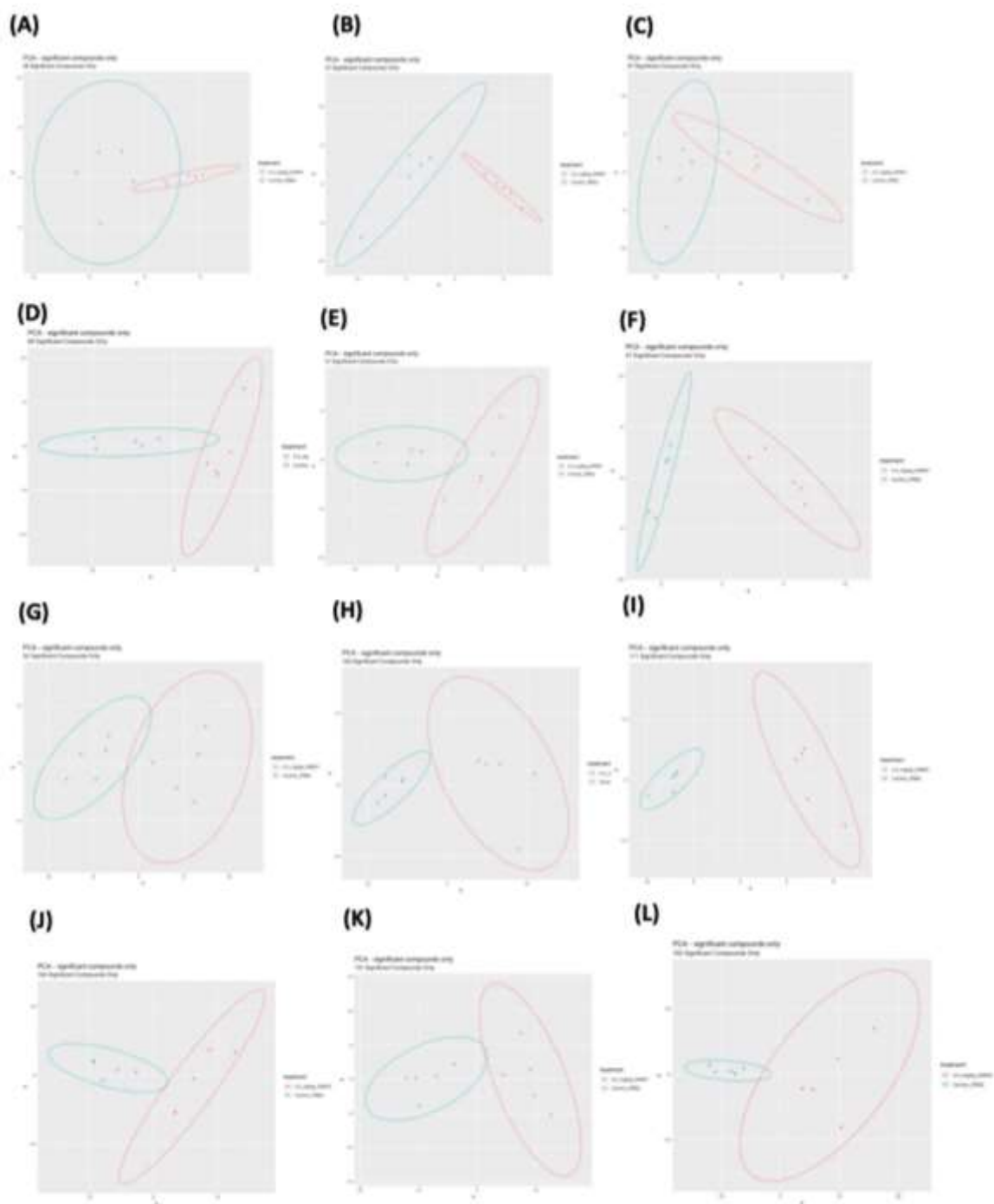


Figure S3 PCA plots of significant metabolites compared to sham-treated control (n= 20 total, 5 per group). A) Cortex 0.2 mL DMSO/kg vs sham-treated control B) Cortex 2.0 mL DMSO/kg vs sham-treated control C) Cortex 4.0 mL DMSO/kg vs sham-treated control D) Hippocampus 0.2 mL DMSO/kg vs sham-treated control E) Hippocampus 2.0 mL DMSO/kg vs sham-treated control F) Hippocampus 4.0 mL DMSO/kg vs sham-treated control G) Basal ganglia 0.2 mL DMSO/kg vs sham-treated control H) Basal ganglia 2.0 mL DMSO/kg vs sham-treated control I) Basal ganglia 4.0 mL DMSO/kg vs sham-treated control J) Cerebellum 0.2 mL DMSO/kg vs sham-treated control K) Cerebellum 2.0 mL DMSO/kg vs sham-treated control L) Cerebellum 4.0 mL DMSO/kg vs sham-treated control

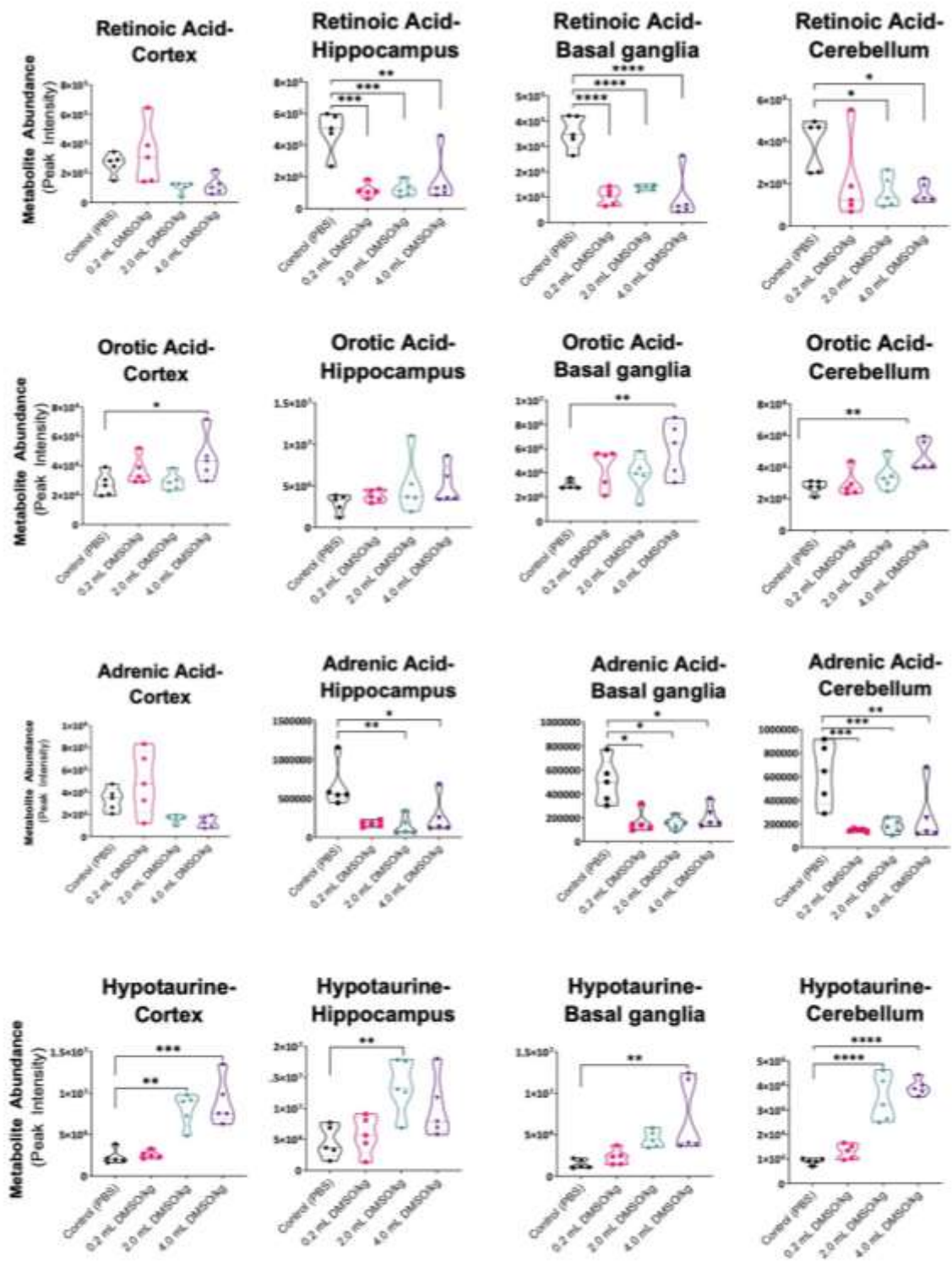


Figure S3 Violin plots of selected metabolites (n= 20 total, 5 per group)*p < 0.05 versus control (PBS); **p < 0.01 versus control (PBS); ***p < 0.001 versus control (PBS); ****p < 0.0001 versus control (PBS)

p73 α 1, an Isoform of the p73 Tumor Suppressor, Modulates Lipid Metabolism and Cancer Cell Growth via Stearoyl-CoA Desaturase-1

Zachary Rabow^{1,†}, Kyra Laubach^{2,†}, Xiangmudong Kong², Tong Shen¹, Shakur Mohibi², Jin Zhang^{2,*}, Oliver Fiehn^{1,*} and Xinbin Chen^{2,*}

¹ West Coast Metabolomics Center, University of California, Davis, CA 95616, USA

² Comparative Oncology Laboratory, Schools of Medicine and Veterinary Medicine, University of California, Davis, CA 95616, USA

* Correspondence: jinzhang@ucdavis.edu (J.Z.); ofiehn@ucdavis.edu (O.F.); xbchen@ucdavis.edu (X.C.); Tel.: +1-530-752-8725 (J.Z.); +1-530-754-8258 (O.F.); +1-530-754-8404 (X.C.)

† These authors contributed equally to this work.

Abstract: Altered lipid metabolism is a hallmark of cancer. p73, a p53 family member, regulates cellular processes and is expressed as multiple isoforms. However, the role of p73 in regulating lipid metabolism is not well-characterized. Previously, we found that loss of p73 exon 12 (*E12*) leads to an isoform switch from p73 α to p73 α 1, the latter of which has strong tumor suppressive activity. In this study, comprehensive untargeted metabolomics was performed to determine whether p73 α 1 alters lipid metabolism in non-small cell lung carcinoma cells. RNA-seq and molecular biology approaches were combined to identify lipid metabolism genes altered upon loss of *E12* and identify a direct target of p73 α 1. We found that loss of *E12* leads to decreased levels of phosphatidylcholines, and this was due to decreased expression of genes involved in phosphatidylcholine synthesis. Additionally, we found that *E12*-knockout cells had increased levels of phosphatidylcholines containing saturated fatty acids (FAs) and decreased levels of phosphatidylcholines containing monounsaturated fatty acids (MUFAs). We then found that p73 α 1 inhibits cancer cell viability through direct transcriptional suppression of Stearoyl-CoA Desaturase-1 (*SCD1*), which converts saturated FAs to MUFAs. Finally, we showed that p73 α 1-mediated suppression of *SCD1* leads to increased ratios of saturated FAs to MUFAs.

Keywords: p73 isoforms; the p53 family; Stearoyl-CoA Desaturase; lipid metabolism; Kennedy pathway

1. Introduction

Lipids are key building blocks in cells that are essential for membrane formation, energy storage, and cell signaling. In particular, glycerophospholipids are the primary component of cell membranes and are composed of a phosphate head group attached to a diacylglycerol (DG) backbone and two fatty acids (FAs) [1]. There are multiple classes of glycerophospholipids, but phosphatidylcholines (PCs) are the most abundant class within eukaryotic cell membranes, contributing up to 50% of the total phospholipid content [2]. PC biosynthesis occurs through the Kennedy pathway (consisting of the CDP-choline and CDP-ethanolamine branches), the Lands Cycle, or the phosphatidylethanolamine methyltransferase (PEMT) pathway [3–5]. The Kennedy pathway is initiated by intracellular choline import via choline transporters (CTLs and CHTs), where choline is quickly converted to phosphocholine (P-choline) by choline kinases in the cytosol [6]. P-choline is then converted to CDP-choline by CDP-choline synthetase in the nucleus or cytosol. Finally, the choline head group is linked to a DG backbone by choline/ethanolamine phosphotransferase to form PCs [3]. In the Lands Cycle, phospholipases cleave PCs to form lysophosphatidylcholines (LPCs) and FAs [7]. LPCs can then be converted back to PCs through lysophospholipid acyltransferases. The PEMT pathway, occurring in the liver, methylates

phosphatidylethanolamines (PEs), through the methyl donor S-adenosylmethionine, to form PCs [8]. Various PC metabolites exist due to differences in fatty acyl chain length and saturation [9].

Traditionally thought of as membrane lipids, the role of PCs in energy metabolism, cell signaling, and lipoprotein transport is becoming more apparent [10].

Altered lipid metabolism has become a consequential hallmark of tumorigenesis [11]. Carcinogenic cells can increase lipid synthesis and/or uptake to sustain their rapidly dividing state [12]. Evidence shows that increased levels of PCs and other choline-containing metabolites are associated with oncogenesis [13]. Cancer cells maintain high levels of PC synthesis through increased choline import and the formation of PC intermediates [14–16]. An abundance of PCs and choline-containing metabolites confers cancer cell survival in metabolically demanding conditions [17]. PCs can also be modified to form signaling lipids, such as arachidonic acid, phosphatidic acid, and DGs. These signaling lipids activate a myriad of oncogenic pathways to promote tumorigenesis [18,19]. For example, phosphatidic acid activates the mTOR pathway to inhibit apoptosis and promote cancer cell survival [20]. Similarly, arachidonic acid and its derivatives have been shown to promote angiogenesis, and tumor cell proliferation and invasion [21]. As such, altered PC metabolism is undoubtedly critical for driving tumorigenesis.

p73, a member of the p53 family of tumor suppressors, is a transcription factor and regulates many cellular processes [22,23]. The p73 gene structure affords the formation of multiple isoforms with varying functions. The N-terminal isoforms arise from two promoters, denoted P1 and P2, located upstream of exon 1 and in intron 3, respectively [24]. Transcription initiation from the P1 promoter leads to the expression of TAp73 isoforms [24], which have a tumor suppressive function similar to that of p53 [25–28]. Conversely, the P2 promoter produces $\Delta Np73$ isoforms [29] that promote cell survival and can function as oncoproteins [30–32]. At the 3' end, alternative splicing of exons 11, 12 and 13 gives rise to several known C-terminal isoforms [29,33,34]. p73 α is the major isoform expressed in most human and mouse tissues and the most well-studied [35,36]. Previously, we found that exclusion of exon 12 (*E12*) leads to an isoform switch from p73 α to a novel isoform that we termed p73 α 1 [37]. We found that p73 α 1 was endogenously expressed in multiple cancer cell lines, as well as normal and cancerous human prostate tissues [37]. Additionally, we found that p73 α 1 inhibits cancer cell viability in vitro, and mice deficient in *E12* are not prone to spontaneous tumors [37]. To further investigate the biological function of p73 α 1, we wanted to explore whether p73 α 1 regulates lipid metabolism.

In the present study, we investigated the effect of p73 α 1 expression on the lipidome in non-small cell lung carcinoma (H1299) cells, which do not express p53. We found that loss of *E12* leads to decreased levels of PCs, PEs, and their derivatives. RNA-seq analysis showed that *E12*-knockout (*E12*-KO) cells had decreased expression of several enzymes involved in PC and PE synthesis, but choline import appeared unchanged. Furthermore, we found that loss of *E12* led to increased levels of PCs containing saturated FAs and decreased levels of PCs containing mono-unsaturated FAs (MUFAs). We then discovered that p73 α 1 directly inhibits Stearoyl-CoA Desaturase-1 (*SCD1*) expression, which converts saturated FAs to MUFAs. Finally, we found that p73 α 1-mediated suppression of *SCD1* inhibits cancer cell viability and leads to an increased ratio of saturated FAs to MUFAs.

2. Materials and Methods

2.1. Cell Culture and Cell Line Generation

H1299 cells (non-small cell lung carcinoma, ATCC; Manassas, VA, USA; Cat# CRL-5803) were cultured in DMEM (Gibco; Waltham, MA, USA; Cat# 12100-61) supplemented with 10% FBS (Gibco; Waltham, MA, USA; Cat# A4766801) and Antibiotic-Antimycotic solution (Gibco; Waltham, MA, USA; Cat# 15240-062). H1299 cell lines tested negative for mycoplasma and were used at passage 20 or lower. *E12*^{-/-} H1299 cell lines were generated as described previously [37].

2.2. Plasmid Generation

pSpCas9(BB)-2A-Puro expression vector was generated by the Zhang Lab [38] and purchased from Addgene (Watertown, MA, USA; Cat# 48139). A vector expressing a single guide RNA (sgRNA) that targeted *E12* was generated by annealing two 25-nt oligos and cloning the product into the pSpCas9(BB)-2A-Puro expression vector via BbsI. All primer sequences used to generate the corresponding expression vectors were listed in Table S1.

2.3. RNA Isolation and qPCR

Quick-RNA MiniPrep Kit (Zymo Research; Irvine, CA, USA; Cat# 11-327) was used to isolate RNA according to the manufacturer's protocol. RNA was then used for cDNA synthesis using oligo dT (18) primer (Thermo Scientific; Waltham, MA, USA; Cat# FERSO123), random hexamer primer (Thermo Scientific; Waltham, MA, USA; Cat# SO142), dNTP (Cat# FERR0181), RiboLock RNase Inhibitor (Thermo Scientific; Waltham, MA, USA; Cat# EO0381), and RevertAid Reverse Transcriptase (Thermo Scientific; Waltham, MA, USA; Cat# EP0441) according to the manufacturer's protocol. The cDNA was used for qPCR with PowerUp Sybr Green Master Mix (Applied Biosystems, Waltham, MA, USA; Cat# A25742) according to the manufacturer's protocol. All primers used for qPCR were listed in Table S2.

2.4. Western Blot Analysis

Western blot analysis was performed as previously described [39]. Briefly, whole cell lysates were harvested with 1× SDS lysis buffer [62.5 mM Tris-HCl pH 6.5, 10% glycerol (Sigma; St. Louis, MO, USA; Cat# G5516-4L), 2% SDS, 0.71 M 2-mercaptoethanol (Acros Organics; Waltham, MA, USA; Cat# 125470010), and 0.15 mM bromophenol blue (Fisher Bioreagents; Waltham, MA, USA; Cat# BP115-25)] and boiled at 95 °C for 6 min. Proteins were separated on polyacrylamide gel [10% acrylamide/bis-acrylamide (Sigma; St. Louis, MO, USA; Cat# A3574-5L), 0.37 M Tris-HCl pH 8.8, 0.035% ammonium persulfate (VWR; Radnor, PA, USA; Cat# 0486-100G), and 4.6 M TEMED (Acros Organics; Waltham, MA, USA; Cat# 138455000)], then transferred to 0.45 mM nitrocellulose membrane (Cytiva; Marlborough, MA, USA; Cat# 10600002). Membranes were probed overnight at 4 °C with the indicated primary antibodies: anti-CD92 (Santa Cruz Biotechnology; Dallas, TX, USA; Cat# 517098), anti-GAPDH (Cell Signaling Technology; Danvers, MA, USA; Cat# 14C10), anti-Vinculin (Cell Signaling Technology; Danvers, MA, USA; Cat# E1E9V), anti-CCTa (Cell Signaling Technology; Danvers, MA, USA; Cat# 69315), anti-SMPD4 (Novus Biologicals; Littleton, CO, USA; Cat# NBP2-93253), anti-CEPT1 (Invitrogen; Waltham, MA, USA; Cat# PA5-23876) anti-SCD1 (Abcam; Cambridge, United Kingdom; Cat# ab236868). Membranes were then incubated at room temperature for 3 h with either anti-mouse (Bio Rad; Hercules, CA, USA; Cat# 1705047) or anti-rabbit (Bio Rad; Hercules, CA, USA; Cat# 1705046) HRP conjugated secondary antibodies. The proteins were visualized with WesternBright ECL HRP substrate (Advansta; San Jose, CA, USA; Cat# K-12043-D20). VisionWorks[®]LS software was used to analyze the images.

2.5. ChIP Assay

ChIP assay was performed as previously described [40]. Briefly, chromatin was cross-linked with 1% formaldehyde in phosphate-buffered saline (PBS) and added directly to the media. Cells were lysed in 2× modified RIPA buffer [0.1 M Tris-HCl, 2% NP-40 (USB; Waltham, MA, USA; Cat# 19628), 0.5% deoxycholic acid (Fisher Bioreagents; Waltham, MA, USA; Cat# BP349-100), 2 mM EDTA (Fisher Bioreagents; Waltham, MA, USA; Cat# BP120-1) with protease inhibitor cocktail (Thermo Scientific; Waltham, MA, USA; Cat# 78438). Chromatin lysates were sonicated to yield ~200–1000 base pair DNA fragments and immunoprecipitated with 1 mg of control anti-IgG normal rabbit (EMD Millipore; Burlington, MA, USA; Cat# NI01-100 mg) or anti-TAp73 (Bethyl Laboratories; Waltham, MA, USA; Cat# A300-126A) and captured with protein A/G magnetic agarose beads (Thermo Scientific; Waltham, MA, USA; Cat# 78609) at 4 °C overnight. The DNA-protein

immunocomplexes were reverse cross-linked and purified using ChIP DNA Clean and Concentrator (Zymo Research; Irvine, CA, USA; Cat# 50-44-363). The DNA fragments were amplified with PCR using DreamTaq DNA polymerase (Thermo Scientific; Waltham, MA, USA; Cat# FEREP0713). The PCR program used for amplification was (1) 94 °C for 5 min, (2) 94 °C for 30 s, (3) 60 °C for 30 s, (4) 72 °C for 30 s, and (5) 72 °C for 10 min. Steps 2–4 were repeated for 32 cycles to amplify *GAPDH*, 36 cycles to amplify *SCD1*, or 38 cycles to amplify *CDKN1A*. Primers used for ChIP assay were listed in Table S2.

2.6. siRNA Knockdown

siRNA was purchased from Horizon Discovery Biosciences and resuspended in 5× siRNA Buffer (Thermo Scientific; Waltham, MA, USA; Cat# B-002000-UB-100) to a final concentration of 20 mM. 2×10^5 cells were plated in a 6-well plate. After 24 h, cells were transfected using RNAi Max (Invitrogen; Waltham, MA, USA; Cat# 13778150) according to the manufacturer's protocol with the appropriate siRNA at the indicated concentrations: scrambled siRNA (Scr) (5'-GGC CGA UUG UCA AAU AAU U-3') (90 nM), si-p73 α 1 (5'-ACC UGG GGC CCG UGG UUU-3') (70 nM), or si-SCD1 (5'-GAG AUA AGU UGG AGA CGA UdTdT-3') (20 nM). After 48 h, cells were trypsinized (VWR; Radnor, PA, USA; Cat# 0458-250G) and either seeded for RNA or protein collection, or for cell viability assay.

2.7. Cell Viability Assay

5×10^3 cells were plated in a 96-well plate. After 96 h, cell viability was measured using CellTiter-Glo 2.0 Cell Viability Assay kit (Promega; Madison, WI, USA; Cat# G9241) according to the manufacturer's protocol. The assay was performed in triplicates to ensure proper statistical analyses.

2.8. Metabolomics and Lipidomics

Lipidomics and metabolomics analysis was performed at the UC Davis West Coast Metabolomics Center. Three million cells were collected into 2 mL Eppendorf tubes (Eppendorf; Hamburg, Germany; Cat# 4036-3352). Samples were randomized and extracted alongside one method blank and one bioreclamation sample per every 10 biological samples. Samples were extracted using the modified Matyash Extraction [41]. 225 μ L of ice-cold methanol, with Avanti SPLASHone internal standards (Avanti Polar Lipids; Alabaster, AL, USA; Cat# 330707) was added to each sample. Cells were homogenized for 90 s in methanol with 2 mm stainless steel beads using an SPEX Geno/Grinder (SPEX SamplePrep; Metuchen, NJ, USA). 750 μ L MTBE was added to the samples, vortex briefly, and then mixed on an orbital shaker for 5 min at 4 °C. Next, 188 μ L water was added to the tubes, vortexed, and then centrifuged for 3 min at 16k RPM. The top organic layer was collected (two, 180 μ L fractions) for lipidomics analysis, and the bottom polar fraction (two, 150 μ L fractions) was collected for metabolomics. All fractions were dried under vacuum using a rotovap. Lipidomics analysis was performed by resuspending dried fractions in 100 μ L Methanol: Toluene (9:1) and analyzed using liquid chromatography (LC) high-resolution mass spectrometry (Q Exactive HF MS/MS). LC conditions were carried out using a Vanquish Focused UHPLC, Waters Acquity UPLC CSH C18 columns (100 mm \times 2.1 mm, 1.7 μ m particle size) with mobile phase A consisting of 6:4 acetonitrile: water and mobile phase B consisting of 9:1 isopropanol: water, both containing 10 mM ammonium formate and 0.1% formic acid for positive ionization mode, and 10 mM ammonium formate for negative ionization mode analysis. 3 and 5 μ Ls of pooled samples were injected for positive and negative modes to equilibrate the column prior to analysis. Mobile phase gradient and mass spectrometry parameters were identical, as described previously [42]. Metabolomics was performed by GC-MS as previously described [43] and by high-resolution LC-MS/MS as described previously [44].

2.9. Statistical Analysis

Data are presented as mean \pm SEM. Significant difference between two groups was assessed by one-tailed, unpaired Student's *t*-test and comparisons between two or more groups were assessed by one-way ANOVA with Benjamini and Hochberg FDR post-test for multiple comparisons, when appropriate. Statistical analysis was performed with GraphPad Prism 9. Statistical parameters can be found in the figure legends. ChemRICH analysis was performed as previously described [45].

3. Results

3.1. Isoform Switch from *p73 α* to *p73 α 1* Alters the Metabolome in H1299 Cells

To determine the role of *p73 α 1* in regulating lipid metabolism, untargeted metabolomic and lipidomic analyses were performed in isogenic control and E12-KO clone #1 (*E12^{-/-}* #1) H1299 cell lines (Figure 1A). It is important to note that isogenic control cells express mostly *p73 α* and a small amount of *p73 α 1*, and E12-KO cells express *p73 α 1* and no *p73 α* (Figure S1A) [37]. 734 lipids and 163 primary metabolites were identified through LC-MS/MS and GC-MS analysis, respectively. Triacylglycerols (TGs), PCs, ether-linked PCs, and PEs were among the classes with the highest lipid counts, and carbohydrates, amino acids, and peptides had the highest primary metabolite counts (Figure 1B). Principal Component Analysis showed the cell lines scattered in the first two principal components, with tight clustering of the pooled quality control samples, indicating excellent analytical precision. The first principal component explains 51% of the total observed biological variance, with the second principal component accounting for nearly 34% of the variance (Figure 1C). Total lipid content was found to be significantly lower in E12-KO cells compared to isogenic control cells (Figure S1B). Consistent with this, the volcano plot displayed a general trend of metabolites and lipids being downregulated in E12-KO cells compared to isogenic control cells (Figure 1D).

To identify class-level lipid changes associated with loss of *E12*, a chemical similarity enrichment analysis (ChemRICH) plot was generated. Using general class-level classifications, the analysis showed that PCs and TGs were the two most significantly altered classes; PCs were decreased, but TGs were increased in E12-KO cells, with a slightly mixed effect for both. The mixed effect for PCs indicated that many of these lipids were decreased in E12-KO cells, while some were increased, compared to isogenic control cells. Conversely, the mixed effect in TGs indicated that most TG lipids were increased in E12-KO cells, while some were decreased, compared to isogenic control cells (Figure 1E). To expand on the broad class-level analysis, a heat map detailing all annotated lipids was generated (Figure 1F). Loss of *E12* led to a considerable decrease in overall FAs compared to isogenic control cells (Figure 1F). Additionally, E12-KO cells exhibited decreased levels of PCs, LPCs, and PEs compared to isogenic control cells (Figure 1F). On the other hand, E12-KO cells elicited a substantial increase in TGs compared to isogenic control cells (Figure 1F). Carnitines and bis(monoacylglycerol)phosphates were significantly decreased in E12-KO cells compared to isogenic control cells, while ether-linked TGs exhibited the opposite trend (Figure S1C). Phosphatidylglycerols, cardiolipins, sphingomyelins, ceramides, and cholesterol esters were not altered between isogenic control and E12-KO cells (Figure S1D).

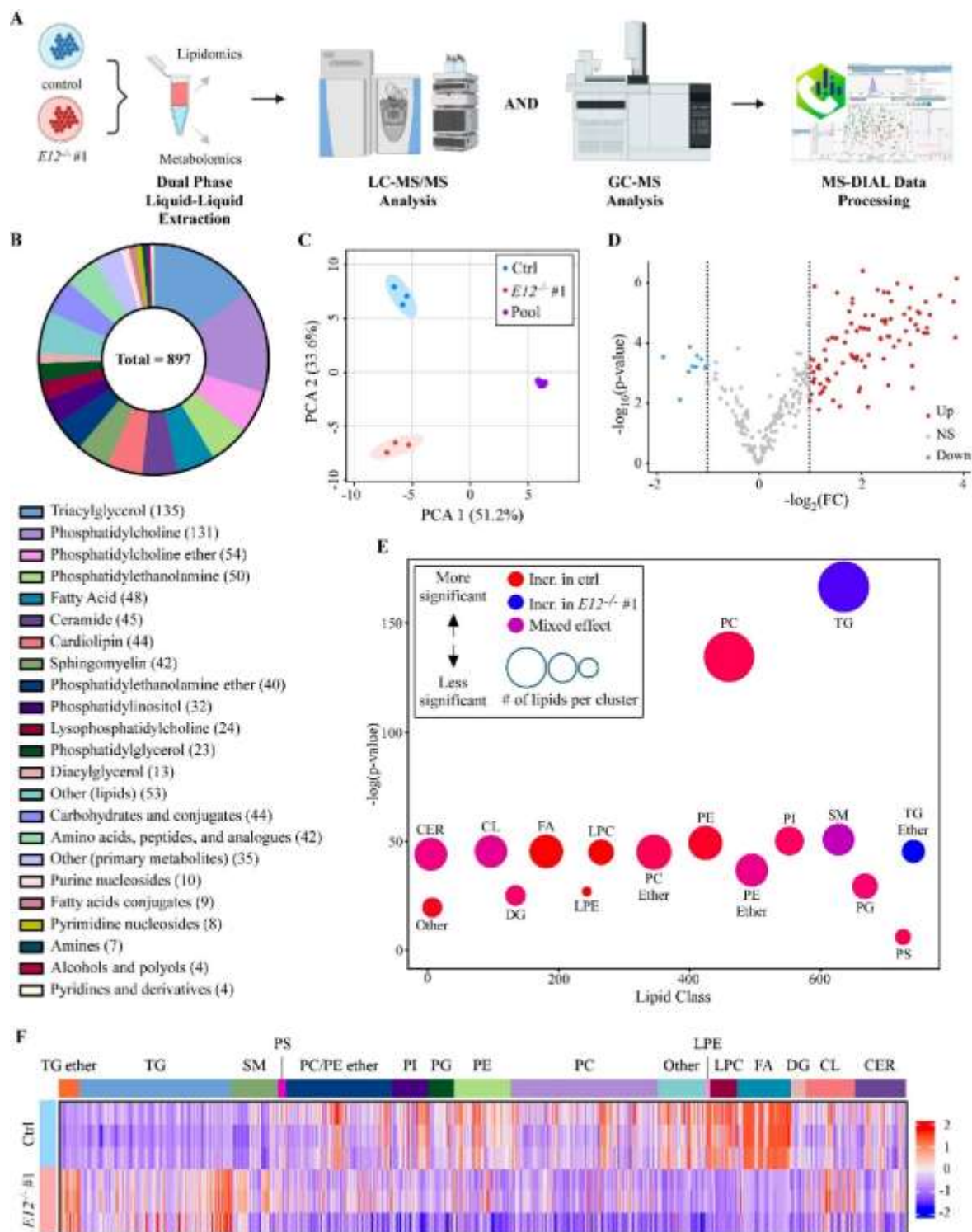


Figure 1. Lipidome overview in isogenic control and E12-KO H1299 cells. (A). Schematic of lipidomic and metabolomic analysis workflow in isogenic control and $E12^{-/-}$ H1299 cells. (B). Class-level overview of metabolites annotated by LC-MS/MS and GC-MS analysis in isogenic control and $E12^{-/-}$ H1299 cells. 897 individual metabolites were identified using accurate mass and in-silico libraries (top). Number of metabolites in each class are indicated in the parentheses (bottom). Classes with less than 10 identified lipids or metabolites were grouped together and denoted "Other (lipids)"

or "Other (primary metabolites)". (C). Principal component analysis (PCA) of isogenic control, $E12^{-/-}$ H1299 cells and pooled quality control samples. (D). Volcano plot of isogenic control compared to $E12^{-/-}$ H1299 cells. Up indicates lipids and metabolites higher in isogenic control cells. (E). Chemical similar enrichment analysis (ChemRICH) of all lipids identified in isogenic control and $E12^{-/-}$ H1299 cells. Y-axis represents statistical significance assessed by Kolmogorov-Smirnov test and node size represents total number of lipids per cluster. Classes with less than 10 identified lipids were grouped together and denoted "Other". TG: triacylglycerols; PC: phosphatidylcholines; CER: ceramides; CL: cardiolipins; FA: fatty acids; DG: diacylglycerols; LPE: lysophosphatidylethanolamines; LPC: lysophosphatidylcholines; PE: phosphatidylethanolamines; PI: phosphatidylinositols; PG: phosphatidylglycerols; PS: phosphatidylserines; SM: sphingomyelins. (F). Heatmap of all annotated lipids clustered by class in isogenic control and $E12^{-/-}$ H1299 cells. Color intensity indicates z-score values of peak heights. CER: ceramides; CL: cardiolipins; DG: diacylglycerols; FA: fatty acids; LPC: lysophosphatidylcholines; LPE: lysophosphatidylethanolamines; PC: phosphatidylcholines; PE: phosphatidylethanolamines; PG: phosphatidylglycerols; PI: phosphatidylinositols; PS: phosphatidylserines; SM: sphingomyelins; TG: triacylglycerols.

3.2. Loss of *E12* Leads to Specific Lipidome Changes in H1299 Cells

Lipidome changes between isogenic control and *E12*-KO cells were further investigated. The top six upregulated (Figure 2A) and downregulated (Figure 2B) compounds were analyzed to determine whether specific lipid classes or pathways were affected by the loss of *E12*. The top six downregulated metabolites were all FAs; three MUFAs (FA 18:1, FA 20:1, FA 26:1) all with fold changes of 0.10, two saturated FAs (FA 16:0, FA 24:0) with fold changes of 0.20 and 0.25, and one poly-unsaturated FA (PUFA) (FA 24:4) with a fold change of 0.14 (Figure 2A). TG species made up four of the top six upregulated metabolites, consisting of three ether-linked TGs (TG-O 48:2, TG-O 54:1, TG-O 46:0) with fold changes of 5, 5 and 10, respectively, and TG 42:0, with a fold change of 10 (Figure 2B). Two polar metabolites, glycerol 3-phosphate and inosine-5-monophosphate with fold changes of 14 and 10, were the other most upregulated metabolites. We hypothesized that the accumulation of glycerol 3-phosphate in *E12*-KO cells was a result of decreased glycerophospholipid levels, as shown in Figure 1F. Overall, these data indicate that loss of *E12* alters the abundance of certain lipid classes and precursors.

To better understand lipid metabolism alterations in *E12*-KO cells, the general class-level ChemRICH plot (Figure 1E) was delineated by saturation level (Figure 2C,D). Interestingly, the mixed effect seen in PCs and TGs in Figure 1E was not observed when the broad classes were stratified by saturation status. PCs containing PUFAs were significantly dysregulated ($FDR = 3.4 \times 10^{45}$), where 70% of all PCs containing PUFAs were altered (67 downregulated and 8 upregulated in *E12*-KO cells) (Figure 2D). On the other hand, PCs containing MUFAs had a slightly mixed effect, with 9 out of 13 being lower in *E12*-KO cells, and four out of 13 being higher in the *E12*-KO cells (Figure 2D). Interestingly, PCs containing saturated FAs were significantly upregulated ($FDR = 2.5 \times 10^8$) in *E12*-KO cells, with 90% being increased in *E12*-KO cells (Figure 2C,D). Overall, TGs of all saturation levels were increased in *E12*-KO cells compared to isogenic control cells (Figure 2C). All TG species containing saturated FAs and MUFAs were increased in *E12*-KO cells (Figure 2D). While over 90% of TGs containing di-unsaturated fatty acids (DUFAs) and PUFAs were increased in *E12*-KO cells, there were 4 individual species that were decreased in *E12*-KO cells (Figure 2D). Similar trends were seen for other lipid classes; however, several classes—ceramides, cardiolipins, sphingomyelins, and ether-linked PEs—showed a mixed effect (Figure 2D).

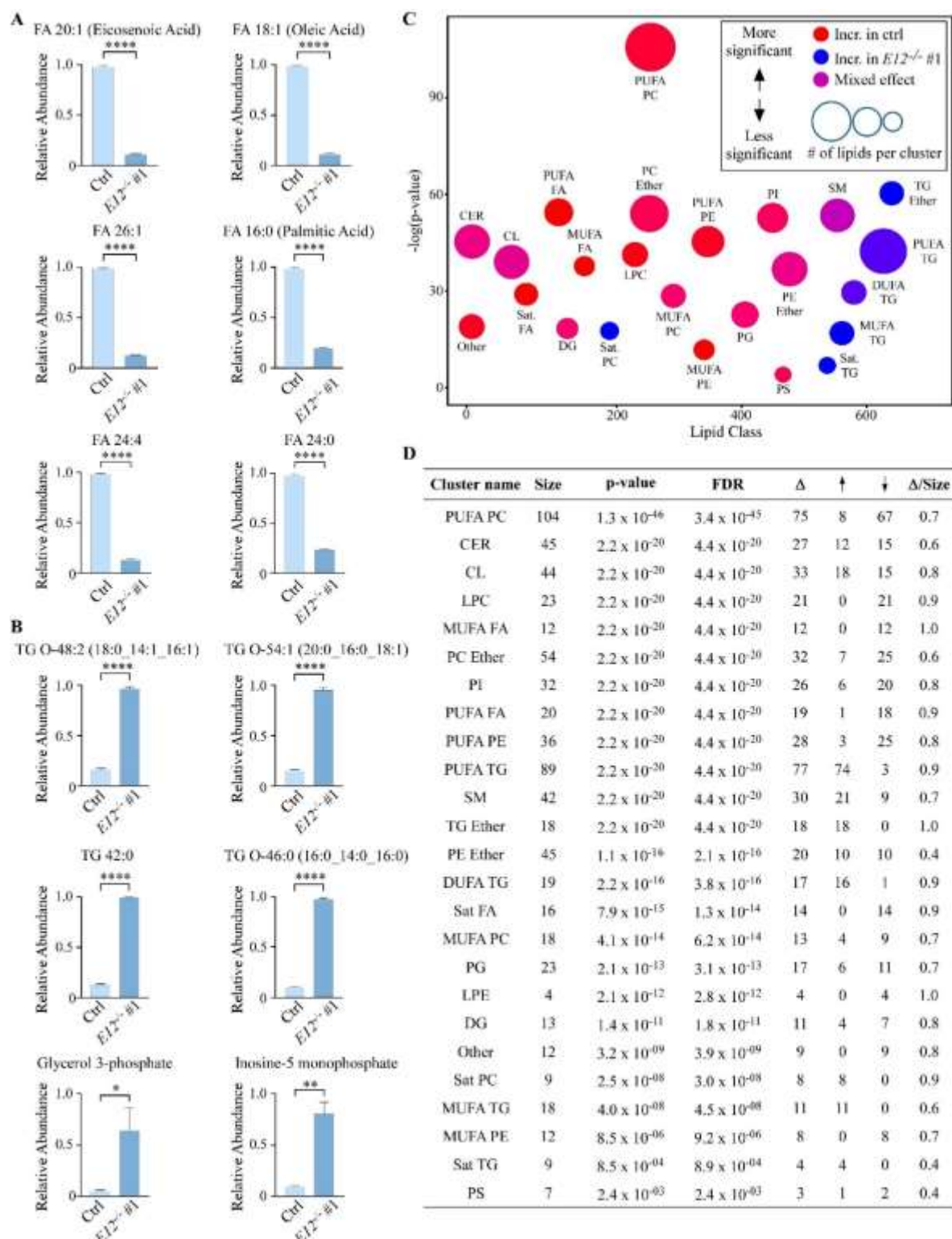


Figure 2. Loss of *E12* leads to lipidome changes in H1299 cells. A-B. (A) Top six downregulated and (B) upregulated metabolites in *E12*^{-/-} compared to isogenic control H1299 cells. TG-O indicates triacylglycerols with an ether bond. Statistical significance was determined using Student's *t*-test. Data are presented as mean \pm SEM. $n = 3$ independent experiments. * $p < 0.05$, ** $p < 0.01$, **** $p < 0.0001$. (C). ChemRICH of all lipids identified in isogenic control and *E12*^{-/-} H1299 cells. Y-

axis represents statistical significance assessed by Kolmogorov-Smirnov test and node size represents total number of lipids per cluster. MUFA: mono-unsaturated fatty acids; DUFA: di-unsaturated fatty acids; PUFA: poly-unsaturated fatty acids; Sat: saturated. (D). Lipid clusters with significant alterations due to loss of *E12* determined by ChemRICH analysis. Δ indicates number of lipids altered in a cluster; \uparrow indicates number of increased lipids in *E12*^{-/-} compared to isogenic control H1299 cells; \downarrow indicates number of decreased lipids in *E12*^{-/-} compared to isogenic control H1299 cells; FDR indicates false discovery rate; Δ /size shows the proportion of significantly altered lipids within each class.

3.3. Kennedy Pathway Metabolites Are Altered upon Loss of *E12* in H1299 Cells

As previously discussed, PCs are formed through the Kennedy pathway, the Lands Cycle, or the PEMT pathway (Figure 3A). ChemRICH analyses indicated that the Kennedy pathway was altered, so levels of PCs, LPCs, PEs, and lysophosphatidylethanolamines (LPEs) were further analyzed. Loss of *E12* led to a significant decrease in the four PC synthesis lipids compared to isogenic control cells (Figure 3B,C). Levels of the PEMT pathway methyl donor S-adenosylmethionine were more significantly increased in *E12*-KO cells, compared to the product of this reaction, S-adenosylhomocysteine (Figure S2A). These data suggest that the PEMT pathway might be inhibited by loss of *E12*, therefore leading to decreased PC production. We then postulated that loss of *E12* was altering the expression of genes involved in PC synthesis, thus explaining the observed lipid changes. To test this, previously generated RNA-seq data was analyzed and showed that several key genes involved in PC synthesis were differentially expressed in *E12*-KO cells compared to isogenic control cells (Figure 3D). mRNA and protein levels of several of these targets were then confirmed via qPCR and Western blot analysis. CCT α (encoded by *PCYT1A*) and CEPT1, two enzymes directly involved in PC synthesis, were significantly downregulated at the mRNA level and markedly decreased at the protein level in *E12*-KO cells compared to isogenic control cells (Figure 3E,F). Furthermore, SMPD4, which hydrolyzes sphingomyelin to ceramide and P-choline (Figure 3A), exhibited the same trend at both the mRNA and protein levels (Figure 3G). These data suggest that decreased PC levels in *E12*-KO cells are partly attributed to decreased expression of enzymes involved in PC synthesis.

DGs are necessary for the final step of PC synthesis and are also converted to TGs through the addition of acyl-CoA, which is catalyzed by diacylglycerol transferases (DGAT) [46] (Figure 3A). Levels of DGs and FAs were found to be significantly decreased in *E12*-KO cells, but TGs were significantly increased compared to isogenic control cells (Figure 3I). FAs are stored primarily as TGs [47], so increased TGs in *E12*-KO cells might explain why FAs are lower than in isogenic control cells. Moreover, the RNA-seq data showed that *DGAT1* and *DGAT2* were upregulated in *E12*-KO cells (Figure 3D), suggesting that DGs were shuttled more towards TG formation, rather than PC synthesis.

As previously mentioned, increased choline import is essential for tumor cells to maintain high levels of PCs. Due to this, it was determined whether decreased choline import was contributing to decreased PC levels in *E12*-KO cells. mRNA and protein levels of a major choline importer, CTL1 (encoded by *SLC44A1*), were analyzed and found to be unchanged in *E12*-KO cells compared to isogenic control cells (Figure 3H). Next, LC-MS/MS metabolomics was conducted to investigate intracellular choline and ethanolamine levels, and both were found to be significantly increased in *E12*-KO cells compared to isogenic control cells (Figure 3J). We hypothesize that the accumulation of choline and ethanolamine in *E12*-KO cells resulted from the decreased flux of these metabolites through the Kennedy pathway due to decreased expression of downstream genes, as discussed above. Altogether, these findings indicate that loss of *E12* leads to decreased PC levels due to decreased expression of enzymes directly or indirectly involved in PC/PE synthesis, and not due to decreased choline import.

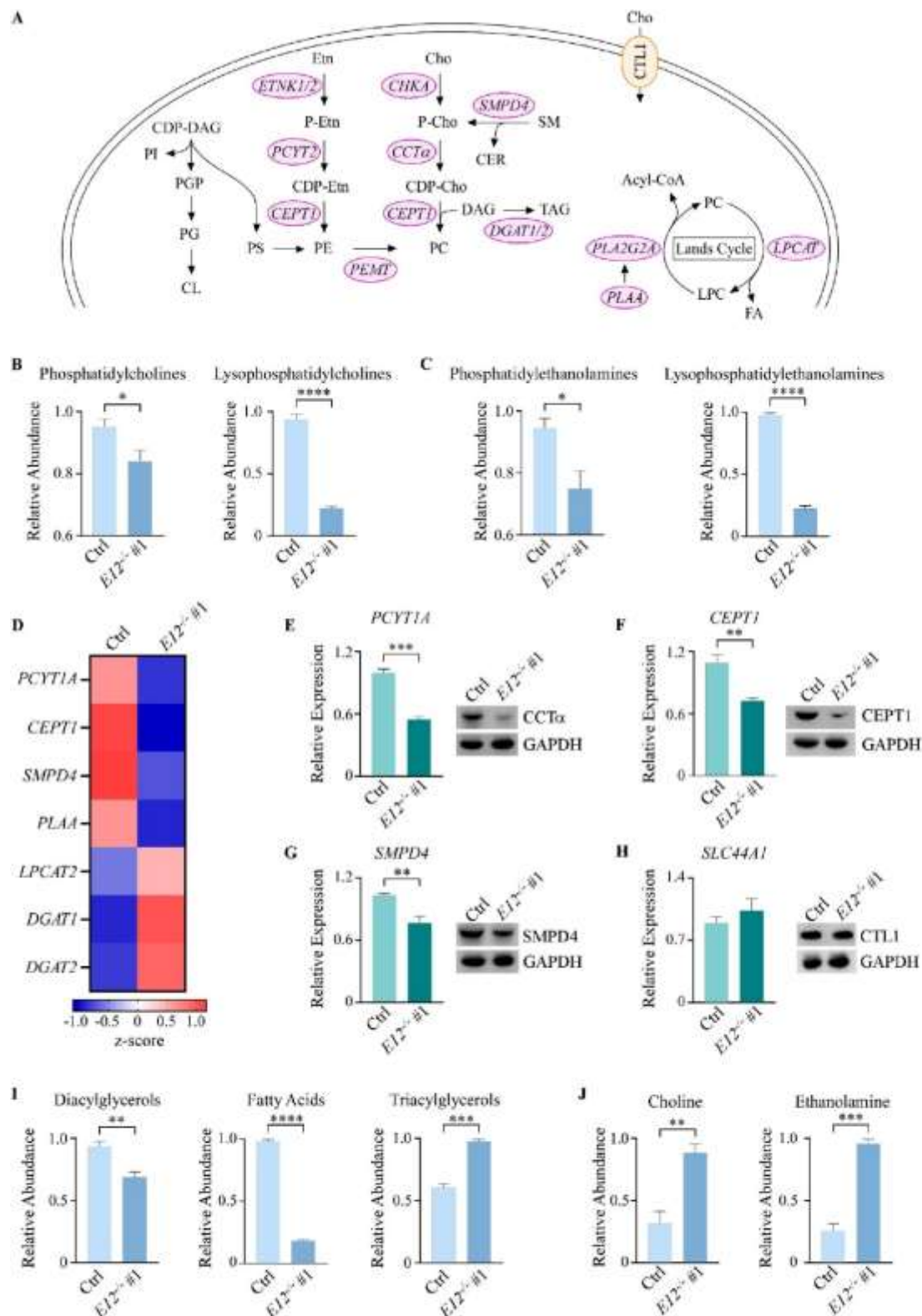


Figure 3. Kennedy pathway metabolites are altered upon knockout of *E12* in H1299 cells. **(A).** Schematic overview of the Kennedy pathway. CDP-DAG: CDP-diacylglycerol; PI: phosphatidylinositol; PG: phosphatidylglycerol; CL: cardiolipin; PS: phosphatidylserine; Cho: choline; P-cho: phosphocholine, (CDP-cho: cytidine diphosphate-choline; Etn: ethanolamine, P-Etn: phosphoethanolamine; CDP-Etn:

cytidine diphosphate-ethanolamine; SM: sphingomyelin; CER: ceramide; DAG: diacylglycerol; TAG: triacylglycerol; FA: fatty acid; CTL1: choline transporter-like protein 1. **B,C**). Relative abundance of **(B)** phosphatidylcholines and lysophosphatidylcholines and **(C)** phosphatidylethanolamines and lysophosphatidylethanolamines in isogenic control and $E12^{-/-}$ H1299 cells. Statistical significance was determined using Student's *t*-test. **(D)**. Heat map of differentially expressed genes identified by RNA-seq analysis in isogenic control and $E12^{-/-}$ H1299 cell lines. Color density indicating z-score values was displayed below. **(E-H)**. (Left) qPCR was used to quantify relative mRNA levels of *PCYT1A*, *CEPT1*, *SMPD4*, and *SLC44A1* in isogenic control and $E12^{-/-}$ H1299 cell lines. All values were normalized to *HPRT1* and are presented as relative to isogenic control (light green). Statistical significance was determined using Student's *t*-test. (Right) Western blot analysis was used to determine CCTa, *CEPT1*, *SMPD4*, *CTL1*, and *GAPDH* protein levels in isogenic control and $E12^{-/-}$ H1299 cell lines. **(I,J)**. Relative abundance of **(I)** diacylglycerols, fatty acids, and triacylglycerols, and **(E)** choline and ethanolamine in isogenic control and $E12^{-/-}$ H1299 cells. Statistical significance was determined using Student's *t*-test. For B-C and E-J. Data presented as mean \pm SEM. $n = 3$ independent experiments. * $p < 0.05$, ** $p < 0.01$, *** $p < 0.001$, **** $p < 0.0001$.

3.4. Loss of *E12* Alters PC Chain Length and Saturation in H1299 Cells

Multiple studies show that increased FA chain length and desaturation are associated with malignancy and tumorigenesis [48,49]. In this study, loss of *E12* did not alter levels of long-chain fatty acids (LCFAs), but levels of very long-chain fatty acids (VLCFAs) were significantly decreased compared to isogenic control cells (Figure S2B). Consistent with the data in Figure 2D, a deeper analysis of PC saturation showed that, when compared to isogenic control cells, *E12*-KO cells had significantly higher levels of PCs containing saturated FAs and lower levels of PCs containing MUFAs, DUFAs, and PUFAs (Figure 4A). These findings suggest that loss of *E12* leads to dysregulation of PC chain length and saturation.

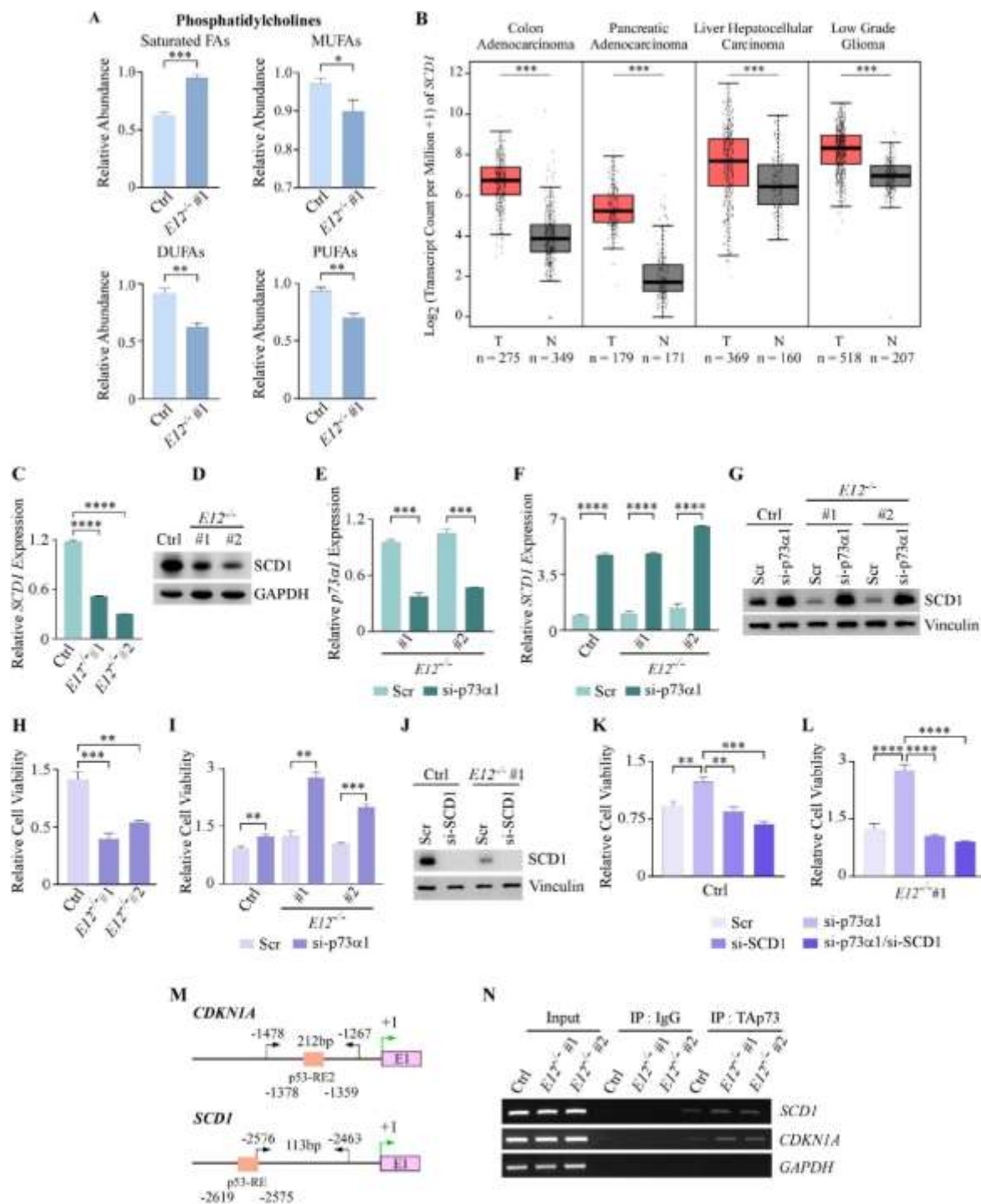


Figure 4. p73 α 1 suppresses cell viability by directly inhibiting *SCD1* expression. (A). Relative abundance of PC saturation level in isogenic control and *E12*^{-/-} H1299 cells. Statistical significance was determined using Student's *t*-test. (B). *SCD1* transcript counts in the indicated tumors (data from TCGA) and the matched normal tissues (data from TCGA and GTEx) were analyzed via Gene Expression Profiling Interactive Analysis (GEPIA; <http://gepia.cancer-pku.cn/index.html>); accessed on 6 May 2022). T: tumor; N: matched normal tissue. (C). qPCR was used to quantify relative mRNA levels of *SCD1* in isogenic control and *E12*^{-/-} H1299 cell lines. All values were normalized to *HPRT1* and are presented as relative to isogenic control (light green). Statistical significance was determined

using one-way ANOVA. (D). Western blot analysis was used to determine SCD1 and GAPDH protein levels in isogenic control and $E12^{-/-}$ H1299 cell lines. (E). qPCR was used to quantify relative mRNA levels of $p73\alpha1$ in $E12^{-/-}$ H1299 cells treated with scramble siRNA (Scr) or si- $p73\alpha1$ for 48 h. All values were normalized to *HPRT1* and are presented as relative to each Scr-treated cell line. Statistical significance was determined using multiple Student's *t*-tests comparing Scr to si- $p73\alpha1$ treatment for each cell line. (F). Cells were treated as in (C) and qPCR was used to quantify relative mRNA levels of *SCD1*. All values were normalized to *HPRT1* and are presented as relative to each Scr-treated cell line. Statistical significance was determined using multiple Student's *t*-tests comparing Scr to si- $p73\alpha1$ treatment for each cell line. (G). Cells were treated as in (C) and Western blot analysis was used to determine SCD1 and Vinculin protein levels. (H). Cells were treated as in (C) and cell viability of the Scr-treated cell lines was determined using CellTiter-GLO. Cell viability for $E12^{-/-}$ #1 and #2 (dark purple) were presented as relative to isogenic control cells (light purple). Statistical significance was determined using one-way ANOVA. (I). Cells were treated as in (C) and cell viability was determined using CellTiter-GLO. Cell viability for isogenic control cells treated with si- $p73\alpha1$ was presented as relative to isogenic control Scr-treated cells. Cell viability for $E12^{-/-}$ #1 cells treated with si- $p73\alpha1$ was presented as relative to $E12^{-/-}$ #1 Scr-treated cells. Cell viability for $E12^{-/-}$ #2 cells treated with si- $p73\alpha1$ was presented as relative to $E12^{-/-}$ #2 Scr-treated cells. Statistical significance was determined using multiple Student's *t*-tests comparing Scr to si- $p73\alpha1$ treatment for each cell line. (J). Western blot analysis of SCD1 and Vinculin proteins in isogenic control and $E12^{-/-}$ H1299 cell lines treated with Scr or si-*SCD1* for 48 h. (K). Cell viability was determined using CellTiter-GLO in the isogenic control H1299 cell line treated with Scr, si- $p73\alpha1$, si-*SCD1*, or si- $p73\alpha1$ and si-*SCD1* for 48 h. Cell viability for isogenic control cells treated with si- $p73\alpha1$, si-*SCD1*, or si- $p73\alpha1$ and si-*SCD1* was presented as relative to isogenic control Scr-treated cells. Statistical significance was determined using one-way ANOVA. (L). Cell viability was determined using CellTiter-GLO in the $E12^{-/-}$ H1299 cell line treated with Scr, si- $p73\alpha1$, si-*SCD1*, or si- $p73\alpha1$ and si-*SCD1* for 48 h. Cell viability for $E12^{-/-}$ cells treated with si- $p73\alpha1$, si-*SCD1*, or si- $p73\alpha1$ and si-*SCD1* was presented as relative to $E12^{-/-}$ Scr-treated cells. Statistical significance was determined using one-way ANOVA. (M). Diagram of the putative p53-Response Elements (p53-RE) (orange) in the promoter of *CDKN1A* and *SCD1*. Locations of the primers used to amplify the p53-RE in the promoters of *CDKN1A* and *SCD1* are indicated by the black arrows. Green arrows indicate transcription start site; E1 indicates exon 1. (N). ChIP analysis was performed with isogenic control and $E12^{-/-}$ H1299 cells. Cell lysates were immunoprecipitated with anti-rabbit IgG or anti-TAp73 to bring down the DNA-protein complex. DNA fragments were visualized by PCR with primers for *SCD1*, *CDKN1A*, and *GAPDH* promoters. For (A,C,E,F,H,I,K,L). Data are presented as mean \pm SEM. $n = 3$ independent experiments. * $p < 0.05$, ** $p < 0.01$, *** $p < 0.001$, **** $p < 0.0001$.

3.5. $p73\alpha1$ Suppresses Cancer Cell Viability by Directly Inhibiting SCD1 Expression in H1299 Cells

The finding that loss of *E12* led to increased saturated FAs and decreased MUFAs was further explored given the importance of MUFAs in tumorigenesis. There are three human desaturase enzymes ($\Delta5$, $\Delta6$ and $\Delta9$) that are responsible for the formation of MUFAs, DUFAs, and PUFAs [50,51]. The rate-limiting step is the conversion of saturated FAs to MUFAs, which is catalyzed by $\Delta9$ desaturase, or SCD1 [52]. SCD1 primarily catalyzes the formation of palmitoleic acid (FA 16:1) and oleic acid (FA 18:1) from palmitic acid (FA 16:0) and stearic acid (18:0), respectively [53]. Oleic acid and palmitoleic acid are the most abundant intracellular MUFAs and are necessary for the production of many lipids [54]. Interestingly, increased SCD1 expression is highly implicated in a variety of cancer types because of the tumorigenic properties of MUFAs [55–57]. Analysis of The Cancer Genome Atlas and the Genotype-Tissue Expression databases showed that *SCD1* transcript levels were significantly increased in 17 out of 31 tumor types compared to the matched normal tissues (Figure 4B; Figure S3A,B). Previously, p53 was identified as a direct suppressor of *SCD1* expression [58], and it is known that p73 can bind to p53-response elements to regulate target gene expression [59]. Given this, we hypothesized that $p73\alpha1$ directly inhibits *SCD1* expression, therefore suppressing cancer cell proliferation.

To test this, *SCD1* mRNA and protein levels were analyzed in isogenic control and E12-KO H1299 cell lines. mRNA levels were significantly decreased, and protein levels were considerably decreased in E12-KO cells compared to isogenic control cells (Figure 4C,D). Next, p73 α 1-specific siRNA was used to determine whether p73 α 1 was responsible for the observed decrease in *SCD1* mRNA and protein levels (Figure 4E). Indeed, the data revealed that knockdown of p73 α 1 in both isogenic control and E12-KO cells led to a significant increase in *SCD1* mRNA levels, and a consistent increase at the protein level (Figure 4F,G). We then wanted to determine whether p73 α 1-mediated suppression of *SCD1* expression was contributing to the previously described tumor suppressive effects of p73 α 1. First, it was reiterated that loss of *E12* leads to decreased cell viability (Figure 4H), and that p73 α 1 was responsible for the growth-suppressive effects (Figure 4I). Next, siRNA targeting p73 α 1 and *SCD1* (Figure 4J) was used to determine whether p73 α 1-mediated suppression of *SCD1* inhibits cancer cell proliferation. In both isogenic control and E12-KO cells, knockdown of *SCD1*, alone or with p73 α 1, led to a significant decrease in cell viability compared to knockdown of only p73 α 1 (Figure 4K,L). Moreover, knockdown of p73 α 1 and *SCD1* did not elicit a significant difference in cell viability compared to knockdown of *SCD1* alone (Figure 4K,L), confirming that p73 α 1-mediated suppression of *SCD1* contributes to the decreased cell viability in E12-KO cells.

To determine whether p73 α 1 was directly inhibiting *SCD1* expression, a chromatin immunoprecipitation (ChIP) assay was performed in isogenic control and E12-KO cell lines (Figure 4M). The data showed that DNA fragments containing the putative p53-response element in the *SCD1* promoter were detected following immunoprecipitation with TAp73 antibody in both isogenic control and E12-KO cell lines (Figure 4N). Taken together, these data identify *SCD1* as a direct target of p73 α 1 and show that p73 α 1-mediated suppression of *SCD1* expression contributes to the tumor suppressive effects of p73 α 1.

3.6. p73 α 1-Mediated Suppression of *SCD1* Leads to an Increased Ratio of Stearic Acid to Oleic Acid in H1299 Cells

As previously mentioned, palmitic acid and stearic acid are the major substrates for *SCD1*, leading to the formation of palmitoleic acid and oleic acid, respectively (Figure 5A). Due to the findings that p73 α 1 directly suppresses *SCD1* expression, it was determined whether this affected the levels of these four lipids. E12-KO cells had significantly decreased levels of these four FAs compared to isogenic control cells (Figure 5B,C). Next, the ratios of saturated FAs to MUFAs were analyzed because a change in *SCD1* expression and/or activity would alter these ratios. Indeed, the data showed that the ratios of palmitic acid to palmitoleic acid and stearic acid to oleic acid were significantly increased in E12-KO cells compared to isogenic control cells (Figure 5D). Additionally, the ratios of saturated FAs to MUFAs of varying chain lengths were analyzed, and 8 out of 9 were significantly increased in E12-KO cells compared to isogenic control cells (Figure 5E).

To confirm that p73 α 1-mediated suppression of *SCD1* expression leads to an increased ratio of saturated FAs to MUFAs, lipidomic analysis was performed following knockdown of p73 α 1 or p73 α 1 and *SCD1*. The ratio of stearic acid to oleic acid was significantly decreased after knockdown of p73 α 1, with a similar, albeit not significant, trend seen in the ratio of palmitic acid to palmitoleic acid in E12-KO cells (Figure 5F). Following knockdown of both p73 α 1 and *SCD1* in E12-KO cells, there was a significant increase in the ratio of stearic acid to oleic acid, but not in the ratio of palmitic acid to palmitoleic acid (Figure 5F). A similar trend for both ratios was found in the isogenic control cells (Figure 5G). Taken together, these data identify p73 α 1 as a transcriptional repressor of *SCD1*, which leads to an increased ratio of stearic to oleic acid.

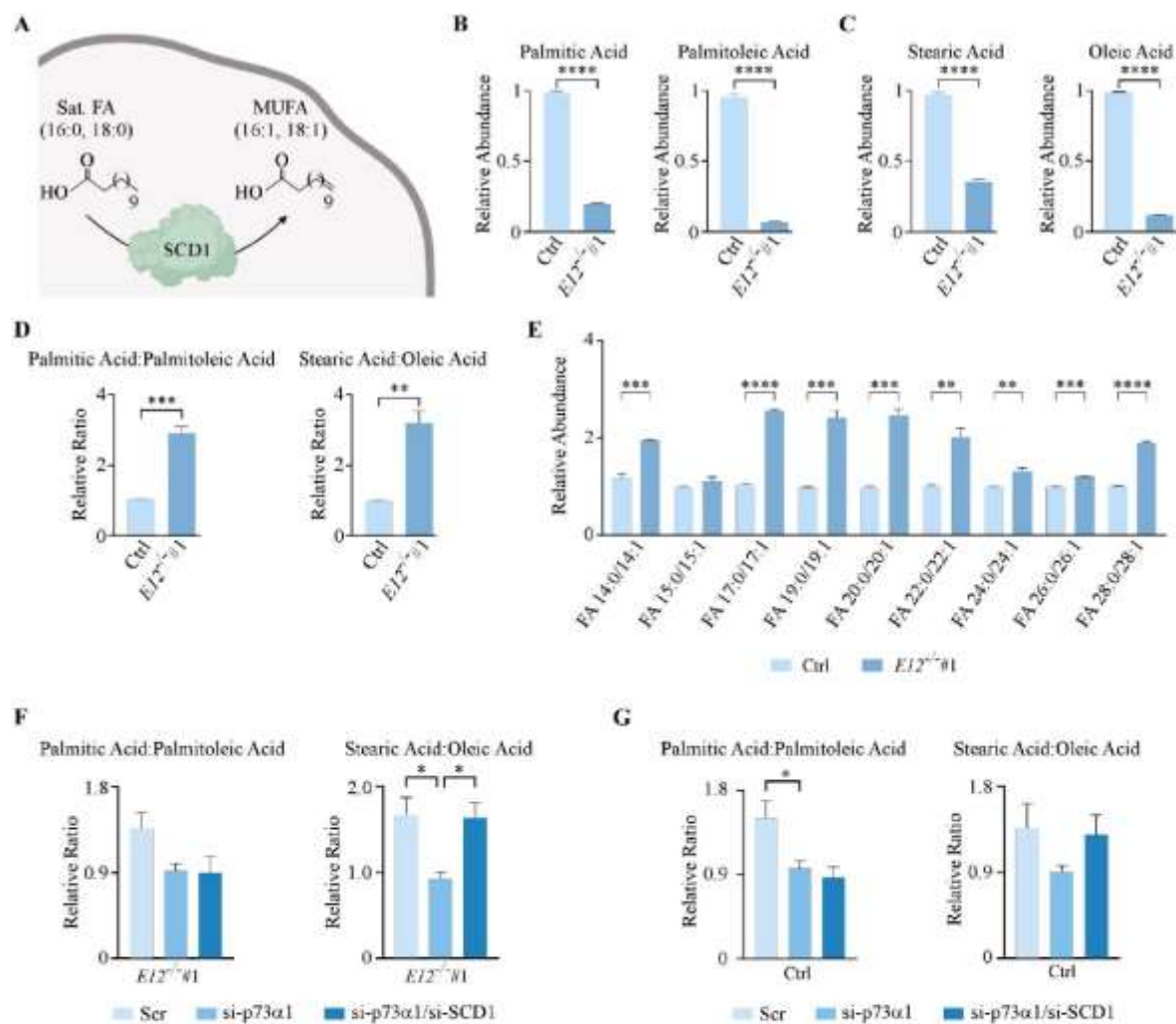


Figure 5. p73 α 1-mediated suppression of SCD1 leads to an increased ratio of saturated FAs to MUFAs. (A). Schematic representation of SCD1 enzymatic activity. (B,C). Relative abundance of (B) palmitic acid and palmitoleic acid and (C) stearic acid and oleic acid in isogenic control and $E12^{-/-}$ H1299 cells. Statistical significance was determined using Student's t -test. (D). Ratio of (left) palmitic acid to palmitoleic acid and (right) stearic acid to oleic acid in isogenic control and $E12^{-/-}$ H1299 cells. Statistical significance was determined using Student's t -test. (E). Ratio of saturated FAs to MUFAs for the indicated FA chain length in isogenic control (light blue) and $E12^{-/-}$ (dark blue) H1299 cells. Statistical significance was determined using multiple Student's t -tests comparing isogenic control and $E12^{-/-}$ cell lines for each saturated/unsaturated FA pair. (F). Ratio of (left) palmitic acid to palmitoleic acid and (right) stearic acid to oleic acid in $E12^{-/-}$ H1299 cells following treatment with Scr, si-SCD1, or si-SCD1 and si-p73 α 1 for 48 h. Statistical significance was determined using one-way ANOVA. (G). Ratio of (left) palmitic acid to palmitoleic acid and (right) stearic acid to oleic acid in isogenic control H1299 cells treated with Scr, sip73 α 1, or sip73 α 1 and siSCD1 for 48 h. Statistical significance was determined using one-way ANOVA. For B-G. Data are presented as mean \pm SEM. $n = 3$ independent experiments. * $p < 0.05$, ** $p < 0.01$, *** $p < 0.001$, **** $p < 0.0001$.

4. Discussion

SCD1 promotes tumorigenesis through a decreased ratio of saturated FAs to MUFAs [55–57]. Phospholipids containing MUFAs are less susceptible to lipid peroxidation than saturated FAs and PUFAs, therefore conferring resistance to ferroptosis [60,61]. Moreover, mass-spectrometry-based imaging showed that PCs containing MUFAs were more abundant in cancerous tissues compared to matched normal tissues [62]. Conversely, the accumulation of saturated FAs causes lipotoxicity, and in most cases cell death, by promoting endoplasmic reticulum stress [63]. These findings support a mechanism for how suppression of *SCD1* expression via p73 α 1 leads to decreased cancer cell viability in E12-KO cells. In the present study, we found that p73 α 1-knockdown decreased the ratio of stearic acid to oleic acid, while knockdown of both p73 α 1 and *SCD1* reversed these effects. Interestingly, the reversal following concurrent knockdown was not observed in the ratio of palmitic acid to palmitoleic acid. One report noted that some cancer cells are able to utilize Δ 6 desaturase (*FADS2*) to produce cis-6-C16:1 (FA 16:1; sapienate) [64], which differs from palmitoleic acid in the location of the double bond. By itself, *FADS2* might be able to compensate for the loss of *SCD1*, which is why the ratio of FA 16:0 to FA 16:1 is not increased following *SCD1* knockdown. However, we were unable to give detailed chemical analyses of the possible FA 16:1-containing isomers because current metabolomics methods cannot determine the location of double bonds in complex lipids. Such detailed analyses may be possible in the future by adding ultraviolet photodissociation mass spectrometry [65], chemical derivatization such as ozonolysis [66], or electron-activated dissociation mass spectrometry [67].

Cancer cells are able to increase uptake and/or biosynthesis of FAs, allowing for increased energy for various cellular processes, such as growth and proliferation [68]. In this study, we not only found that loss of *E12* altered the ration of saturated FAs to MUFAs, but we also showed that, overall, FA abundance was decreased upon E12-KO. We hypothesize that decreased FA abundance in E12-KO cells could also be contributing to the observed decrease in cell viability. Moreover, decreased abundance of FAs could lead to decreased mitochondrial FA oxidation, which has been shown to be increased in tumorigenic cells [68]. As such, it would be interesting to explore the relationship between cancer cell viability and FA abundance and oxidation in E12-KO cells in future work.

In addition to the actual biochemical differences that we observed, we are also able to interpret these changes with respect to the organelles that may be most likely involved. The peroxisome is a key organelle involved in lipid metabolism, immunometabolism, and cellular redox balance. It is the only organelle that catabolizes VLCFAs and branched-chain FAs, and converts FAs and alcohols to ether-linked lipids. Our data showed that the loss of *E12* resulted in increased catabolism of VLCFAs, indicating alterations to peroxisomal activity. Additional lines of evidence to support this notion are increased levels of ether-linked TG lipids in E12-KO cells compared to isogenic control cells. Interestingly, phosphoether lipids did not show differences in abundance, in contrast with ether-linked TG lipids. Such a phenomenon has not been reported before. Many studies have shown that peroxisomal alterations contribute to cancer and inflammation. A link of peroxisomal activity to cancer cell autophagy was previously shown by the impaired ability of CD8 + T-cells to kill malignant cells that were associated with an accumulation of LCFAs and VLCFAs within the tumor microenvironment [69]. Ether-linked lipids have also been shown to be elevated in various tumors compared to control tissues, and show a linear relationship with metastatic spread in breast, prostate, and lung cancers [68,70,71]. We previously reported that *E12*^{+/-} mice had increased immune cell infiltration and inflammation [37], which may be explained by peroxisomal-derived inflammatory cytokines and metabolites (prostaglandins, leukotrienes, thromboxanes) and immune cell activation through redox homeostasis. Future research will examine the role of the peroxisome in relationship to p73 α 1 to better understand tumor microenvironment and metabolism, and overall cancer cell phenotypes.

5. Conclusions

In this study, we identified a role for p73 α 1 in lipid metabolism through direct regulation of SCD1, which alters the ratio of saturated FAs to MUFAs and decreases cancer cell viability. Taken together, our data indicate that p73 has a critical role in regulating the metabolome and lipidome, which may contribute to oncogenesis, redox balance, and immunometabolic signaling. As such, it would be of great interest to further investigate how the various p73 isoforms alter biochemical pathways, thus influencing the tumor microenvironment and cancer metabolism.

Supplementary Materials: The following supporting information can be downloaded at: <https://www.mdpi.com/article/10.3390/cells11162516/s1>, Figure S1: Loss of *E12* alters the lipidome in H1299 cells; Figure S2: Metabolites involved in PC synthesis are altered upon loss of *E12*; Figure S3: *SCD1* transcript counts are increased in certain cancer types; Table S1: Primers used to generate expression vectors; Table S2: Primers used for qPCR and ChIP.

Author Contributions: Conceptualization, Z.R., K.L., T.S., S.M., J.Z., X.C. and O.F.; methodology, Z.R., K.L., T.S., S.M., J.Z., X.C. and O.F.; validation, Z.R., K.L., T.S. and S.M.; formal analysis, Z.R. and K.L.; investigation, Z.R., K.L. and X.K.; writing—original draft, Z.R. and K.L.; writing—review and editing, Z.R., K.L., O.F. and X.C.; visualization, Z.R. and K.L.; supervision, T.S., S.M., J.Z., O.F. and X.C.; funding acquisition, K.L., J.Z., O.F. and X.C. All authors have read and agreed to the published version of the manuscript.

Funding: This work was supported in part by NIH T32 HL007013 to K.L., NIH RO1 CA081237 to X.C., California TRDRP T31IP1727 to J.Z., P30 AG072972 and NIH U19 AG023122 to O.F.

Institutional Review Board Statement: Not applicable.

Informed Consent Statement: Not applicable.

Data Availability Statement: Available upon request.

Acknowledgments: The authors want to thank members of the Chen-Zhang and Fiehn Labs for their support.

Conflicts of Interest: The authors declare no conflict of interest.

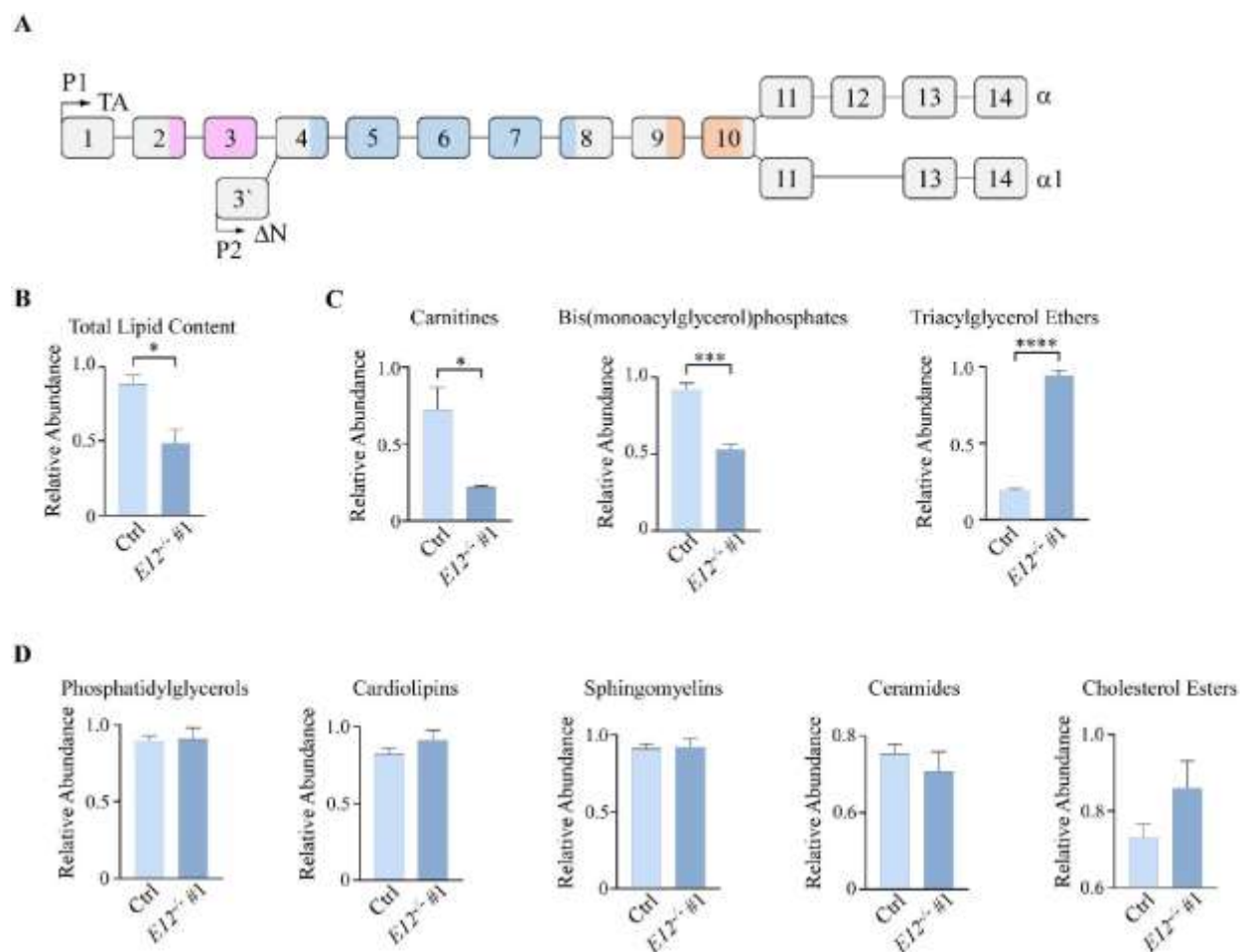


Fig. S1. Loss of *E12* alters the lipidome in H1299 cells.

A. *TP73* diagram showing that loss of exon 12 leads to isoform switch from p73 α to p73 α 1. Pink region indicates transactivation domain, blue region indicates DNA binding domain, and orange region indicates oligomerization domain. P1: promoter 1; P2: promoter 2.

B. Relative abundance of total lipid content in isogenic control and *E12*^{-/-} H1299 cells. Statistical significance was determined using Student's t-test.

C. Relative abundance of carnitines, bis(monoacylglycerol)phosphates, and triacylglycerol ethers in isogenic control and *E12*^{-/-} H1299 cells. Statistical significance was determined using Student's t-test.

D. Relative abundance of phosphatidylglycerols, cardiolipins, sphingomyelins, ceramides, and cholesterol esters in isogenic control and *E12*^{-/-} H1299 cells. Statistical significance was determined using Student's t-test.

For B-D. Data are presented as mean \pm SEM. n = 3 independent experiments. * p < 0.05, *** p < 0.001, **** p < 0.0001.

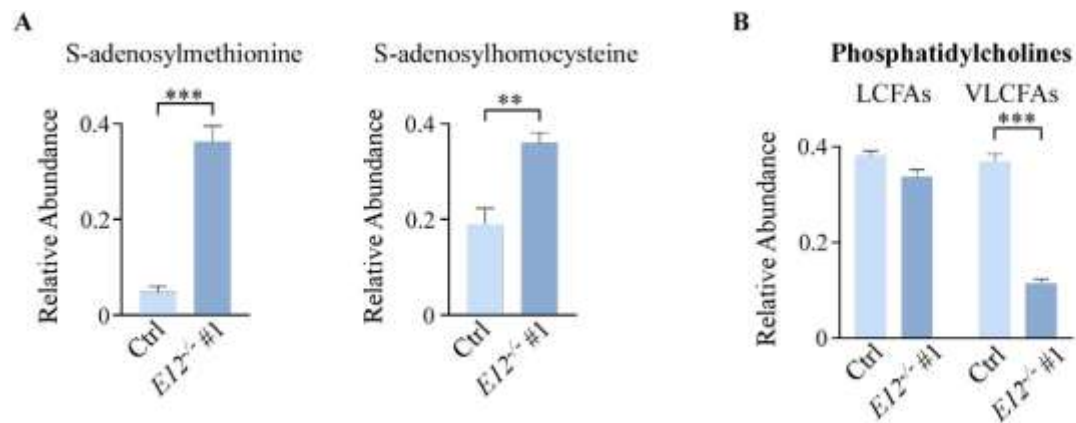


Fig. S2. Metabolites involved in PC synthesis are altered upon loss of *E12*.

A. Relative abundance of S-adenosylmethionine and S-adenosylhomocysteine in isogenic control and *E12*^{-/-} H1299 cell lines. Statistical significance was determined using Student's t-test.

B. Relative abundance of PCs containing (left) long-chain fatty acids (LCFAs) and (right) very long-chain fatty acids (VLCFAs) in isogenic control and *E12*^{-/-} H1299 cell lines. Statistical significance was determined using Student's t-test.

For A-B. Data presented as mean \pm SEM. n = 3 independent experiments. ** p < 0.01, *** p < 0.001.

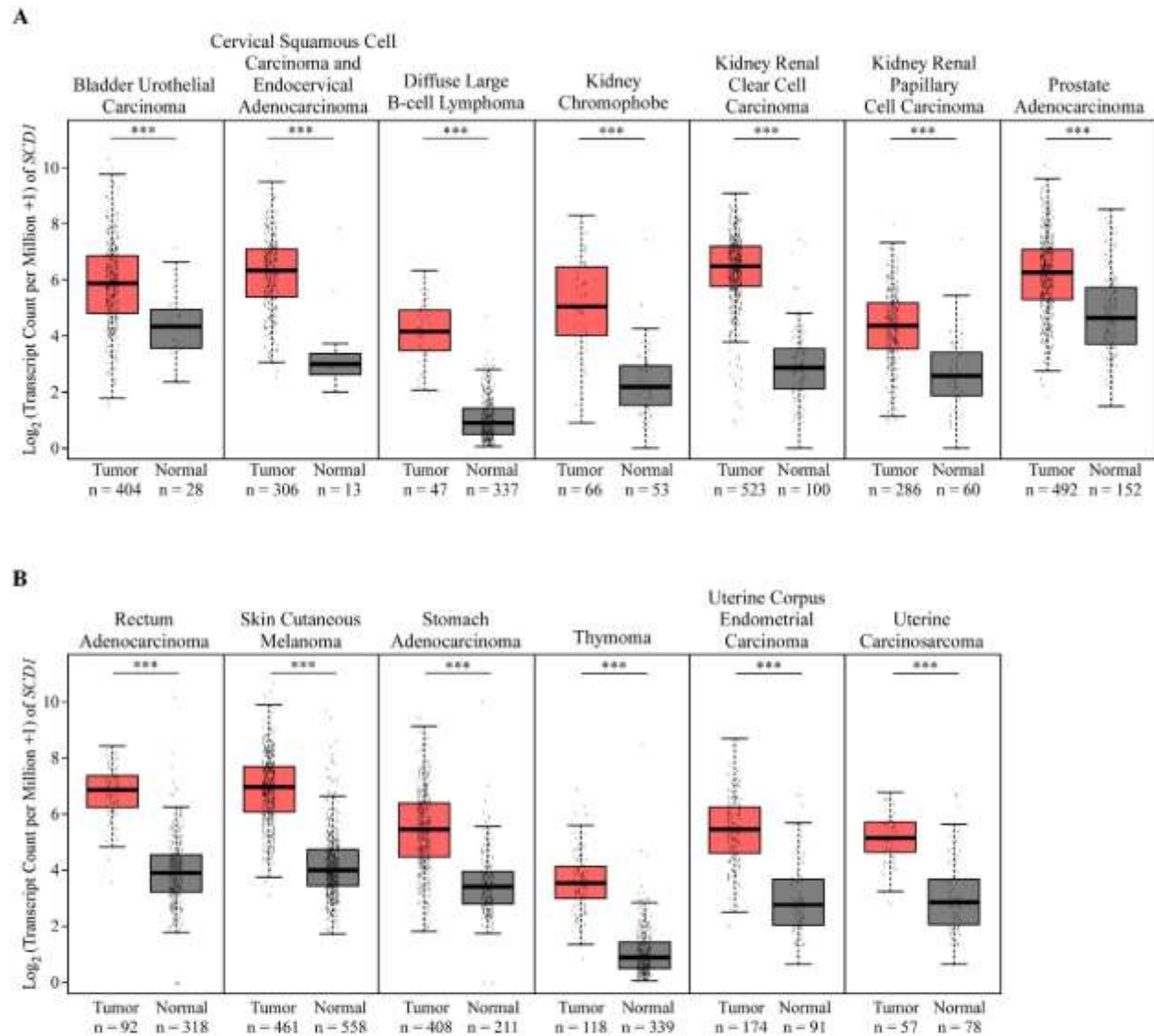


Fig. S3. *SCD1* transcript counts are increased in certain cancer types.

A-B. *SCD1* transcript counts in the indicated tumors (data from TCGA) and the matched normal tissues (data from TCGA and GTEx) were analyzed via Gene Expression Profiling Interactive Analysis (GEPIA, <http://gepia.cancer-pku.cn/index.html>). *** $p < 0.001$.

Table S1. Primers used to generate expression vectors.

Name	Oligonucleotide	Sequence
p73-E12-gRNA-1- pSpCas9(BB)-2A-Puro	Sense	5'-CACCGCGTCACATCGCCAGGCCTT-3'
	Antisense	5'-AAACAAGGCCTGGCGATGTGACGC-3'
p73-E12-gRNA-2- pSpCas9(BB)-2A-Puro	Sense	5'-CACCGCTGCTGCTCATCTCGCCGT-3'
	Antisense	5'-AAACACGGCGAGATGAGCAGCAGC-3'

Table S2. Primers used for qPCR and ChIP.

<i>TP73α1</i>	Sense	5'-CACCGTCAAACGTGGTGCCCCCATC-3'
	Antisense	5'-AAACGATGGGGGCACCACGTTTGAC-3'
<i>SCD1</i>	Sense	5'-CACTTGGGAGCCCTGTATGG-3'
	Antisense	5'-TGAGCTCCTGCTGTTATGCC-3'
<i>PCYT1A</i>	Sense	5'-GAGTTGCAGCATGTGCCGA-3'
	Antisense	5'-GCATTGACCTTGGCTGAACA-3'
<i>CEPT1</i>	Sense	5'-GGCAGTGATTGGAGGACCAC-3'
	Antisense	5'-TGCCAACACCACCTGTGAAG-3'
<i>SMPD4</i>	Sense	5'-GACTCCAGCCCCGGTGT-3'
	Antisense	5'-CCACTCGGAACACCATGAG-3'
<i>SLC44A1</i>	Sense	5'-GCAGAGCTCCAAACGAGAA-3'
	Antisense	5'-AGCCACAAATAAATCCCATCCC-3'
<i>HPRT1</i>	Sense	5'-CACCGCGTCACATCGCCAGGCCTT-3'
	Antisense	5'-AAACAAGGCCTGGCGATGTGACGC-3'
<i>SCD1-ChIP</i>	Sense	5'-TGCAGGGGTTTTTCGGAGTTT-3'
	Antisense	5'-TGAACGCCCTATTCCAGCCTTA-3'
<i>CDKN1A-ChIP</i>	Sense	5'-GGTCTGCTACTGTGTCCTCC-3'
	Antisense	5'-CATCTGAACAGAAATCCCAC-3'
<i>GAPDH-ChIP</i>	Sense	5'-AAAAGCGGGGAGAAAGTAGG-3'
	Antisense	5'-AAGAAGATGCGGCTGACTGT-3'

References

1. Tocher, D.R. Chapter 6 Glycerophospholipid metabolism. In *Biochemistry and Molecular Biology of Fishes*; ScienceDirect: Amsterdam, The Netherlands, 1995; pp. 119–157. [CrossRef]
2. Kanno, K.; Wu, M.K.; Scapa, E.F.; Roderick, S.L.; Cohen, D.E. Structure and function of phosphatidylcholine transfer protein (PC-TP)/StarD2. *Biochim. Biophys. Acta-Mol. Cell Biol. Lipids* **2007**, *1771*, 654–662. [CrossRef]
3. Gibellini, F.; Smith, T.K. The Kennedy pathway-de novo synthesis of phosphatidylethanolamine and phosphatidylcholine. *IUBMB Life* **2010**, *62*, 414–428. [CrossRef] [PubMed]
4. Moessinger, C.; Klizaitė, K.; Steinhagen, A.; Philippou-Massier, J.; Shevchenko, A.; Hoch, M.; Ejsing, C.S.; Thiele, C. Two different pathways of phosphatidylcholine synthesis, the Kennedy Pathway and the Lands Cycle, differentially regulate cellular triacylglycerol storage. *BMC Cell Biol.* **2014**, *15*, 43. [CrossRef] [PubMed]
5. Watkins, S.M.; Zhu, X.; Zeisel, S.H. Phosphatidylethanolamine-N-methyltransferase Activity and Dietary Choline Regulate Liver-Plasma Lipid Flux and Essential Fatty Acid Metabolism in Mice. *J. Nutr.* **2003**, *133*, 3386–3391. [CrossRef] [PubMed]
6. Michel, V.; Yuan, Z.; Ramsbair, S.; Bakovic, M. Choline transport for phospholipid synthesis. *Exp. Biol. Med.* **2006**, *231*, 490–504. [CrossRef]
7. Robichaud, P.P.; Surette, M.E. Polyunsaturated fatty acid-phospholipid remodeling and inflammation. *Curr. Opin. Endocrinol. Diabetes Obes.* **2015**, *22*, 112–118. [CrossRef]
8. Vance, D.E. Phospholipid methylation in mammals: From biochemistry to physiological function. *Biochim. Biophys. Acta-Biomembr.* **2014**, *1838*, 1477–1487. [CrossRef]
9. Harayama, T.; Eto, M.; Shindou, H.; Kita, Y.; Otsubo, E.; Hishikawa, D.; Ishii, S.; Sakimura, K.; Mishina, M.; Shimizu, T. Lysophospholipid acyltransferases mediate phosphatidylcholine diversification to achieve the physical properties required in vivo. *Cell Metab.* **2014**, *20*, 295–305. [CrossRef]
10. Cole, L.K.; Vance, J.E.; Vance, D.E. Phosphatidylcholine biosynthesis and lipoprotein metabolism. *Biochim. Biophys. Acta-Mol. Cell Biol. Lipids* **2012**, *1821*, 754–761. [CrossRef]
11. Hanahan, D.; Weinberg, R.A. Hallmarks of cancer: The next generation. *Cell* **2011**, *144*, 646–674. [CrossRef]
12. Snaebjornsson, M.T.; Janaki-Raman, S.; Schulze, A. Greasing the Wheels of the Cancer Machine: The Role of Lipid Metabolism in Cancer. *Cell Metab.* **2020**, *31*, 62–76. [CrossRef]
13. Saito, T.; Kuma, A.; Sugiura, Y.; Ichimura, Y.; Obata, M.; Kitamura, H.; Okuda, S.; Lee, H.C.; Ikeda, K.; Kanegae, Y.; et al. Autophagy regulates lipid metabolism through selective turnover of NCoR1. *Nat. Commun.* **2019**, *10*, 1567. [CrossRef] [PubMed]
14. Jain, M.; Nilsson, R.; Sharma, S.; Madhusudhan, N.; Kitami, T.; Souza, A.L.; Kafri, R.; Kirschner, M.W.; Clish, C.B.; Mootha, V.K. Metabolite profiling identifies a key role for glycine in rapid cancer cell proliferation. *Science* **2012**, *336*, 1040–1044. [CrossRef] [PubMed]
15. Daly, P.F.; Lyon, R.C.; Faustino, P.J.; Cohen, J.S. Phospholipid metabolism in cancer cells monitored by ³¹P NMR spectroscopy. *J. Biol. Chem.* **1987**, *262*, 14875–14878. [CrossRef]
16. Glunde, K.; Bhujwala, Z.M.; Ronen, S.M. Choline metabolism in malignant transformation. *Nat. Rev. Cancer* **2011**, *11*, 835–848. [CrossRef]
17. Zheng, Y.; Rodrik, V.; Toschi, A.; Shi, M.; Hui, L.; Shen, Y.; Foster, D.A. Phospholipase D Couples Survival and Migration Signals in Stress Response of Human Cancer Cells. *J. Biol. Chem.* **2006**, *281*, 15862–15868. [CrossRef] [PubMed]
18. Gomez-Cambronero, J. Phosphatidic acid, phospholipase D and tumorigenesis. *Adv. Biol. Regul.* **2014**, *54*, 197–206. [CrossRef]
19. Han, H.; Qi, R.; Zhou, J.J.; Ta, A.P.; Yang, B.; Nakaoka, H.J.; Seo, G.; Guan, K.L.; Luo, R.; Wang, W. Regulation of the Hippo Pathway by Phosphatidic Acid-Mediated Lipid-Protein Interaction. *Mol. Cell* **2018**, *72*, 328–340. [CrossRef] [PubMed]
20. Foster, D.A. Phosphatidic acid signaling to mTOR: Signals for the survival of human cancer cells. *Biochim. Biophys. Acta-Mol. Cell Biol. Lipids* **2009**, *1791*, 949–955. [CrossRef]
21. Wang, B.; Wu, L.; Chen, J.; Dong, L.; Chen, C.; Wen, Z.; Hu, J.; Fleming, I.; Wang, D.W. Metabolism pathways of arachidonic acids: Mechanisms and potential therapeutic targets. *Signal Transduct. Target. Ther.* **2021**, *6*, 94. [CrossRef]
22. Kaghad, M.; Bonnet, H.; Yang, A.; Creancier, L.; Biscan, J.C.; Valent, A.; Minty, A.; Chalou, P.; Lelias, J.M.; Dumont, X.; et al. Monoallelically expressed gene related to p53 at 1p36, a region frequently deleted in neuroblastoma and other human cancers. *Cell* **1997**, *90*, 809–819. [CrossRef]
23. Jost, C.A.; Marin, M.C.; Kaelin, W.G., Jr. P73 is a human p53-related protein that can induce apoptosis. *Nature* **1997**, *389*, 191–194. [CrossRef] [PubMed]
24. Arrowsmith, C.H. Structure and function in the p53 family. *Cell Death Differ.* **1999**, *6*, 1169–1173. [CrossRef]
25. Tomasini, R.; Tsuchihara, K.; Wilhelm, M.; Fujitani, M.; Rufini, A.; Cheung, C.C.; Khan, F.; Itie-Youten, A.; Wakeham, A.; Tsao, M.S.; et al. TAp73 knockout shows genomic instability with infertility and tumor suppressor functions. *Genes Dev.* **2008**, *22*, 2677–2691. [CrossRef] [PubMed]
26. Zhu, J.; Jiang, J.; Zhou, W.; Chen, X. The Potential Tumor Suppressor p73 Differentially Regulates Cellular p53 Target Genes. *Cancer Res.* **1998**, *58*, 5061–5065.
27. Melino, G.; Bernassola, F.; Ranalli, M.; Yee, K.; Zong, W.X.; Corazzari, M.; Knight, R.A.; Green, D.R.; Thompson, C.; Vousden, K.H. P73 Induces Apoptosis via PUMA Transactivation and Bax Mitochondrial Translocation. *J. Biol. Chem.* **2004**, *279*, 8076–8083. [CrossRef]
28. Vernole, P.; Neale, M.H.; Barcaroli, D.; Munarriz, E.; Knight, R.A.; Tomasini, R.; Mak, T.W.; Melino, G.; de Laurenzi, V. TAp73 α binds the kinetochore proteins Bub1 and Bub3 resulting in polyploidy. *Cell Cycle* **2009**, *8*, 421–429. [CrossRef]

29. Yang, A.; Walker, N.; Bronson, R.; Kaghad, M.; Oosterwegel, M.; Bonnin, J.; Vagner, C.; Bonnet, H.; Dikkes, P.; Sharpe, A.; et al. P73-deficient mice have neurological, pheromonal and inflammatory defects but lack spontaneous tumours. *Nature* **2000**, *404*, 99–103. [[CrossRef](#)]
30. Wilhelm, M.T.; Rufini, A.; Wetzel, M.K.; Tsuchihara, K.; Inoue, S.; Tomasini, R.; Itie-Youten, A.; Wakeham, A.; Arsenian-Henriksson, M.; Melino, G.; et al. Isoform-specific p73 knockout mice reveal a novel role for Δ Np73 in the DNA damage response pathway. *Genes Dev.* **2010**, *24*, 549–560. [[CrossRef](#)]
31. Zaika, A.I.; Slade, N.; Erster, S.H.; Sansome, C.; Joseph, T.W.; Pearl, M.; Chalas, E.; Moll, U.M. δ Np73, a dominant-negative inhibitor of wild-type p53 and Tap73, is up-regulated in human tumors. *J. Exp. Med.* **2002**, *196*, 765–780. [[CrossRef](#)]
32. Steder, M.; Alla, V.; Meier, C.; Spitschak, A.; Pahnke, J.; Fürst, K.; Kowtharapu, B.S.; Engelmann, D.; Petigk, J.; Egberts, F.; et al. DNp73 Exerts Function in Metastasis Initiation by Disconnecting the Inhibitory Role of EPLIN on IGF1R-AKT/STAT3 Signaling. *Cancer Cell* **2013**, *24*, 512–527. [[CrossRef](#)] [[PubMed](#)]
33. De Laurenzi, V.; Costanzo, A.; Barcaroli, D.; Terrinoni, A.; Falco, M.; Annicchiarico-petruzzelli, M.; Levrero, M.; Melino, G. Two New p73 Splice Variants with Different Transcriptional Activity. *J. Exp. Med.* **1998**, *188*, 1763–1768. [[CrossRef](#)] [[PubMed](#)]
34. de Laurenzi, V.; Catani, M.V.; Terrinoni, A.; Corazzari, M.; Melino, G.; Constanzo, A.; Levrero, M.; Knight, R.A. Additional complexity in p73: Induction by mitogens in lymphoid cells and identification of two new splicing variants ϵ and ζ . *Cell Death Differ.* **1999**, *6*, 389–390. [[CrossRef](#)] [[PubMed](#)]
35. Rufini, A.; Agostini, M.; Grespi, F.; Tomasini, R.; Sayan, B.S.; Niklison-Chirou, M.V.; Conforti, F.; Velletri, T.; Mastino, A.; Mak, T.W.; et al. P73 in cancer. *Genes Cancer* **2011**, *2*, 491–502. [[CrossRef](#)] [[PubMed](#)]
36. Grespi, F.; Amelio, I.; Tucci, P.; Annicchiarico-Petruzzelli, M.; Melino, G. Tissue-specific expression of p73 C-terminal isoforms in mice. *Cell Cycle* **2012**, *11*, 4474–4483. [[CrossRef](#)]
37. Laubach, K.N.; Yan, W.; Kong, X.; Sun, W.; Chen, M.; Zhang, J.; Chen, X. p73 α 1, a p73 C-terminal isoform, regulates tumor suppression and the inflammatory response via Notch1. *Proc. Natl. Acad. Sci. USA* **2022**, *119*, e2123202119. [[CrossRef](#)]
38. Ran, F.A.; Hsu, P.D.; Wright, J.; Agarwala, V.; Scott, D.A.; Zhang, F. Genome engineering using the CRISPR-Cas9 system. *Nat. Protoc.* **2013**, *8*, 2281–2308. [[CrossRef](#)]
39. Chen, X.; Bargonetti, J.; Prives, C. p53, through p21 (WAF1/CIP1), Induces Cyclin D1 Synthesis. *Cancer Res.* **1995**, *55*, 4257–4263.
40. Liu, G.; Xia, T.; Chen, X. The Activation Domains, the Proline-rich Domain, and the C-terminal Basic Domain in p53 Are Necessary for Acetylation of Histones on the Proximal p21 Promoter and Interaction with p300/CREB-binding Protein. *J. Biol. Chem.* **2003**, *278*, 17557–17565. [[CrossRef](#)]
41. Matyash, V.; Liebisch, G.; Kurzchalia, T.V.; Shevchenko, A.; Schwudke, D. Lipid extraction by methyl-tert-butyl ether for high-throughput lipidomics. *J. Lipid Res.* **2008**, *49*, 1137–1146. [[CrossRef](#)]
42. Folz, J.; Oh, Y.T.; Blaženović, I.; Richey, J.; Fiehn, O.; Youn, J.H. Interaction of Gut Microbiota and High-Sodium, Low-Potassium Diet in Altering Plasma Triglyceride Profiles Revealed by Lipidomics Analysis. *Mol. Nutr. Food Res.* **2019**, *63*, 1900752. [[CrossRef](#)] [[PubMed](#)]
43. Showalter, M.R.; Nonnecke, E.B.; Linderholm, A.L.; Cajka, T.; Sa, M.R.; Lönnerdal, B.; Kenyon, N.J.; Fiehn, O. Obesogenic diets alter metabolism in mice. *PLoS ONE* **2018**, *13*, e0190632. [[CrossRef](#)] [[PubMed](#)]
44. Rabow, Z.; Morningstar, T.; Showalter, M.; Heil, H.; Thongphanh, K.; Fan, S.; Chan, J.; Martínez-Cerdeño, V.; Berman, R.; Zagzag, D.; et al. Exposure to DMSO during infancy alters neurochemistry, social interactions, and brain morphology in long-evans rats. *Brain Behav.* **2021**, *11*, e02146. [[CrossRef](#)] [[PubMed](#)]
45. Barupal, D.K.; Fiehn, O. Chemical Similarity Enrichment Analysis (ChemRICH) as alternative to biochemical pathway mapping for metabolomic datasets. *Sci. Rep.* **2017**, *7*, 14567. [[CrossRef](#)] [[PubMed](#)]
46. Eichmann, T.O.; Lass, A. DAG tales: The multiple faces of diacylglycerol—Stereochemistry, metabolism, and signaling. *Cell Mol. Life Sci.* **2015**, *72*, 3931–3952. [[CrossRef](#)]
47. Koundouros, N.; Poulogiannis, G. Reprogramming of fatty acid metabolism in cancer. *Br. J. Cancer* **2019**, *122*, 4–22. [[CrossRef](#)]
48. Chen, M.; Huang, J. The expanded role of fatty acid metabolism in cancer: New aspects and targets. *Precis. Clin. Med.* **2019**, *2*, 183–191. [[CrossRef](#)]
49. Nagarajan, S.R.; Butler, L.M.; Hoy, A.J. The diversity and breadth of cancer cell fatty acid metabolism. *Cancer Metab.* **2021**, *9*, 2. [[CrossRef](#)]
50. Paton, C.M.; Ntambi, J.M. Biochemical and physiological function of stearoyl-CoA desaturase. *Am. J. Physiol.-Endocrinol. Metab.* **2009**, *297*, 28–37. [[CrossRef](#)]
51. Nakamura, M.T.; Nara, T.Y. Structure, Function, and Dietary Regulation of Δ 6, Δ 5, and Δ 9 Desaturases. *Annu. Rev. Nutr.* **2004**, *24*, 345–376. [[CrossRef](#)]
52. Ntambi, J.M. The regulation of stearoyl-CoA desaturase (SCD). *Prog. Lipid Res.* **1995**, *34*, 139–150. [[CrossRef](#)]
53. Enoch, H.G.; Catala, A.; Strittmatter, P. Mechanism of rat liver microsomal stearyl-CoA desaturase. Studies of the substrate specificity, enzyme-substrate interactions, and the function of lipid. *J. Biol. Chem.* **1976**, *251*, 5095–5103. [[CrossRef](#)]
54. Burlingame, B.; Nishida, C.; Uauy, R.; Weisell, R. Fats and Fatty Acids in Human Nutrition: Introduction. *Ann. Nutr. Metab.* **2009**, *55*, 5–7. [[CrossRef](#)] [[PubMed](#)]
55. Roongta, U.V.; Pabalan, J.G.; Wang, X.; Ryseck, R.P.; Fargnoli, J.; Henley, B.J.; Yang, W.P.; Zhu, J.; Madireddi, M.T.; Lawrence, R.M.; et al. Cancer cell dependence on unsaturated fatty acids implicates stearoyl-CoA desaturase as a target for cancer therapy. *Mol. Cancer Res.* **2011**, *9*, 1551–1561. [[CrossRef](#)]
56. Igal, R.A. Stearoyl-coa desaturase-1: A novel key player in the mechanisms of cell proliferation, programmed cell death and transformation to cancer. *Carcinogenesis* **2010**, *31*, 1509–1515. [[CrossRef](#)] [[PubMed](#)]

57. von Roemeling, C.A.; Marlow, L.A.; Radisky, D.C.; Rohl, A.; Larsen, H.E.; Wei, J.; Sasinowska, H.; Zhu, H.; Drake, R.; Sasinowski, M.; et al. Functional genomics identifies novel genes essential for clear cell renal cell carcinoma tumor cell proliferation and migration. *Oncotarget* **2014**, *5*, 5320–5334. [[CrossRef](#)]
58. Kirschner, K.; Samarajiva, S.A.; Cairns, J.M.; Menon, S.; Pérez-Mancera, P.A.; Tomimatsu, K.; Bermejo-Rodriguez, C.; Ito, Y.; Chandra, T.; Narita, M.; et al. Phenotype Specific Analyses Reveal Distinct Regulatory Mechanism for Chronically Activated p53. *PLoS Genet.* **2015**, *11*, e1005053. [[CrossRef](#)]
59. Harms, K.; Nozell, S.; Chen, X. The common and distinct target genes of the p53 family transcription factors. *C. Cell. Mol. Life Sci.* **2004**, *61*, 822–842. [[CrossRef](#)]
60. Luis, G.; Godfroid, A.; Nishiumi, S.; Cimino, J.; Blacher, S.; Maquoi, E.; Wery, C.; Collignon, A.; Longuespée, R.; Montero-Ruiz, L.; et al. Tumor resistance to ferroptosis driven by Stearoyl-CoA Desaturase-1 (SCD1) in cancer cells and Fatty Acid Binding Protein-4 (FABP4) in tumor microenvironment promote tumor recurrence. *Redox Biol.* **2021**, *43*, 102006. [[CrossRef](#)]
61. Scott, J.S.; Nassar, Z.D.; Swinnen, J.V.; Butler, L.M. Monounsaturated Fatty Acids: Key Regulators of Cell Viability and Intracellular Signaling in Cancer. *Mol. Cancer Res.* **2022**, 1–11. [[CrossRef](#)]
62. Guo, S.; Wang, Y.; Zhou, D.; Li, Z. Significantly increased monounsaturated lipids relative to polyunsaturated lipids in six types of cancer microenvironment are observed by mass spectrometry imaging. *Sci. Rep.* **2014**, *4*, 5959. [[CrossRef](#)] [[PubMed](#)]
63. Ackerman, D.; Simon, M.C. Hypoxia, lipids, and cancer: Surviving the harsh tumor microenvironment. *Trends Cell Biol.* **2014**, *24*, 472–478. [[CrossRef](#)] [[PubMed](#)]
64. Vriens, K.; Christen, S.; Parik, S.; Broekaert, D.; Yoshinaga, K.; Talebi, A.; Dehairs, J.; Escalona-Noguero, C.; Schmieder, R.; Cornfield, T.; et al. Evidence for an alternative fatty acid desaturation pathway increasing cancer plasticity. *Nature* **2019**, *566*, 403–406. [[CrossRef](#)] [[PubMed](#)]
65. Williams, P.E.; Klein, D.R.; Greer, S.M.; Brodbelt, J.S. Pinpointing Double Bond and sn-Positions in Glycerophospholipids via Hybrid 193 nm Ultraviolet Photodissociation (UVPD) Mass Spectrometry. *J. Am. Chem. Soc.* **2017**, *139*, 15681–15690. [[CrossRef](#)]
66. Harris, R.A.; May, J.C.; Stinson, C.A.; Xia, Y.; McLean, J.A. Determining Double Bond Position in Lipids Using Online Ozonolysis Coupled to Liquid Chromatography and Ion Mobility-Mass Spectrometry. *Anal. Chem.* **2018**, *90*, 1915–1924. [[CrossRef](#)]
67. Baba, T.; Ryumin, P.; Duchoslav, E.; Chen, K.; Chelur, A.; Loyd, B.; Chernushevich, I. Dissociation of Biomolecules by an Intense Low-Energy Electron Beam in a High Sensitivity Time-of-Flight Mass Spectrometer. *J. Am. Soc. Mass Spectrom.* **2021**, *32*, 1964–1975. [[CrossRef](#)]
68. Carracedo, A.; Cantley, L.C.; Pandolfi, P.P. Cancer metabolism: Fatty acid oxidation in the limelight. *Nat. Rev. Cancer* **2013**, *13*, 227–232. [[CrossRef](#)]
69. Manzo, T.; Prentice, B.M.; Anderson, K.G.; Raman, A.; Schalck, A.; Codreanu, G.S.; Lauson, C.B.N.; Tiberti, S.; Raimondi, A.; Jones, M.A.; et al. Accumulation of long-chain fatty acids in the tumor microenvironment drives dysfunction in intrapancreatic cd8+ t cells. *J. Exp. Med.* **2020**, *217*, e20191920. [[CrossRef](#)]
70. Kim, J.A. Peroxisome Metabolism in Cancer. *Cells* **2020**, *9*, 1692. [[CrossRef](#)]
71. Smith, R.E.; Lespi, P.; di Luca, M.; Bustos, C.; Marra, F.A.; de Alaniz, M.J.T.; Marra, C.A. A reliable biomarker derived from plasmalogens to evaluate malignancy and metastatic capacity of human cancers. *Lipids* **2008**, *43*, 79–89. [[CrossRef](#)]

Application of MALDI Mass Spectrometry Imaging for Spatially Resolved Metabolomics

Zachary Rabow, Tong Shen, Oliver Fiehn

1. Introduction

Metabolites are the end products of cellular functions and help understand the biochemical changes related to disease processes (1). Traditional approaches for metabolomics involve bulk homogenization of tissue, followed by extraction (and fractionation in the case of dual phase extractions), drying the sample, reconstitution in solvent for liquid chromatography, or possible derivatization to enrich the signal for detection (2). As with any sample preparation process or treatment, these steps introduce a bias in detecting a metabolite. Metabolism occurs in specific cells, at specific times. This spatiotemporal resolution gets lost during bulk homogenization. Tissue homogenization greatly hinders biological interpretation and likely dilutes signal intensities.

Recent advances in technology make it possible to carry out spatial metabolomics, known as mass spectrometry imaging (MSI) (3). MSI avoids the need for bulk homogenization and keeps the tissue intact to preserve the localization of metabolites to specific anatomic regions or lesions (in the case of disease). Matrix-assisted laser desorption/ionization (MALDI) mass spectrometry has been used for the past 20+ years for peptide analysis for proteomics, but is often done in formalin fixed tissue (4). Advancements in sample preparation and instrumentation now enables spatial metabolomics on unfixed tissue.

In this study, we present the application of MSI for lipid analysis in a mouse brain and then extend this workflow to a case study of litter-matched rats, one with a transgene that induces Alzheimer's disease pathology and its wild-type littermate without the disease.

2. Materials and methods

2.1 Murine Samples

24-week-old C57BL/J6 wild-type mice were humanly euthanized, and the tissue was collected quickly. All procedures were done under IACUC protocol.

2.2 Rat model

The TgF344-AD rat model (AD) and wild-type (WT) Fischer 344 littermate were used for molecular pathophysiology investigation. This model has been extensively used and previously described (5). Animals were humanly euthanized at 9 months of age, the time point when AD-like pathology is first seen. All procedures were approved by the IACUC of the University of California, Davis.

2.3 Tissue Collection and Processing

Animals were euthanized using CO₂. The brain was removed, and the right and left lobes were separated by cutting through the midsagittal plane. The tissue was prepared as previously described (7). Briefly, a layer of dry ice was mixed with isopentane, and the left and right hemispheres were placed onto a metal weigh boat on top of the slurry to allow the tissue to freeze completely. Embedding molds were filled partway with 2.6% carboxymethylcellulose (CMC). Once the CMC molds were frozen, brain sections were added to the molds, and more CMC was added on top of the tissue to fully cover the tissue. Once completely frozen, samples were wrapped in foil and stored in -80°C until sectioning. CMC-embedded tissue blocks were placed in Leica Cryostat maintained at -

28°C. The blocks were attached to the chuck using OCT, with care to ensure OCT did not make contact with the cryostat blade. The tissue was sectioned at 10 µm thickness and thaw mounted on indium tin oxide glass slides. Slides were dried in a desiccator for approximately 30 minutes and stored at -80°C until use.

2.4 MSI analysis

Matrix was applied using an HTX Sprayer. Nitrogen was set at 8 psi, and the nozzle temperature was 40°C. Five mL of the matrix (1,5-diaminonaphthalene (DAN), 20 mg/mL in tetrahydrofuran) was loaded onto the sprayer, the valve was then switched to “inject,” and the matrix was sprayed for one minute to ensure the matrix was flowing. Four slides were placed on the slide deck and taped down, and the matrix was applied with the following parameters: 1350 mm/min nozzle velocity, 0.05 mL/min flow rate, 1.5 mm track spacing, crisscross pattern (CC), 5 passes, 40 mm nozzle height, no drying time. After the matrix application was finished, slides were placed in a slide box and stored at -80°C until analysis. MSI analysis was performed using Bruker timsTOF fleX. Mass calibration was performed using an external calibration solution before data collection and achieved 2ppm mass accuracy. Data were acquired between 300 and 1200 m/z range in positive ionization mode with 20 µm spatial resolution. Ion transfer time was 65 µs, and prepulse storage was set to 7µs. The laser was set to 20 µm spatial resolution at 30% power and 200 shots per pixel. Data processing was performed using SCiLS Pro.

3. Results

3.1 Data-driven segmentation of the mouse brain clusters to anatomic regions

The brain of a 24-week-old C57BL/J6 mouse was used for spatial lipidomics investigation. Data-driven, spatial segmentation in SCiLS using the top 500 molecular features results in detailed segmentation resembling known anatomic regions. The top 500 most abundant features were used for unsupervised spatial segmentation using hierarchical clustering of similar spectra. The first segmentation resulted in the differentiation of basic cellular groups consisting of fiber tracts (a), the brain stem (b), the cerebrum (c) and the cerebellum (d) (Fig 1A). Further segmentation using the same molecular features differentiated the hippocampal formation (1), the molecular layers of the cerebellum (2), the granular layers of the cerebellum (3), fiber tracts (4), three segmented molecular layers in the cortex (5), brain stem (6), cerebral nuclei (7) and the hindbrain (8) (Fig 1B). Unsupervised segmentation based on lipid features results in clusters that resemble known anatomic brain regions and cell layers described in the Allen Brain Atlas (Fig 1C).

3.2 MALDI MSI shows high spatial resolution of lipids to distinct anatomic regions

While the MALDI MSI acquired data between 300-1200 m/z that would include small metabolites, we found that the top-500 ions that spatially separated brain regions were all between 620-950 Da. This is the mass region of complex lipids, from phosphatidyl-lipids to triacylglycerides, showing that brain lipids are highly spatially organized. Lipids identified with MS/MS analysis in situ are shown in Fig 2 A-E. PS 44:6 (m/z 890.592) shows high expression in the white matter of the cerebellum, the hindbrain, and in the lower molecular layers of the cortex (2A). In contrast, PS 36:2 (18:1/18:1) is nearly exclusively expressed in the granular layers of the cerebellum (2B). Similarly, PE 44:10 is highly expressed in the granular layers of the cerebellum

and the granular layers of the dentate gyrus and hippocampus (2C). Remarkably, we can see high spatial resolution of this lipid in the hippocampal region, starting with low expression in the subiculum (Fig 2C.1) and then high expression in the pyramidal layer of Ammon's horn (CA1sp, CA2sp, CA3) (Fig 2C.2), low expression between CA3 where the pyramidal layer ends (Fig 2C.3), then high expression in the granular cell layer of the dentate gyrus (Fig 2C.4).

Lipid features can be co-visualized using unique m/z molecular channels, demonstrated with m/z 718.5361 and 890.6313, showing distinct localization patterns (2E). m/z 718.5361 (green) that can be annotated as PE 34:1, is seen to be enriched to the molecular layers of the cerebellum, with slightly lower expression in the granular layers. m/z 890.6313 (purple), annotated as PC 44:6, is enriched within the branching fiber tracts of the cerebellum and homogenously in the medulla and pons. These features were annotated through accurate mass search using LIPIDMAPS. While MS2 data is necessary for a more confident identification, these features show similar spatial distribution as seen in The Metabolome Atlas of the Aging Mouse Brain, which provides a degree of confidence in the identification of these two ions.

Figure 1

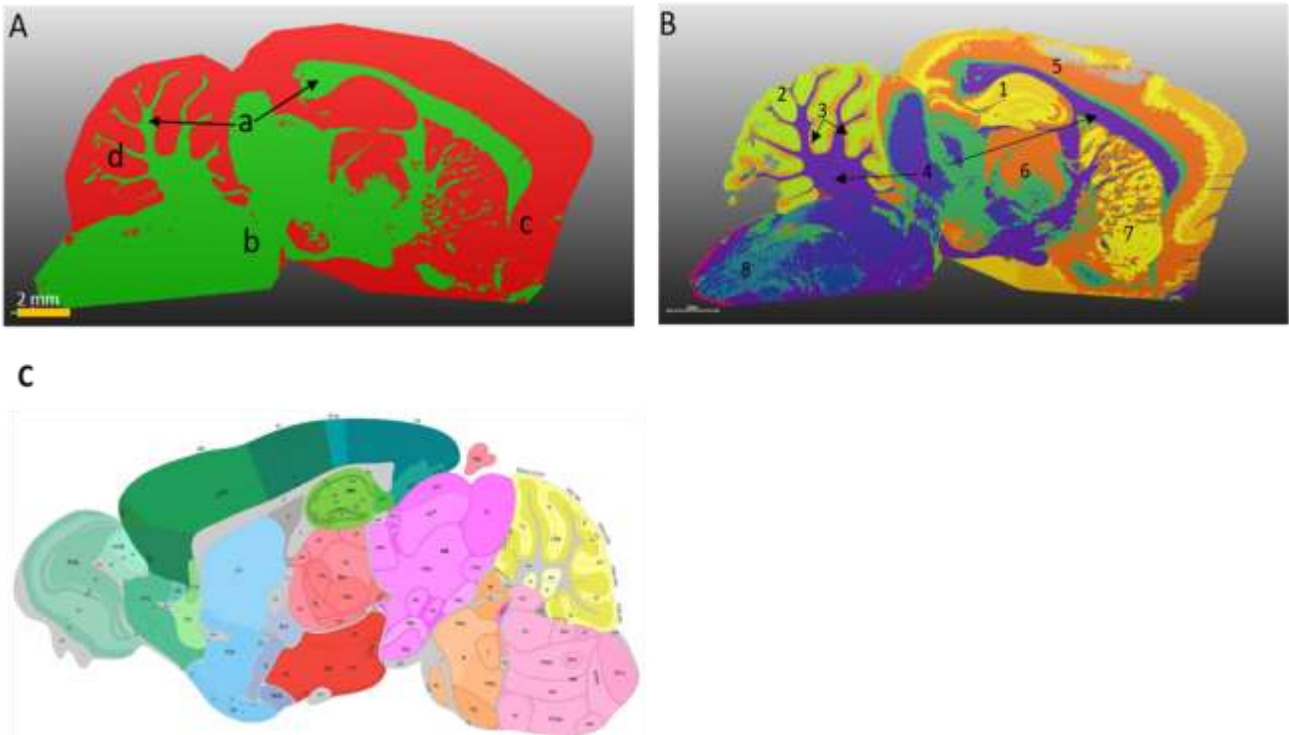


Figure 1. MALDI MSI readily distinguishes anatomically defined regions. Data driven spatial segmentation using the top 500 abundant m/z features enables general brain regions to be seen through hierarchical clustering of similar spectra. (A). Simple, binary segmentation results using the top 500 m/z features. (B). Multiple rounds of segmentation using the same ions as the prior plot show highly specific segmentation patterns that resemble known anatomic brain regions. (C). Map of the Allen Brain Atlas showing anatomically defined regions similar to 1B.

3.3 Statistical analysis and differential expression between regions of interest

Manual segmentation followed by ion peak area extraction allows for analysis of different regions of interest (ROI). Using the optical image of the tissue, the following ROIs were annotated (Fig 3A): (1) cortex, (2) olfactory areas, (3) striatum, (4) fiber tracts, (5) hippocampus (hippocampal formation), (6) thalamus, (7) hypothalamus, (8) midbrain, (9) pons, (10) medulla, (11) cerebellum grey matter, and (12) cerebellum white matter. m/z 789.6195 shows high spatial

differences between brain regions (Fig. 3B). m/z 789.6195 showed significant differences ($p=0.001$) between brain regions (i.e., a three-fold change between the hippocampus and pons; Fig 3C) and within brain regions (differential expression within the layers of the cortex; Fig 3B). A bulk search of LIPIDMAPS for m/z 789.6195 resulted in three possible candidates: FA 44:2; O9 ($\Delta M = 0.0109$), PA 42:0 ($\Delta M = 0.0173$), and PG O-38:2 ($\Delta M = 0.0191$).

The white matter of the cerebellum and the hippocampus were manually annotated, followed by principal component analysis (PCA) to investigate which molecular feature significantly differentiated these two areas. m/z 729.5192 contributed the highest variance to the PCA. The ion map (blue) shows that this feature is highly expressed in white matter in the cerebellum, with low expression in the hippocampal formation (Fig 3D). m/z 729.5192 is significantly different ($p < 0.001$) between these two regions, with a five-fold increase in the white matter compared to the hippocampus (Fig 3E). A bulk search of m/z 729.5192 using LIPIDMAPS resulted in 5 possible candidates: PG-O 34:4 ($\Delta M = 0.0127$ Da), PA 38:2 ($\Delta M = 0.0237$ Da), MGDG 32:1 ($\Delta M = 0.0319$ Da), CerPE 38:3; O3 ($\Delta M = 0.0349$ Da), and PG 33:4 ($\Delta M = 0.0491$ Da). However, all these candidates were outside of the typical 5 mDa mass accuracy window that we found in annotation of other known compounds (see Figure 2). Biologically, m/z 729.5192 might better get annotated as PS 38:2 that fragments into PA-lipids during MALDI ionization, as has been reported before. Correspondingly, m/z 789.6195 could possibly annotate as PS 42:0. It is well documented that collision induced dissociation (CID) of PS's results in an in source fragment, resulting from one of two possible rearrangements, both resulting in a PA artifact. For both features (m/z 789.6195 and 729.5192), in situ MS2 and orthogonal LC-MS/MS are needed to

confidently identify the lipid feature. In addition, LIPIDMAPS only considers $[M+H]^+$ adducts in its online search tool, while $[M+Na]^+$ or $[M+NH_4]^+$ are also typically occurring in lipid ionizations.

Figure 2

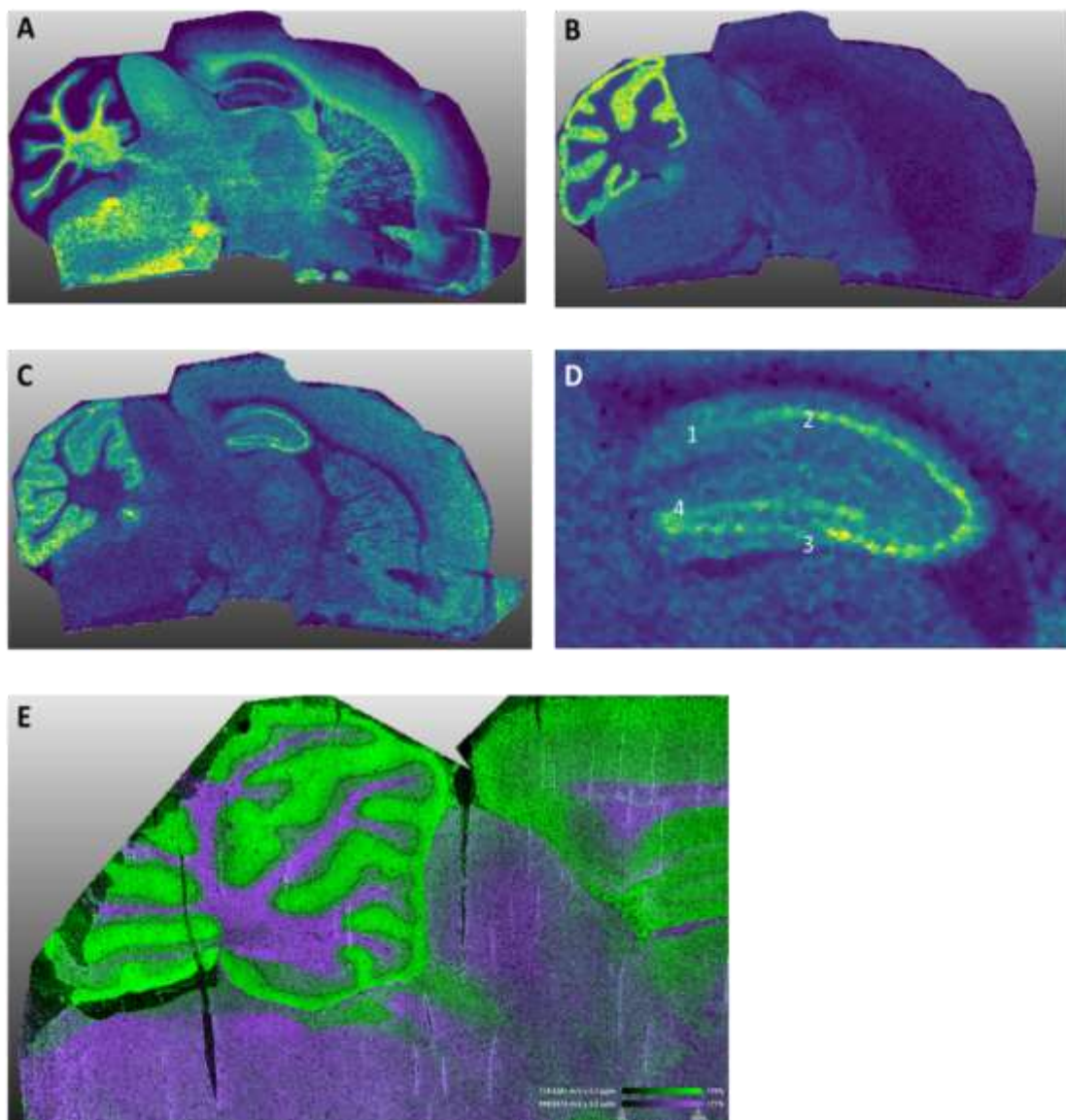


Figure 2. Examples of MALDI MSI Images showing high spatial specificity of lipid ions. (A) PS 44:6 (m/z 890.592) is only found in brainstem and midbrain regions, but not in cerebellum. (B). PS 36:2 is only found in the cerebellum. (C). PE 44:10 is enriched in the cerebellum and hippocampus. (D). 4x magnification of the left image. PE 44:10 is localized to the pyramidal layer of the hippocampus and granular layers of the dentate gyrus. (E). Co-visualization of m/z 718.5361 and 890.6313, showing distinct localization patterns

Figure 3

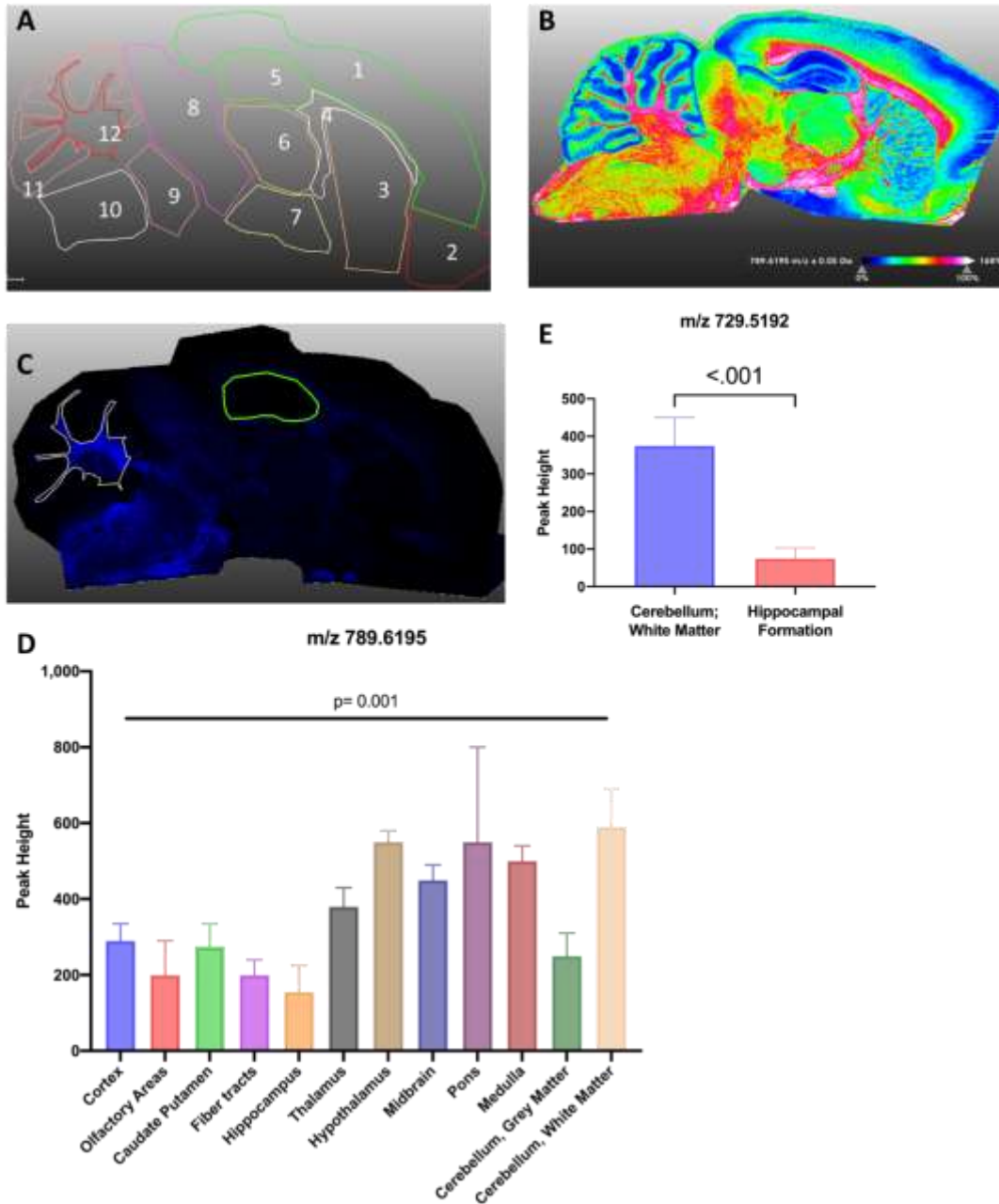


Figure 3. Extraction of Peak area for individual ions enables analysis of different regions of interest (ROI). (A). Schematic diagram for ROI: (1) cortex, (2) olfactory areas, (3) striatum, (4) fiber tracts, (5) hippocampus (hippocampal formation), (6) thalamus, (7) hypothalamus, (8) midbrain, (9) pons, (10) medulla, (11) cerebellum grey matter, and (12) cerebellum white matter. (B) ion image for m/z 789.6195 (C) ion image for m/z 729.5192 (D) Bar plots for selected ROI for m/z 789.6195 (E) bar plot for selected ROI for m/z 729.5192. $n=1$ biological replicate. Data presented as mean \pm SEM. SEM is from the average intensity of the m/z feature in each pixel of the MSI experiment

3.4 MSI shows spatial lipidomic changes in a rat model of AD

MALDI MSI bridges the gap between histopathology and metabolomics, allowing for small molecules and lipids to be visualized in a spatial (or spatiotemporal) fashion. To demonstrate this, a TgF344-AD rat and its wild-type littermate was used to analyze differences in lipids in the brain.

m/z 734.5709, annotated as PC (16:0/16:0), shows significant enrichment in the total brain section ($p < 0.001$) as well as significant differences ($p < 0.001$) in the selected ROI (the hippocampus, or HPF) of the WT brain compared to the AD brain (Fig 4A, D). Conversely, m/z 782.5684, annotated as PC (18:1/18:3) or PC (16:0/20:4), is significantly higher in the HPF in the AD brain compared to HPF of the WT brain (Fig 4B). Interestingly, if the ion intensity for m/z 782.5684 is extracted for the entire brain region, no statistical difference is seen, with a fold change of 0.94 between WT and AD (Fig. 4E); *however*, if the ion intensity for m/z 782.5684 is extracted from just the HPF, we see a significant difference ($p < 0.01$) and a 1.5-fold change difference between WT and AD (Fig. 4E). Similarly, m/z 788.6174, annotated as PC 36:1 (e.g., PC (18:0/18:1), shows no difference in the total brain (Fig 4C, F), but significant differences ($p < 0.001$) within the fiber tracts of the cortex between AD and WT brains (Fig 4C, F).

Figure 4

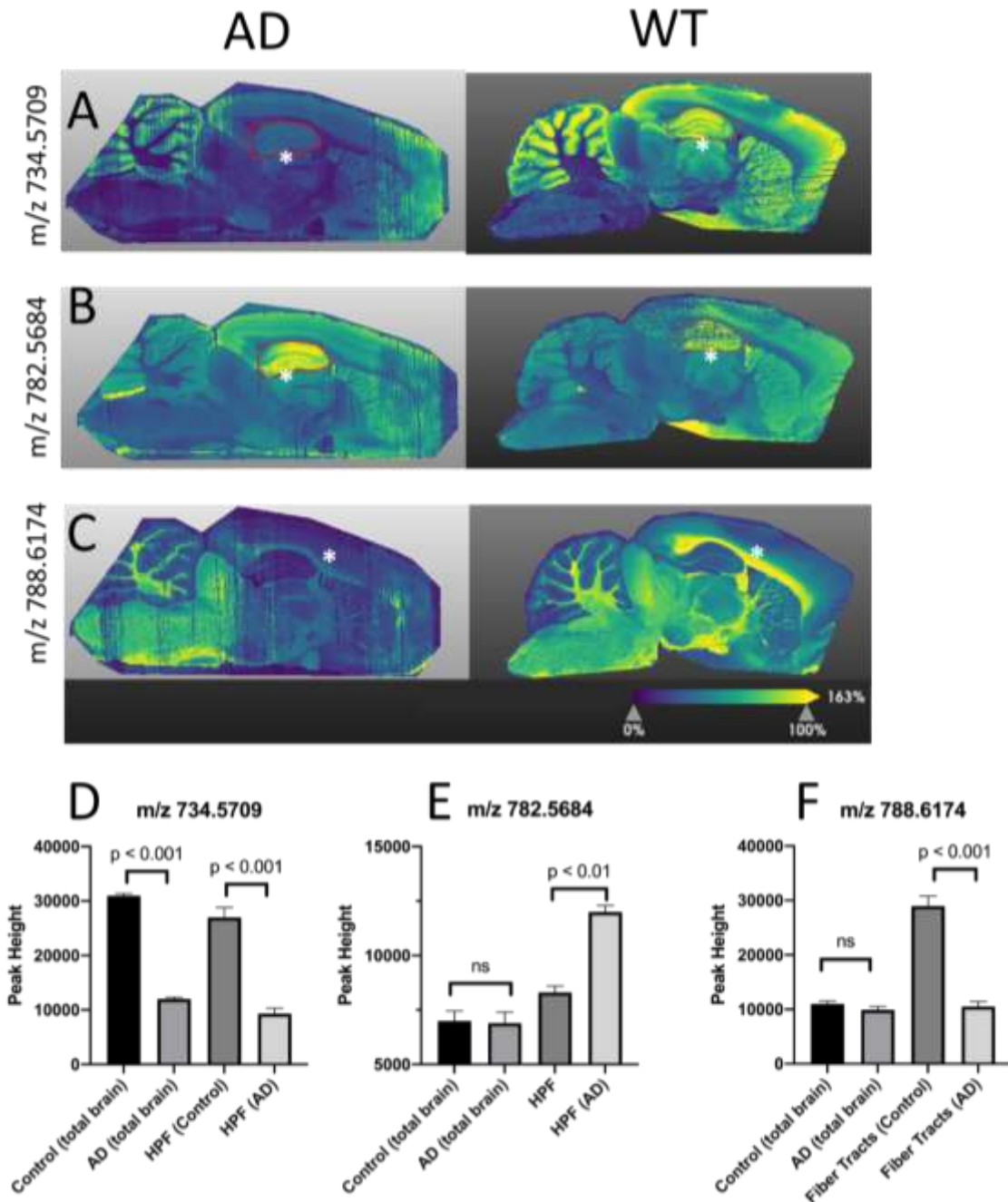


Figure 4. Analysis of a healthy control brain compared to a transgene littermate with AD. Ion images for features of interest are shown for (A) m/z 734.5709, (B) m/z 782.5684, (C) m/z 788.6174. (D-F) Bar graphs for each m/z feature for total brain and extracted ROI. * denotes ROI for selected segmentation and ion intensity extraction. $n=1$ biological replicate/group; data presented as mean \pm SEM. SEM is from the average intensity of the m/z feature in each pixel of the MSI experiment, between 40,000 (smaller ROI) and 2,000,000 pixels for the whole brain section

4. Discussion

The core aspects of pathology are: 1) Etiology/cause, 2) Biochemical and molecular mechanisms (pathogenesis), 3) Associated structural and functional alteration to cells and organs (morphological changes), 4) Clinical consequences of the morphological changes. Here we study the spatial organization of brain lipids, focusing on the core pathology area (3). Lipids are the critical building blocks in the cell and a crucial component of myelin, making lipids a crucial molecule in neurology (7,8). Additionally, lipids make up cell membranes, and are essential for energy storage and cell signaling (9). Lipid composition in the brain plays a pivotal role in maintaining healthy brain physiology. Perturbations to the brain lipidome can lead to neurodegenerative diseases and pathologies- from Alzheimer's (AD), Parkinson's, Huntington's, Schizophrenia, and bipolar (10). Alois Alzheimer and Emil Kraepelin first described AD over a century ago (11). The progressive neurodegeneration that occurs in AD has been researched for over a century, yet the disease is still not well understood, and no treatments exist. However, most research has focused on genetics, diet, exposures, and activation of inflammatory cells (like microglia) in the brain, and lipids have largely been overlooked. Alois Alzheimer's initial description of the disease was around the findings of extensive lipid droplet (LD) formation (12). These LDs are now associated with microglia, and growing evidence shows that defective phagocytosis is responsible for LD formation, microglia activation, and the inflammatory cascade that ensues. LDs are made of complex lipids with varying Fatty acyl (FA) chain lengths and of saturation status. The FA chain length and number of double bonds can greatly affect cellular homeostasis and pathology. For this reason, mass spectrometry is essential to describe and characterize lipids. However, there are different levels of confidence in the identification of lipids

(13). The most basic classification would be discerning the class of lipid detected (phosphatidylcholine or PC, phosphatidylethanolamine or PE, etc.). The next level of identification would be describing the number of carbons and double bonds- if any- (i.e., PC: 36:2). The next level would be detailed fatty acyl identification (i.e., PC (18:0_18:2). The next level would be providing positional information (i.e., PC (18:2/18:0)). There are additional levels of identification that provide information on the modifications (oxidation, hydroxylation, etc.) as well as the stereochemistry and double bond geometry, but these require highly specialized experiments to capture that level of information and are not routinely performed in nontargeted metabolomics.

Traditional metabolomic workflows must catch up in the third core area discussed at the being of this section, linking biochemical changes (function) to spatial and structural regions (morphology). There are numerous reports in the literature of bulk homogenization-based approaches for investigating the chemical biology of diseases or disorders, including the Metabolome Atlas of the Aging Mouse Brain (14). Still, such reports often fail to provide translational power due to overlooking spatial aspects of diseases. Additionally, there is plenty of literature discussing MSI methodologies and approaches for increasing the analytical chemistry aspect of this technology, but very few reports use this workflow and technology for histopathological analysis. While MALDI MSI has seen a tremendous improvement in technological advancements, there are a few critical limitations to the current state of the field that limit research. The first is the limitation of MS¹ only in an imaging experiment. This means we can only get to the first level of lipid identification discussed above and are left to speculate on the second level of information. To determine higher orders of identification, in situ MS² (as

performed in Fig. 2) is needed, perhaps as follow up of automatic regional differentiation as shown in Figure 1A, B. Additional LC-MS/MS of a bulk homogenized brain sections would be needed to distinguish isomers. The experiments discussed in this chapter had a mass accuracy of +/- 5 mDa, as shown for the lipids in Figure 2. . This mass accuracy, combined with being limited to MS¹, limited our ability to provide higher-order information about the lipids presented. Consequently, the lipid annotations using LIPIDMAPS lookups were necessarily preliminary. In addition to these technological limitations, we suffered from instrument issues that could not be fixed to run more biological replicates for the AD/WT case study and perform LC-MS/MS for increased lipid identification.

The data presented here show that ion features provide unique biochemical signatures that segment the brain into clusters representing known anatomic structures. We provide examples of lipids that have a high degree of spatial organization within anatomic regions. We then show that manual spatial segmentation for ROIs enables us to extract ion intensities for different brain regions and analyze the abundance of lipid features in the brain. Finally, we applied this workflow to a case study of litter-matched rats, one healthy control, and one AD animal for spatial metabolomic analysis. The data presented here provide a framework for how MSI can be leveraged to investigate the chemical biology aspect of disease better.

References:

1. Fiehn, Oliver. "Metabolomics—the link between genotypes and phenotypes." *Functional genomics* (2002): 155-171.
2. Vuckovic, Dajana. "Current trends and challenges in sample preparation for global metabolomics using liquid chromatography–mass spectrometry." *Analytical and bioanalytical chemistry* 403.6 (2012): 1523-1548.
3. Murphy, Robert C., Joseph A. Hankin, and Robert M. Barkley. "Imaging of lipid species by MALDI mass spectrometry." *Journal of lipid research* 50 (2009): S317-S322.
4. Bonk, Thomas, and Andreas Humeny. "MALDI-TOF-MS analysis of protein and DNA." *The Neuroscientist* 7.1 (2001): 6-12.
5. Pentkowski, Nathan S., et al. "Anxiety-like behavior as an early endophenotype in the TgF344-AD rat model of Alzheimer's disease." *Neurobiology of aging* 61 (2018): 169-176.
6. Neumann, Elizabeth K., et al. "Protocol for multimodal analysis of human kidney tissue by imaging mass spectrometry and CODEX multiplexed immunofluorescence." *STAR protocols* 2.3 (2021): 100747.
7. Schmitt, Sebastian, Ludovici Cantuti Castelvetti, and Mikael Simons. "Metabolism and functions of lipids in myelin." *Biochimica et Biophysica Acta (BBA)-Molecular and Cell Biology of Lipids* 1851.8 (2015): 999-1005.
8. Storck, Elisabeth M., Cagakan Özbalci, and Ulrike S. Eggert. "Lipid cell biology: a focus on lipids in cell division." *Annual review of biochemistry* 87 (2018): 839-869.

9. Welte, Michael A., and Alex P. Gould. "Lipid droplet functions beyond energy storage." *Biochimica et Biophysica Acta (BBA)-Molecular and Cell Biology of Lipids* 1862.10 (2017): 1260-1272.
10. Shichiri, Mototada. "The role of lipid peroxidation in neurological disorders." *Journal of clinical biochemistry and nutrition* (2014): 14-10.
11. Möller, H-J., and Manuel B. Graeber. "The case described by Alois Alzheimer in 1911." *European archives of psychiatry and clinical neuroscience* 248.3 (1998): 111-122.
12. Foley, Paul. "Lipids in Alzheimer's disease: A century-old story." *Biochimica et Biophysica Acta (BBA)-Molecular and Cell Biology of Lipids* 1801.8 (2010): 750-753.
13. Liebisch, Gerhard, et al. "Update on LIPID MAPS classification, nomenclature, and shorthand notation for MS-derived lipid structures." *Journal of lipid research* 61.12 (2020): 1539-1555.
14. Ding, Jun, et al. "A metabolome atlas of the aging mouse brain." *Nature communications* 12.1 (2021): 1-12.

Appendix: Other Projects

In addition to the projects and work presented in this text, I undertook numerous other research projects that are not presented here. First, I developed a novel high-throughput method for comprehensive metabolomics and lipidomics analysis of blood plasma and serum. I increased the throughput by 10-fold, allowing a 96-well plate of samples to be extracted and prepared for analysis in under an hour. The performance of this new method was validated by absolute quantification of NIST SRM 1950 Plasma for endogenous metabolites, as well as intra- and interday precision. Next, I applied this method to a nested case-cohort study of four longitudinal cohorts (MrOS, SOF, HealthABC, and CHS) for over 24,000 samples for the Longevity Consortium (LC). Secondly, I carried out the sample preparation, data acquisition of over 2,000 murine (brain, heart, liver, kidney and blood plasma) samples investigating the biochemical signatures associated with longevity and aging. I interfaced with statisticians, epidemiologists, chemists, and biologists through both projects. I learned the importance of collaboration and communication through this consortium and am grateful for the support of the LC during my Ph.D. training.

I was a co-author on two other publications. The first was in collaboration with Dr. Lindsay Cameron and Prof. David Olson on the function-oriented synthesis to identify the critical structural components and therapeutic pharmacophore of ibogaine, which enabled the synthesis of a novel compound named tabernanthalog (TBG). In this collaboration, I characterized TBG by mass spectrometry. I developed a targeted LC-MS/MS method using multiple reaction monitoring for pharmacokinetic and pharmacodynamic (PK/PD) assessments of TBG in the brain and liver. The second publication was work I did with Dr. Jun Ding, a postdoctoral scientist in the Fiehn Lab. This project characterized the aging mouse brain in ten anatomic regions. I assisted Dr. Ding in sample preparation, data acquisition, and data interpretation for this project (2). The last significant project I worked on, but not presented in this dissertation, was the investigation of

endogenous psychedelics produced by the gut microbiome. In this project, I developed a highly sensitive targeted LC-MS/MS method to investigate bufotenine, a metabolite that we initially hypothesized was made by the host through the known biosynthetic pathway of the INMT enzyme. An INMT KO mouse model was used, and surprisingly bufotenine levels were unchanged by this KO. A two-year investigation led to the finding that by knocking out the gut microbiome with antibiotics, bufotenine levels are depleted beyond the lower limit of detection. Further, we showed that through administration of classic antidepressants, that bufotenine levels are increased in the brain. This research is ongoing and provides an exciting new framework on the mechanism of how classic antidepressants mediate neurochemistry and behavior. Through this project, I learned the importance of collaboration and a dynamic "Team Science" approach. This project could not have happened without the diverse science background and skills that each team member brought to the table. All of these studies, and those presented in the chapters above, describe my graduate work covering metabolomics, lipidomics, oncology, neurology, PK/PD, and analytical chemistry.

Below is a summary of the projects that have been published or are being prepared for publication

Published:

1. Cameron, Lindsay P., et al. "A non-hallucinogenic psychedelic analogue with therapeutic potential." *Nature* 589.7842 (2021): 474-479.
2. Ding, Jun, et al. "A metabolome atlas of the aging mouse brain." *Nature communications* 12.1 (2021): 1-12.
3. Rabow, Zachary, et al. "p73 α 1, an Isoform of the p73 Tumor Suppressor, Modulates Lipid Metabolism and Cancer Cell Growth via Stearoyl-CoA Desaturase-1." *Cells* 11.16 (2022): 2516.

4. Rabow, Zachary, et al. "Exposure to DMSO during infancy alters neurochemistry, social interactions, and brain morphology in long-evans rats." *Brain and behavior* 11.5 (2021): e02146.

In preparation or under review:

1. Burg A, Showalter M, Rabow Z Carraway K, Fiehn O. "Malignant transformation-induced alterations in bis(monoacylglycerol)phosphate (BMP) lipids"
2. Rabow Z, Keshet U, Tong S, Fiehn O. "Comprehensive High-throughput Methods and Cloud Based Computing for Large Scale Metabolomics Studies"
3. Rabow Z, Cameron LP, Patel S, Fiehn O, Olson D. "Endogenous Psychedelics Are Produced by the Gut Microbiome"